



Regulating the surface of nanoceria and its applications in heterogeneous catalysis

Yuanyuan Ma^a, Wei Gao^{a, b, c}, Zhiyun Zhang^a, Sai Zhang^a, Zhimin Tian^a, Yuxuan Liu^a, Johnny C. Ho^{b, c}, Yongquan Qu^{a, *}

^a Center for Applied Chemical Research, Frontier Institute of Science and Technology, Shaanxi Key Laboratory of Energy Chemical Process Intensification, School of Chemical Engineering and Technology, Xi'an Jiaotong University, Xi'an 710049, China

^b Department of Materials Science and Engineering, City University of Hong Kong, 83 Tat Chee Avenue, Kowloon, Hong Kong, PR China

^c Shenzhen Research Institute, City University of Hong Kong, Shenzhen 518057, PR China

ARTICLE INFO

Article history:

Accepted 2 February 2018

Available online 15 February 2018

Keywords:

Heterogeneous catalysis

Metal oxide catalysts

CeO₂

Oxygen vacancy

Surface control

CO oxidation

CO₂ reduction

Hydrogenation

Hydrolysis

Biomimetic catalysis

ABSTRACT

Ceria (CeO₂) as a support, additive, and active component for heterogeneous catalysis has been demonstrated to have great catalytic performance, which includes excellent thermal structural stability, catalytic efficiency, and chemoselectivity. Understanding the surface properties of CeO₂ and the chemical reactions occurred on the corresponding interfaces is of great importance in the rational design of heterogeneous catalysts for various reactions. In general, the reversible Ce³⁺/Ce⁴⁺ redox pair and the surface acid-base properties contribute to the superior intrinsic catalytic capability of CeO₂, and hence yield enhanced catalytic phenomenon in many reactions. Particularly, nanostructured CeO₂ is characterized by a large number of surface-bound defects, which are primarily oxygen vacancies, as the surface active catalytic sites. Many efforts have therefore been made to control the surface defects and properties of CeO₂ by various synthetic strategies and post-treatments. The present review provides a comprehensive overview of recent progress in regulating the surface structure and composition of CeO₂ and its applications in catalysis.

© 2018 Elsevier B.V. All rights reserved.

Contents

1. Introduction	2
2. Crystal structures of CeO ₂	3
3. Synthesis of CeO ₂ catalysts	4
3.1. Hydrothermal synthesis	4
3.2. Solvothermal synthesis in the presence of capping agents	7
3.3. Template-assisted synthesis	7
4. Surface control on CeO ₂ nanomaterials	9
5. Catalytic performance	13
5.1. CO oxidation	13
5.2. CO ₂ conversion	17
5.2.1. Catalytic synthesis of carbonates by CeO ₂ catalysts	17
5.2.2. Reduction of CO ₂	18
5.3. Organic transformation	21
5.3.1. Hydrolysis and dehydration reactions	21
5.3.2. Oxidation reactions	23
5.3.3. Hydromethoxylation of acrylonitrile	26
5.3.4. Catalytic hydrogenation	26

* Corresponding author.

E-mail address: yongquan@xjtu.edu.cn (Y. Qu).

5.3.5.	Other catalytic organic reactions	29
5.4.	Biomimetic catalysis	30
5.4.1.	Peroxidase-like activity of CeO ₂	30
5.4.2.	SOD and catalase activity	31
5.4.3.	Oxidase activity	32
5.4.4.	Phosphatase-mimetic activity	32
6.	Conclusions and perspectives	33
	Acknowledgments	34
	References	34

1. Introduction

In recent years, due to the unique properties, ceria (CeO₂) is finding prolific industrial applications [1–12]. For example, CeO₂-based materials have been widely explored as electrolytes in solid oxide fuel cells since their oxygen ionic conductivity is exceptionally high at the temperature range of 800–1100 K [13,14]. Fine CeO₂ powders are often used as polishing agents in glass and screen manufacturing [15,16] while CeO₂ materials are also served as an ultraviolet absorbent because of its appropriate band gap of 3.2 eV [17]. Among different utilizations, the most successful commercial application of CeO₂ is considered as its use in three-way catalysts (TWCs) for the elimination of toxic auto-exhaust gases, where CeO₂ plays an important role as an oxygen storage material in order to promote the catalytic performance of TWCs [2,18–20]. Regardless, the widespread industrial applicability of CeO₂ is mainly originated from its distinctive surface characteristics, which involves the reversible Ce³⁺/Ce⁴⁺ redox pair as well as their surface acid-base properties [21–23]. Pure stoichiometric CeO₂ typically presents a fluorite structure with atoms arranged in a face-centered cubic unit cell with a *Fm3m* space group. When CeO₂ is shrunk down to the nanoscale, its formation energies of structural defects would be considerably reduced, leading to the production of non-stoichiometric CeO₂ nanomaterials [1]. These structural defects are primarily oxygen vacancies accompanied with the generation of Ce³⁺ species. In this case, such unique surface properties induce the intensive exploration on catalytic performances of CeO₂ as the active component, promoter, and support.

Generally, heterogeneous catalysis involves (1) the adsorption of at least one of the reactants on the less coordinated surface sites of solid catalysts, (2) the activation of the adsorbed reactants, (3) the subsequent formation of the intermediate species and the adsorbed products through surface reactions catalyzed by the active sites, and (4) the final release of the adsorbed products from catalyst surfaces and the recovery of the surface active sites. Therefore, any

change in the surface properties of solid catalysts would substantially affect the entire catalytic process, which dictates the corresponding catalytic efficiency and chemoselectivity. For instance, the structural defects of CeO₂-based catalysts is observed to have a significant effect on their intrinsic catalytic capabilities and activities for many desired reactions [4]. Inspired by the motivation to modulate and optimize the surface properties of CeO₂, the synthesis of CeO₂ nanostructures with controllable chemical compositions, uniform sizes, and well-defined morphologies has become one of the prime topics in the scientific community. It has been found that the synthetic strategies by considering the pressure, temperature, surfactants, and additives, etc. play essential roles in determining the surface properties of as-synthesized CeO₂ nanostructures. Moreover, the technological applications of CeO₂ nanostructures have also been comprehensively discussed [4,24]. However, even though there are extensive efforts, including chemical doping and various post-treatments, have been made to regulate the structural defects of CeO₂, there still remains a lack of an effective approach to realize the controllable modulation of the surface properties of CeO₂.

Until now, the synthesis of CeO₂ nanostructures and their applications in catalysis and biology have been well summarized in the literature [1,3–7,9–11,25–33]; nevertheless, the modulations of surface physicochemical properties of CeO₂ have not been surveyed in details. In this review, we present a comprehensive summary on the approaches to regulate surface properties of nanoscaled CeO₂ and their applications in advanced catalysis. Following an introduction, a brief summary of the synthesis of CeO₂ nanostructures and their effects on the surface properties of as-synthesized CeO₂ are thoroughly discussed. It includes the conventional synthetic methods as well as the recently developed novel synthetic approaches. Regulating the surface properties of CeO₂ by post-treatments and chemical doping is also systematically described. More importantly, the surface chemistry of CeO₂ nanomaterials manipulated by various strategies for advanced catalysis, including

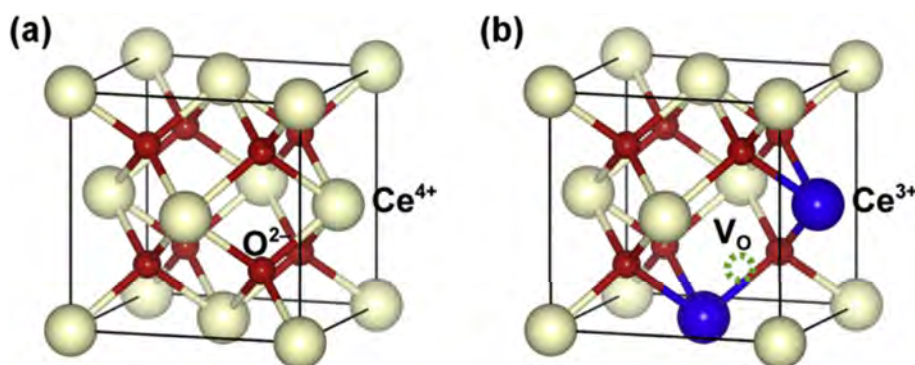
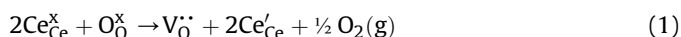


Fig. 1. (a) Ideal crystal structure of CeO₂. (b) Crystal structure of CeO₂ in the presence of one oxygen vacancy accompanied with two generated Ce³⁺ species.

gas-solid, liquid-solid, and biometric reactions are as well carefully reviewed. Based on all these discussion, the insightful summary and perspective outlook are then presented at the end.

2. Crystal structures of CeO₂

Typically, stoichiometric CeO₂ adopts a cubic fluorite structure with a face-centered cubic unit cell ($a = 0.5411$ nm, JCPDS 34–394). In this structure, each Ce⁴⁺ ion has the coordination number of eight and is centered in the cubic cell of eight O^{2−} centers (Fig. 1a). Each O^{2−} ion is coordinated to four Ce⁴⁺ centers. Because of the reversible surface Ce³⁺/Ce⁴⁺ redox pair, the nonstoichiometric CeO₂ is generally formed by the release of oxygen and the subsequent formation of oxygen vacancy within the crystal structure can be understood as shown in Equation (1).



At the same time, Fig. 1b shows an illustration of the structural defects of CeO₂. With the formation of an oxygen vacancy in the lattice, the removal of an oxygen atom would leave two electrons localized in the two cerium cations and alters their oxidation states from Ce⁴⁺ to Ce³⁺, accordingly. However, the precise spatial locations of the missing oxygen atom and the two cerium cations cannot be easily identified [34–36]. The recent scanning tunneling microscopy (STM) experiments and PBE + U theoretical calculations revealed that both Ce³⁺ cations or at least one Ce³⁺ ion is not adjacent to the site of oxygen vacancy [34,35]. Since the size of Ce³⁺ is larger than that of Ce⁴⁺, the formation of oxygen vacancy would also induce certain lattice distortion, affecting the corresponding charge distribution on the surface or in the bulk of CeO₂ [36].

Moreover, the formation of oxygen vacancy would become extremely prominent when the size of CeO₂ crystals is shrunk down to the nanoscale. The presence of surface defects that are primarily oxygen vacancies can enrich the surface chemistry of nanostructured CeO₂. In addition to the reversible Ce³⁺/Ce⁴⁺ redox pair, the surface of CeO₂ is also demonstrated with the multifunctional behavior with the coexistence of surface acidic and basic sites. The terminated OH groups are typically bases on the surface while the Ce⁴⁺ ions have both Brønsted and Lewis acidic characteristics. Therefore, the multifunctionalized surface properties of CeO₂ nanostructures can trigger numerous practical applications in catalysis. Usually, the catalytic performance of CeO₂-based catalysts hinges upon how the CeO₂ surface may be effectively reduced and how the oxygen be efficiently stored; in other words, the performance is highly depended on the effectiveness of the material repeatedly passing through Ce³⁺/Ce⁴⁺ redox cycles [37]. Also, the ability of nanoceria to switch between different oxidation states is largely determined by the ratio of Ce³⁺/Ce⁴⁺ and the concentration of oxygen vacancies. As a result, many efforts have been made for controlling the concentrations of surface Ce³⁺ and oxygen vacancies by various synthetic strategies, chemical doping schemes, and post-treatment methods of CeO₂ [2,4,38].

In this regard, many technologies have been developed and devoted to understand the surface properties of CeO₂ and their corresponding catalytic characteristics considering the single crystal-based material with well-defined crystal structures as model catalysts under ultra-high vacuum (UHV) conditions [27,39–42]. These techniques include STM, X-ray photoelectron spectroscopy (XPS), Fourier transform infrared spectroscopy (FTIR), X-ray absorption spectroscopy (XAS), and calorimetry, etc, which have been already well summarized in previous reviews [30,33,43]. The catalytic interaction between well-defined CeO₂ surfaces and small molecules (e.g., CO, H₂, H₂O, CO₂, NO_x, and CH₄) can also be revealed by these characterization approaches [30,33,43,44]. All

these studies would provide important insights into the catalytic mechanism and pave plausible approaches for the design of efficient and robust catalysts. However, practical catalytic reactions generally occur under high pressure with nanoscaled materials as catalysts. Thus, these investigations often encounter the so-called material gap and pressure gap [44]. The material gap is referred to the size effect encountered when the catalyst is scaled to nano-dimension, as compared with the two-dimensional (2D) planar single crystal surface. For example, the active sites in the corners and edges of the nanoscaled catalysts cannot be simulated precisely along with the single crystal surface. Similarly, the pressure gap is denoted as the surface reconstruction and adsorption configuration of reactants on the catalyst surface under UHV and high pressure conditions. Both gaps might induce very different electronic structures of the catalytic sites, and even different catalytic active sites and various adsorption configurations of reactants under the practical and UHV conditions.

For characterizations of the surface properties of CeO₂ nanostructured catalysts, the surface Ce³⁺ fraction, concentration of oxygen vacancy, and oxygen storage capacity (OSC) are commonly used as important parameters in the field of catalysis. In this case, the XPS technique is widely used to study the chemical states of heterogeneous catalysts, which can provide a quantitative analysis on the surface properties of a solid. For instance, by fitting the XPS peak of Ce 3d core level and integrating all the respective peaks, the surface Ce³⁺ fraction of CeO₂ nanocrystals can be determined [45]. Also, the Raman spectrum of CeO₂ usually shows two characteristic bands of CeO₂ at ~460 and ~600 cm^{−1}. The strong band at ~460 cm^{−1} can be attributed to the Raman-active vibrational mode (F_{2g}) of the fluorite-type structure, while the band at ~600 cm^{−1} is due to the existence of intrinsic oxygen vacancies [37,45]. Thus, the ratios of integral areas of the two peaks can be qualitatively compared with the concentrations of oxygen vacancies among various CeO₂ catalysts. The concentration of surface oxygen vacancy (N in cm^{−3}) can also be semi-quantitatively calculated from the grain size of CeO₂ nanostructures, which can be obtained by Raman spectroscopy, as shown in Equations (2)–(4) [46]:

$$d_g(\text{nm}) = \frac{51.8}{\Gamma(\text{cm}^{-1}) - 5} \quad (2)$$

$$L(\text{nm}) = \sqrt[3]{\left(\frac{\alpha}{2d_g}\right)^2 [(d_g - 2\alpha)^3 + 42d_g^2\alpha]} \quad (3)$$

$$N = 3/4\pi L^3 \quad (4)$$

where Γ (cm^{−1}) is the half-width at half-maximum of the strong Raman peak of CeO₂ at ~460 cm^{−1}, d_g is the calculated grain size of CeO₂ from the Raman spectrum, L is the calculated average distance between two lattice defects, and α is the radius of CeO₂ unit (0.34 nm).

In addition, the reversible Ce³⁺/Ce⁴⁺ redox pair suggests the capability of CeO₂ to switch between releasing and storing of oxygen. This surface property is defined as the OSC, which can be used to quantitatively evaluate the capability of CeO₂ catalysts in releasing and storing oxygen [47,48]. The temperature-programmed reduction by reductants (e.g., CO, H₂, and hydrocarbon) and re-oxidation by oxidants (e.g., O₂, and NO) can give the OSC values of CeO₂ at a specific temperature [49–54]. Notably, the OSC parameter of CeO₂-based materials is critical for TWCs in the automobile converters, where a high value of OSC can promote the oxidation of CO and hydrocarbon and the reduction of NO_x [47,55,56].

Table 1
Summary of synthetic methods for CeO₂ catalysts.

#	Method	Solvent	Reagent	Stabilizer/ template	Conditions	Production description	Ref.
1	Hydrothermal	Water	NaOH, Ce(NO ₃) ₃ ·6H ₂ O	—	100 °C 24 h in a Pyrex bottle	Porous ceria nanorods, 8 × 60 nm	[37]
2	Hydrothermal	Water	Ce(NO ₃) ₃ ·6H ₂ O, ammonia, hydrogen peroxide	—	160 °C 12 h in autoclave 250 °C for different times, followed by heat treatment at different temperatures	Nanoparticles, 10–15 nm	[65]
3	Hydrothermal	Water	NaOH, Ce(NO ₃) ₃ ·6H ₂ O	—	100, 140, 180 °C with different alkali concentrations for 24 h	Polyhedra, 11 ± 1.8 nm Nanorods: (9.6 ± 1.2) × (50–200) nm	[68]
4	Hydrothermal	Water	Ce(NO ₃) ₃ ·6H ₂ O, urea	—	160 °C for different times	Nanooctahedra, 300 nm	[69]
5	Hydrothermal	Water	Ce(NO ₃) ₃ ·6H ₂ O, Na ₃ PO ₄ ·6H ₂ O	—	170 °C for different times	Nanooctahedra, 100–200 nm Nanorods, hundreds of nanometers	[70]
6	Hydrothermal	Water	Ce(NO ₃) ₃ ·6H ₂ O, urea	CTAB	150 °C for 16 h, followed by annealing at 650 °C for 7 h	triangular microplates: edge length of 300 nm–1 μm, thickness of 100–200 nm	[72]
7	Hydrothermal	Water	Ce(NO ₃) ₃ ·6H ₂ O, NaOH, CeCl ₃ ·7H ₂ O, NaNO ₃ , NaBrO ₃ , NaBr, NaI, and Na ₂ SO ₄	—	150 °C for different times	Different morphology when different anions are added during the hydrothermal process, including nanorods and nanocubes	[73]
8	Simultaneous polymerization-precipitate reaction, metamorphic reconstruction, and hydrothermal process	Water	Ce(NO ₃) ₃ ·6H ₂ O, glucose, acrylamide, ammonia	—	180 °C for 72 h, followed by annealing at 600 °C for 6 h and 400 °C for 4 h	Flowerlike microspheres with diameter of several micrometers	[75]
9	Solvothermal	Toluene	Ce(NO ₃) ₃ ·6H ₂ O, tert-butylamine	Oleic acid	180 °C for 24 h	Nanocubes, 15.65 nm	[76]
10	Solvothermal	Ethanol, water	Ce(NO ₃) ₃ ·6H ₂ O, TMAH	PVP	200 °C for 18 h	Nanocubes, 9–17 nm Truncated octahedra, 17 nm	[77]
11	Thermal decomposition	Oleic acid, oleylamine, 1-octadecene	Cerium acetate hydrate, sodium oleate	Oleic acid, oleylamine, 1-octadecene	320–330 °C for 30 min	Nanoplates, length of 151.6 nm and width of 14.3 nm	[78]
12	Template-assisted synthesis	Water	CeCl ₃ ·7H ₂ O, NaOH	SBA-15	Annealing at 700 °C	Mesoporous structure with pore-size centered at 3.5 nm	[79]
13	Template-assisted synthesis	Water	Ce(NO ₃) ₃ ·6H ₂ O, NaOH	CTAB	Annealing at 400 °C for 4 h	Mesoporous structure with pore-size centered at 9.5 nm	[80]
14	Solution-precipitation	Water	Cerium acetate hydrate, ammonia	Sodium bis(2-ethylhexyl) sulfosuccinate	Precipitating at 67 °C for 72 h, followed by annealing at 400 °C for 4 h	Nanowires with diameters of 30–120 nm and lengths of 0.2–5 μm	[81]
15	Potentiostatic electrochemical deposition	Ethyl alcohol	CeCl ₃ ·7H ₂ O	AAO	–10 V vs. SCE for different times	Nanotubes with diameters of 210 nm and lengths of 60 μm	[82]
16	Solution-precipitation	Water	Ce(NO ₃) ₃ ·6H ₂ O, oxalic acid	Anodic alumina membranes	Precipitating for 3 h, followed by annealing at 700 °C for 10 h	Nanowires with diameters of 60 nm and lengths of 50 μm	[83]
17	Solution-precipitation	Water	Ce(NO ₃) ₃ ·6H ₂ O, HMT	PS microspheres	Precipitating at 75 °C for 2 h, followed by annealing at 600 °C for 2 h	Hollow microspheres with various shell thickness	[84]
18	Hydrothermal	Water	CeCl ₃ ·6H ₂ O, ammonia	Sodium oleate	180 °C for 48 h, followed by annealing at 400 °C for 2 min	Ultrathin nanosheets with thickness of about 0.6 nm	[85]

3. Synthesis of CeO₂ catalysts

Nanosize effects on the catalysts' performance are generally observed in heterogeneous catalysis. In particular, when the dimension of catalytic materials decreases down to the range of 1–10 nm or even to subnanometers/single atom, strong size effects are observed to impose on their catalytic activity, selectivity, and stability because of the distinct changes in the surface physico-chemical properties of catalysts as compared with their bulk counterparts [57–63]. Although the origin of these nanosize effects is still not thoroughly understood, many experimental studies have witnessed the importance of size controllability on the catalysts for various reactions. In principle, solid catalysts with the smaller sizes offer the higher catalytic activity and/or the better chemoselectivity. The morphology of catalysts has also been found to have

an equal importance in the modulation of their surface chemistry and the manipulation of electronic structures of their surface active sites. As a result, considerable attentions have been paid on the synthesis of nanocatalysts with tailorable sizes and shapes. In this section, the synthetic strategies of CeO₂ nanocatalysts (Table 1) are given and thoroughly discussed: (1) hydrothermal synthesis, (2) solvothermal synthesis, and (3) template-assisted synthesis.

3.1. Hydrothermal synthesis

Hydrothermal synthesis is a facile and cost-effective method for the preparation of crystalline CeO₂ powders. In the early studies, ultrafine CeO₂ powders were prepared hydrothermally in the presence of an excess amount of ammonia in a stainless steel autoclave at temperatures of 150–200 °C [64]. Nanocrystalline

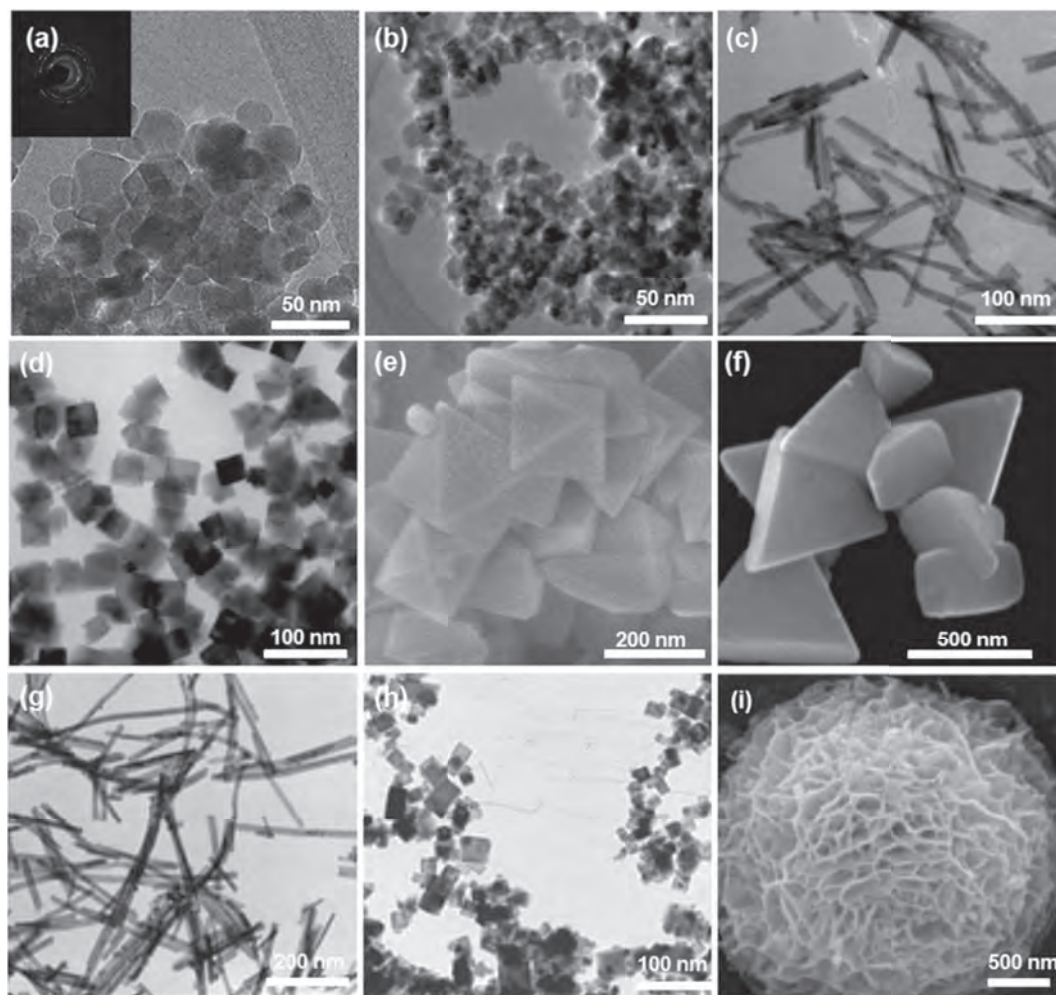


Fig. 2. Representative morphologies of CeO_2 synthesized by hydrothermal methods (a) TEM image of CeO_2 nanocrystalline particles, adapted with permission from Ref. [65]. Copyright © 2007, Elsevier B. V. All rights preserved. (b–d) TEM images of polyhedral CeO_2 nanoparticles, CeO_2 nanorods, and CeO_2 nanocubes, respectively, adapted with permission from Ref. [68]. Copyright © 2005, American Chemical Society. (e) SEM image of CeO_2 octahedra, adapted with permission from Ref. [69]. Copyright © 2011, Elsevier B. V. All rights preserved. (f) SEM image of CeO_2 triangular microplates, adapted with permission from Ref. [72]. Copyright © 2006, American Chemical Society. (g–h) TEM image of CeO_2 nanocubes and CeO_2 truncated octahedra, adapted with permission from Ref. [73]. Copyright © 2008, American Chemical Society. (i) SEM image of monodisperse flowerlike CeO_2 microspheres, adapted with permission from Ref. [74]. Copyright © 2006, American Chemical Society.

particles of CeO_2 (Fig. 2a) could also be obtained by a low-temperature hydrothermal process at 250°C , where cerium hydroxide and ceria acetate were used as precursors [65]. The entire hydrothermal process has been recognized as the well-known dissolution/recrystallization mechanism [66,67]. On the basis of this growth mechanism, Yan et al. reported a template-free hydrothermal method to synthesize CeO_2 nanostructures with well-controlled morphologies as shown in Fig. 2 [68]. Typically, the hydrothermal temperatures and concentrations of bases play important roles in controlling the morphologies of CeO_2 nanostructures. In particular, anisotropic $\text{Ce}(\text{OH})_3$ nuclei would be formed once the Ce^{3+} ion precursors are added into an aqueous NaOH solution. At low concentrations of NaOH (e.g. $< 1.0\text{ M}$) and low hydrothermal temperature (e.g. 100°C), the chemical potential driving force for the anisotropic growth of $\text{Ce}(\text{OH})_3$ nuclei is inadequate, thereby leading to the formation of polyhedral CeO_2 nanoparticles enclosed with (111) and (100) facets (Fig. 2b). When the NaOH concentration is increased, it accelerates the dissolution/recrystallization rates and results in the anisotropic growth of $\text{Ce}(\text{OH})_3$ nuclei. For the further increase in the concentration of NaOH over 6.0 M , pure CeO_2 nanorods can be synthesized (Fig. 2c).

Notably, at a hydrothermal temperature of 180°C , $\text{Ce}(\text{OH})_3$ nuclei would become unstable in which they can be readily oxidized to CeO_2 . In this case, CeO_2 nanocubes can be produced at a high concentration of NaOH (6.0 M , Fig. 2d). On the other hand, CeO_2 octahedra can be made using a similar process, where urea is used during the synthesis (Fig. 2e) [69]. They can also be synthesized using $\text{Ce}(\text{NO}_3)_3$ as the cerium source and Na_3PO_4 as the mineralizer by a hydrothermal process at 170°C [70,71].

Later, CeO_2 nanostructures with controllable sizes and morphologies, and tailorable surface properties can be synthesized by modified hydrothermal methods in the presence of surfactants or with optimized hydrothermal parameters (e.g., temperature, pressure). For example, single-crystal $\text{Ce}(\text{OH})\text{CO}_3$ triangular microplates were successfully made in the presence of the surfactant cetyltrimethyl ammonium bromide (CTAB) during the hydrothermal process [72]. Thermal treatments on the obtained $\text{Ce}(\text{OH})\text{CO}_3$ precursor could further produce CeO_2 triangular microplates with single-crystal structures (Fig. 2f). Small inorganic anions could also be used to control the growth of CeO_2 nanocrystals. In this manner, NO_3^- was observed to be effective in the synthesis of nanocubes, while halides and SO_4^{2-} were found to induce the assembly of CeO_2

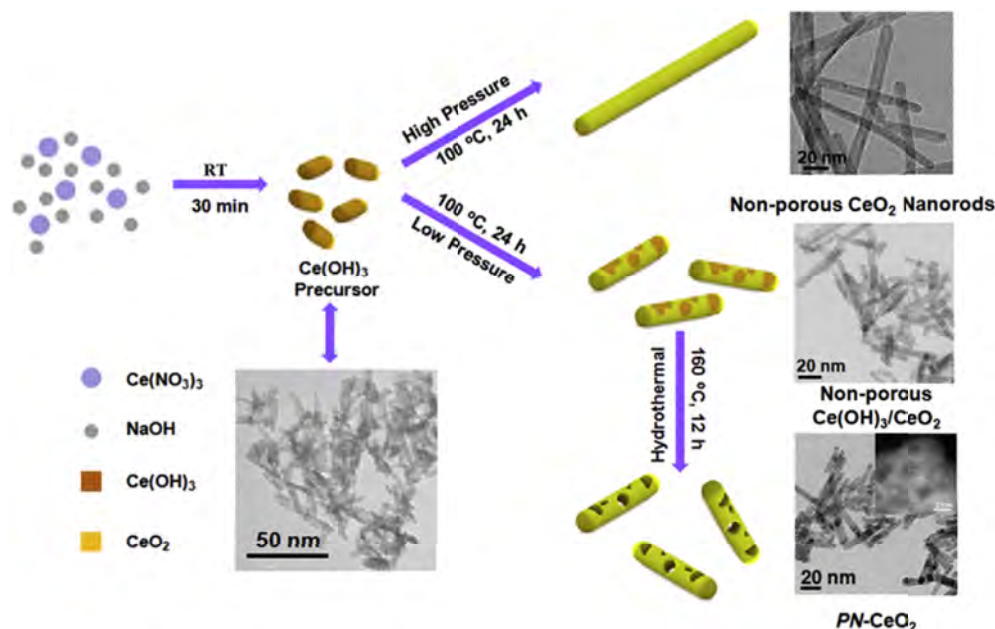


Fig. 3. Schematic illustration of the synthesis of PN-CeO₂ at low pressure. Its morphological evolution was revealed from TEM images. Adapted with permission from Ref. [37]. Copyright © 2014, Royal Society of Chemistry.

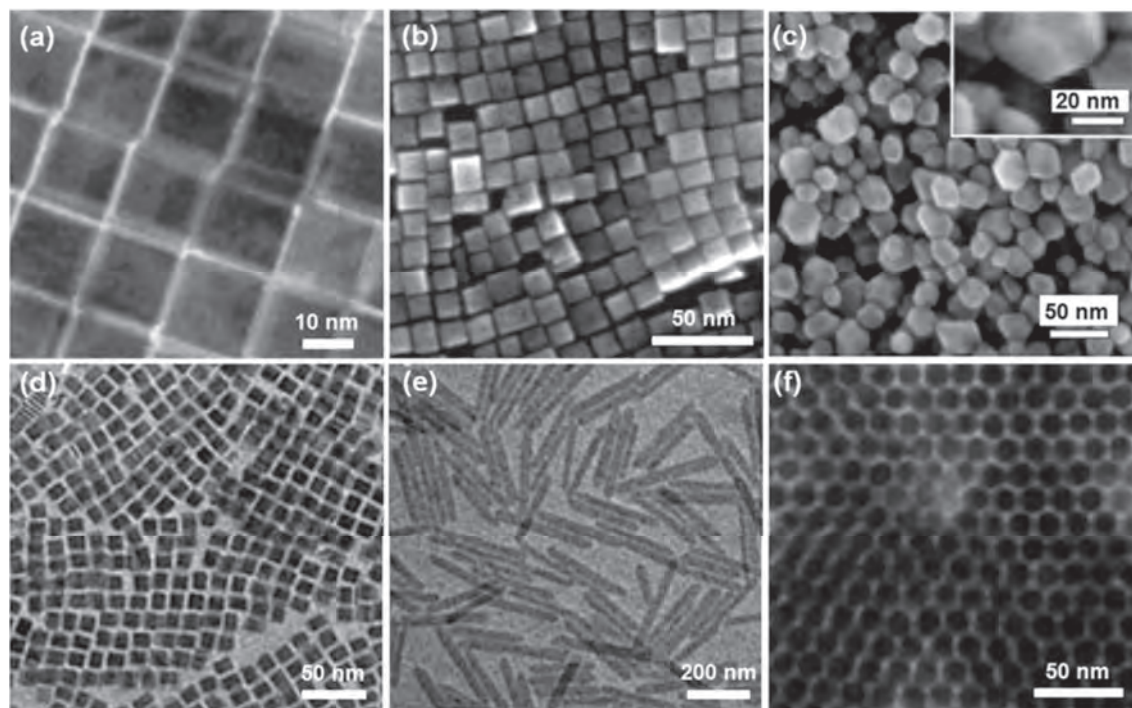


Fig. 4. Representative morphologies of CeO₂ synthesized by solvothermal methods (a) TEM image of CeO₂ nanocubes, adapted with permission from Ref. [76]. Copyright © 2006, American Chemical Society. (b) TEM image of CeO₂ nanocubes, adapted with permission from Ref. [77]. Copyright © 2012, Royal Society of Chemistry. (c) TEM image of CeO₂ truncated octahedra, adapted with permission from Ref. [77]. Copyright © 2012, Royal Society of Chemistry. (d–f) TEM images of square CeO₂ nanoplates, elongated CeO₂ nanoplates, and round CeO₂ nanoplates, respectively, adapted with permission from Ref. [78]. Copyright © 2012, WILEY-VCH Verlag GmbH & Co. KGaA, Weinheim.

nanorods (Fig. 2g and h) [73]. Recently, nanostructured ceria could be hydrothermally prepared using the green deep eutectic solvent reline in the presence of SDS surfactants, which allows the facile morphology and porosity control in one of the less energy-intensive routes reported to date [75]. In the absence of water, only CeO₂ nanoparticles were obtained under any synthetic

temperatures. In contrast, the increased amount of water drove a morphological change of the as-synthesized CeO₂ nanostructures from nanoparticles to nanowires, suggesting that water was functioned as the directing agent [75]. Monodispersed flowerlike CeO₂ microspheres (Fig. 2i) could also be synthesized by the simultaneous polymerization-precipitation reaction, metamorphic

reconstruction, and mineralization under hydrothermal conditions followed by calcination [74]. The obtained CeO_2 microspheres usually consisted of 20- to 30-nm-thick nanosheets as the petals. Importantly, they were found to have the open three-dimensional (3D) porous and hollow structure, exhibiting the large surface area, large pore volume, and good thermal stability.

Recently, there is a surfactant-free hydrothermal method operated at low pressures which has been successfully developed to synthesize porous nanorods of CeO_2 (PN- CeO_2) [37]. The preparation involves a two-step hydrothermal process (Fig. 3). In the first step, a low pressure of ~ 1.2 atm is critical for the formation of a $\text{Ce}(\text{OH})_3/\text{CeO}_2$ nanorod precursor. Then, a subsequent hydrothermal step at a higher temperature (e.g. $> 160^\circ\text{C}$) would lead to the complete dehydration and oxidation of $\text{Ce}(\text{OH})_3$ in the precursor nanorods and induce formation of porous nanorods successively. The unaltered rod-like morphology may be attributed to the robustness of precursor nanorods surviving through the dehydration, oxidation, and accompanied structure reorganization in the hydrothermal treatment.

3.2. Solvothermal synthesis in the presence of capping agents

Despite the simplification of the hydrothermal method, its controllability on the geometries and morphologies of CeO_2 nanostructures is still insufficient for practical utilizations. Thus, the solvothermal synthesis in the presence of various capping agents has been developed in order to realize this purpose. For example, a shape- and size-controllable synthesis of CeO_2

nanocubes enclosed by six (200) planes was achieved by a rationally designed one-pot approach (Fig. 4a) [76]. The 2D and 3D self-assembly of CeO_2 nanocubes was formed by the oriented aggregation-mediated precursor growth on the substrates. Both the shape and size of CeO_2 nanostructures could then be tuned conveniently by adjusting the concentrations of reactants and stabilizing agents (i.e. oleic acid) as well as the water/toluene molar ratios. Also, Wang et al. was able to synthesize CeO_2 nanocubes and CeO_2 truncated octahedra in the presence of various capping agents in an alkaline environment [77]. These nanocubes were made in the presence of oleic acid as the capping agent and using $\text{Ce}(\text{N}(\text{O}_3)_3)_3 \cdot 6\text{H}_2\text{O}$ as the Ce source in an alkaline solution of tetramethylammonium hydroxide (TMAH) (Fig. 4b). The side lengths of the as-synthesized nanocubes enclosed with six (100) facets are in the range of 9–17 nm. Similarly, CeO_2 truncated octahedra were prepared using polyvinyl pyrrolidone (PVP) as the capping agent in the reaction system (Fig. 4c). The size of CeO_2 truncated octahedra surrounded with eight (111) and six (100) facets was ~ 17 nm. Also, ultrathin 2D CeO_2 nanoplates were successfully prepared by the thermal decomposition of cerium acetate at $320\text{--}330^\circ\text{C}$ in the presence of oleic acid and oleylamine as the capping agent and the surfactant, respectively (Fig. 4d–f) [59]. The morphology of nanoplates can be easily controlled by the reaction parameters (e.g., precursor ratio, reaction time, and temperature).

3.3. Template-assisted synthesis

The size, surface area, and shape of CeO_2 nanostructures can also

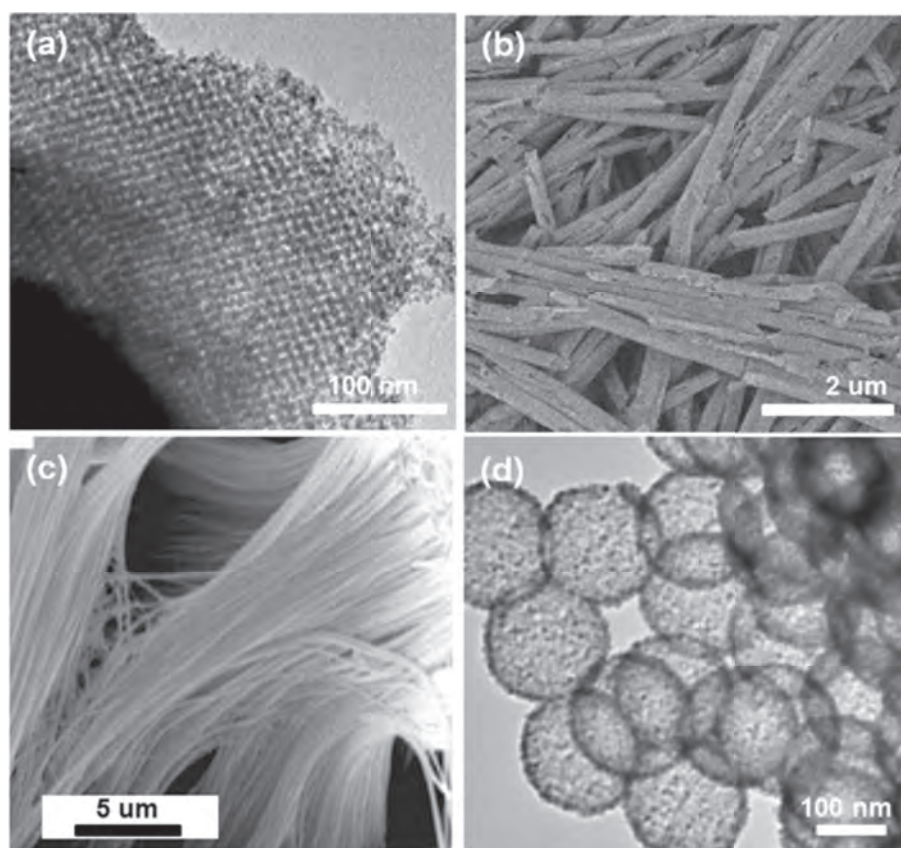


Fig. 5. Representative morphologies of CeO_2 synthesized by template methods (a) TEM image of the template-free CeO_2 samples, adapted with permission from Ref. [79]. Copyright © 2003, Royal Society of Chemistry. (b) SEM image of CeO_2 nanotubes, adapted with permission from Ref. [82]. Copyright © 2009, American Chemical Society. (c) SEM image of CeO_2 nanowire arrays, adapted with permission from Ref. [83]. Copyright © 2004, Elsevier B. V. All rights preserved. (d) TEM image of porous hollow CeO_2 microspheres, adapted with permission from Ref. [84]. Copyright © 2012, Springer International Publishing AG.

Table 2
Summary of surface control methods.

# Method	Conditions	Effect on surface structure	application	Ref.
1 High temperature annealing under vacuum	Annealing in vacuum at different temperatures	Increasing lattice defect and oxygen storage capacity (OSC)	–	[86]
2 Hydrogen treatment	Annealing at 700, 800 and 900 °C with mixture gas of nitrogen and hydrogen for 2 h, respectively	Increased surface Ce^{3+} content and concentrations of oxygen vacancy, modulated optical property	Up- and down-conversion	[87]
3 Thermal activation in a gas mixture of nitrogen and oxygen	Annealing at 400 °C with nitrogen-oxygen mixture gas under vacuum of 0.1 Torr	Changes in the surface Ce^{3+} fractions of the nanostructured CeO_2 and in the coordination numbers of the surface cerium atoms	CO oxidation	[88]
4 <i>In situ</i> and <i>ex situ</i> thermal annealing treatments	Annealing at 375 and 800 °C in an oxidizing environment	Disordered small oxygen defects and small vacancy clusters, increased lattice strain and expansion, formation of polyhedral nanocavities	–	[89]
5 EB irradiation	EB energy of 0.7 MeV and an initial EB current of 2 mA/s in water at room temperature and atmospheric pressure.	More surface Ce^{3+} species and increased the concentration of surface defects	Photocatalysis	[90]
6 Wet chemical redox etching	Treating with ascorbic acid and hydrogen peroxide alternatively for different cycles	Larger surface area, more surface Ce^{3+} fraction, higher concentration of oxygen vacancy	CO oxidation	[92]
7 Pressure control	Hydrothermal under different pressures and oxygen/nitrogen ratios	Controllable length/diameter ratio, surface area, surface Ce^{3+} fraction and OSC value	CO oxidation and nitrile hydrolysis	[93]

be modulated by using templates during the synthesis such as organic macromolecules, surfactants, nanometer-sized granules of silica, polycarbonate membranes, and anodic alumina (AAO) membranes. Among all, mesoporous silica templates have been successfully employed to fabricate the highly ordered mesoporous CeO_2 with uniform mesopore sizes [79]. The synthesis involves the incorporation of cerium precursors into a mesoporous silica

template, subsequent conversion of precursors into CeO_2 , and final removal of the silica template. The morphology of obtained mesoporous CeO_2 is very similar to that of silica templates (Fig. 5a). Importantly, these mesoporous CeO_2 are found to exhibit the remarkable thermal stability at 973 K. Also, nanoscaled CeO_2 with a large surface area of $200 \text{ m}^2 \text{ g}^{-1}$ could be prepared using cetyltrimethyl ammonium bromide (CTAB) as the templating agent [80],

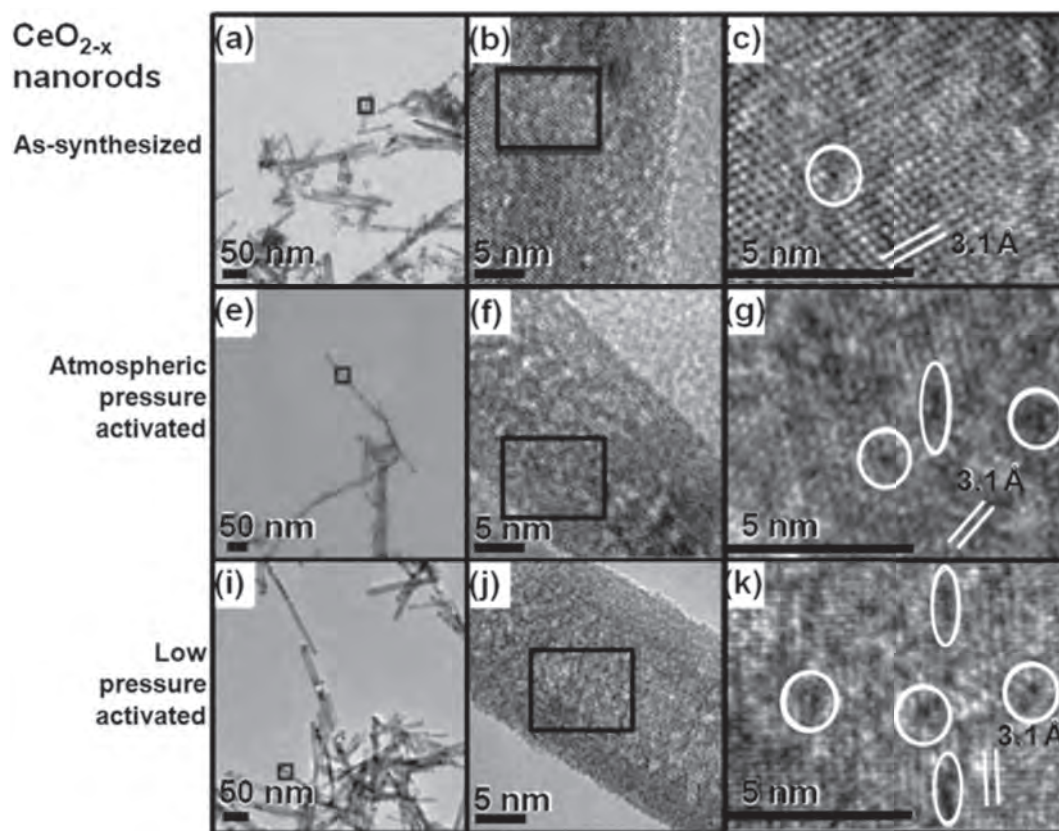


Fig. 6. Surface properties of CeO_2 modulated by the thermal activation method in a gas mixture of nitrogen and oxygen at various pressures. (a–c) TEM images of the as-synthesized CeO_2 nanorods; (e–g) TEM images of the thermally activated CeO_2 nanorods at atmospheric pressure; and (i–k) TEM images of the thermally activated CeO_2 nanorods at low pressure (0.1 Torr). The left column shows the typical TEM images of CeO_2 nanorods. Squares in the figures show approximate zoomed-in area of interest for adjacent figures in the right column. The middle column shows HRTEM images of individual nanorods. The right column illustrates the approximate locations of some oxygen vacancy defects: point oxygen vacancies (circles) and linear oxygen vacancies (ovals). Adapted with permission from Ref. [87]. Copyright © 2011, American Chemical Society.

Table 3

Parameters of the local structure around Ce atoms of low pressure-activated ceria nanorods, nanoparticles, and bulk samples obtained from the curve fitting of Ce L₁-edge EXAFS. Adapted with permission from Ref. [88]. Copyright © 2011, American Chemical Society.

CeO _{2-x} sample	neighboring atom	N	R(Å)
theoretical	O	8	2.34
	Ce	12	3.83
	O	24	4.48
nanorod	O	6.3 ± 0.1	2.294 ± 0.005
	Ce	7.4 ± 0.4	3.815 ± 0.005
	O	14.7 ± 1.2	4.515 ± 0.005
nanoparticle	O	6.5 ± 0.1	2.299 ± 0.005
	Ce	6.5 ± 0.3	3.841 ± 0.005
	O	15.5 ± 1.3	4.464 ± 0.005
bulk	O	8 ± 0.1	2.316 ± 0.005
	Ce	12 ± 0.3	3.82 ± 0.005
	O	24 ± 1.2	4.48 ± 0.005

^aN is the coordination number. R is the average interatomic distance between Ce and its neighboring atoms. Uncertainties were estimated by the double-minimum residue $2\chi^2$ method.

while polycrystalline CeO₂ nanowires were synthesized via a solution-phase route with sodium bis(2-ethylhexyl) sulfosuccinate as the templating agent [81]. It is noted that the as-synthesized nanowires were composed of many tiny grains at different orientations. At the same time, CeO₂ nanotube arrays (Fig. 5b) could as well be successfully fabricated by a potentiostatic electrochemical deposition from a cerium nitride solution, where the AAO membranes were served as the hard templates [82]. As expected, these CeO₂ nanotubes showed a polycrystalline structure with a thin wall of 6 nm and uniform diameter. In addition, using the similar AAO membranes as templates, ordered CeO₂ nanowire arrays (Fig. 5c) could also be prepared [83]. During the deposition process, Ce³⁺ and C₂O₄²⁻ species conversely migrated into the hexagonally ordered nanochannels of AAO membranes and reacted inside the channels to form Ce₂(C₂O₄)₃ precursors configured into the one-dimensional nanowire geometry along the axial direction. The subsequent thermal annealing of Ce₂(C₂O₄)₃/AAO would result in the formation of CeO₂ nanowires confined in the pores of AAO templates. On the other hand, porous hollow CeO₂ microspheres (Fig. 5d) with the good monodispersion and uniformity in size were synthesized, in which the negatively charged polystyrene (PS) microspheres were used as the hard templates [84], whereas ultrathin CeO₂ sheets were also synthesized from the hard template of ultrathin CeCO₃OH sheet precursors by a well-controllable thermal annealing process in air [85]. All these examples demonstrate the versatility of different template-assisted methods for the synthesis of various CeO₂ nanostructures.

4. Surface control on CeO₂ nanomaterials

In general, the synthetic method would dictate the surface properties of obtained CeO₂ nanostructures, including their specific surface area, surface Ce³⁺ fraction, and oxygen vacancy concentration. During the formation of CeO₂ and their related precursors, various strategies of doping foreign elements as well as controlling the morphologies and the exposed facets of these nanostructures are also extensively studied. For example, different post-synthesis treatments, including the high-temperature annealing processes under selected temperatures, gas atmospheres and pressures, and electron beams (EBs) and chemical based modifications have been widely developed in order to regulate the surface properties of the nanostructures [86–88]. Table 2 summarizes the recent efforts on regulating the surface properties of CeO₂.

Mamontov et al. demonstrated the dependence of lattice defect

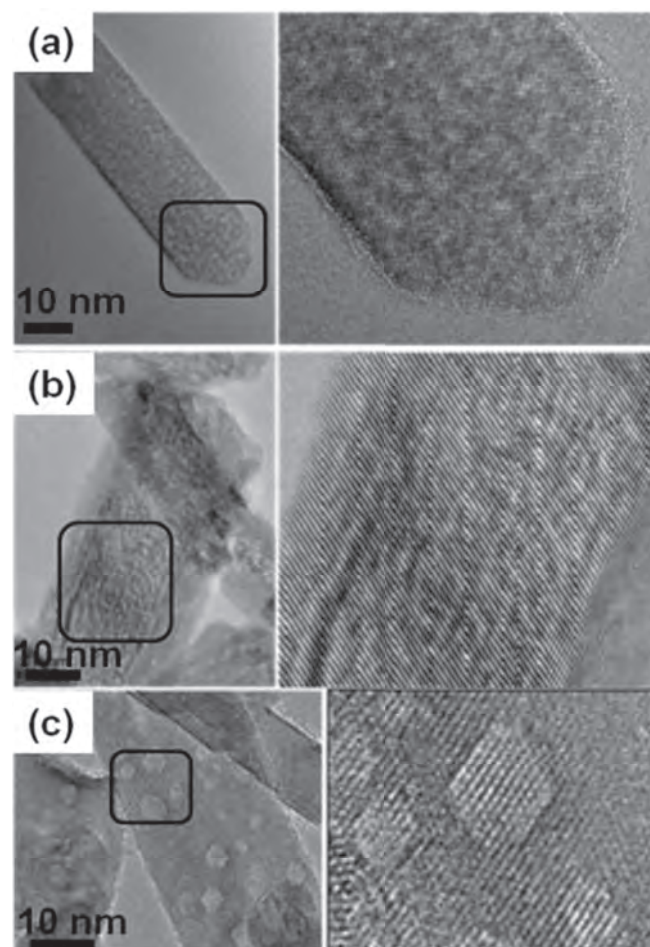


Fig. 7. Surface control on CeO₂ nanorods by thermal annealing. *Ex situ* annealing: HRTEM images showing various amounts of imperfect crystallinity (image pairs with zoom-in of black rectangles): (a) As-synthesized CeO₂ nanorods: Rod direction <110>. (b) CeO₂ nanorods annealed at 325 °C in air. (c) CeO₂ nanorods annealed at 800 °C: rod direction for (b, c) is <211>. The viewing directions for (a–c) are of <110> type. Adapted with permission from Ref. [89]. Copyright © 2015, Royal Society of Chemistry.

formation and OSC on the annealing temperature under vacuum, suggesting that the structural defect concentration is maximized at medium annealing temperatures of 300–600 °C [86]. Also, hydrogen treatments on the erbium-doped CeO₂ nanoparticles were observed to lead to the chemical reduction of Ce⁴⁺ as well as the increase in the surface Ce³⁺ content and the concentration of oxygen vacancy [87]. Thus, they exhibited enhanced optical properties with the higher up-conversion and down-conversion efficiencies. The manipulation on the oxygen vacancies of CeO₂ nanoparticles and nanorods could also be realized by the thermal activation method in a gas mixture of nitrogen and oxygen at a low pressure of 0.1 Torr and atmospheric pressure, respectively (Fig. 6). All these activations would lead to the changes in surface Ce³⁺ fractions of the nanostructured CeO₂ and in coordination numbers of the surface cerium atoms (Table 3) [88]. Moreover, the process pressure was known to considerably affect the surface properties of fabricated CeO₂. Low-pressure treatments produced CeO₂ with a higher surface Ce³⁺ fraction, while those under atmospheric pressure resulted in a relatively lower surface Ce³⁺ fraction but still higher than that of the untreated CeO₂. Thus, the enhanced catalytic activity for CO oxidation reaction was observed for the CeO₂ based catalysts treated at various pressures, which may be attributed to the increase in surface defects in terms of higher surface

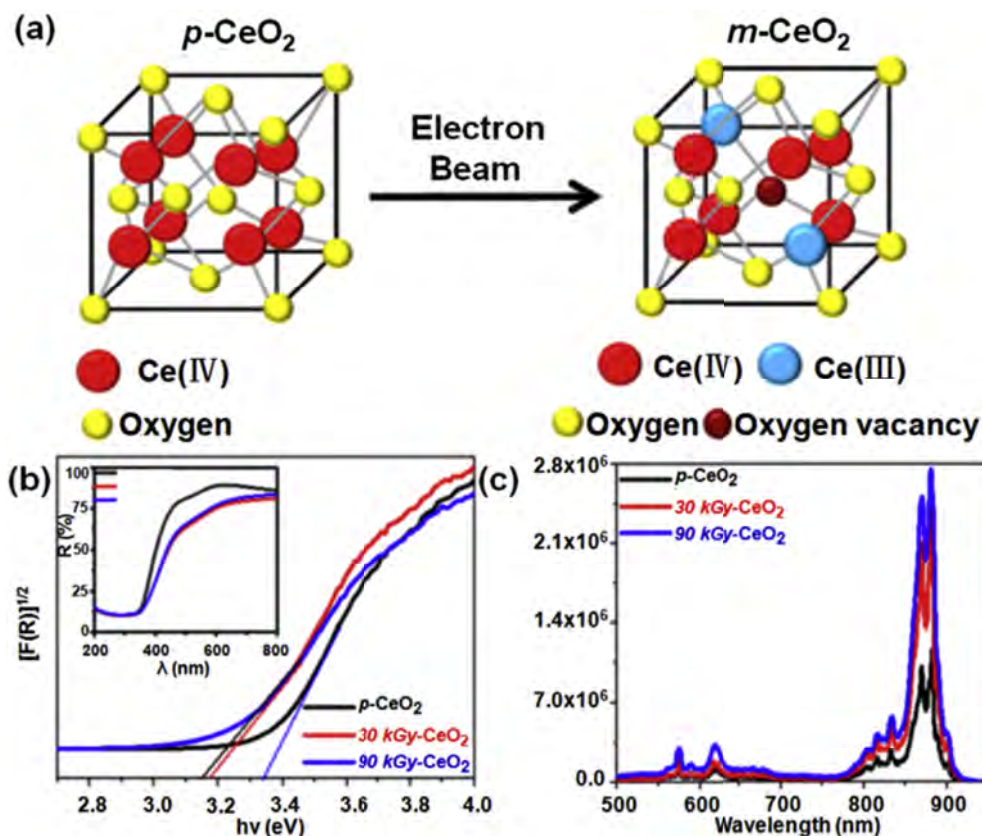


Fig. 8. Surface properties of CeO₂ controlled by EB irradiation. (a) Schematic model illustrating the change in crystalline structure of CeO₂ due to the formation of Ce(III) and oxygen vacancy after EB irradiation. (b) $[F(R)]^{1/2}$ versus $h\nu$ plot of p-CeO₂, 30 kGy-CeO₂, and 90 kGy-CeO₂ nanostructures. (Inset) UV–vis diffuse reflectance spectra. (c) PL spectra of p-CeO₂, 30 kGy-CeO₂, and 90 kGy-CeO₂ nanostructures. Adapted with permission from Ref. [90]. Copyright © 2014, American Chemical Society.

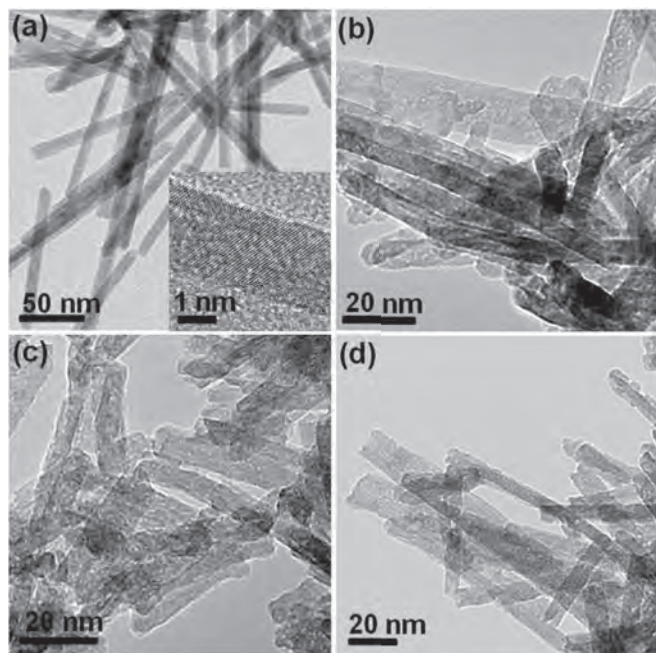


Fig. 9. Surface control by wet chemical redox etching. TEM images of CeO₂ nanorods. (a) As-synthesized CeO₂ nanorods (inset: HRTEM image of CeO₂ nanorods). (b) CeO₂ nanorods after one cycle, (c) four cycles, and (d) eight cycles of oxidation/reduction treatment. Adapted with permission from Ref. [92]. Copyright © 2015, Royal Society of Chemistry.

Ce³⁺ fractions.

Recently, the tailorable structures and surface properties of CeO₂ nanorods were also achieved by the *in situ* and *ex situ* thermal annealing treatments (Fig. 7) [89]. Two different types of oxygen-related defects were found under TEM observations: (1) the disordered oxygen defects and (2) the vacancy clusters. Both types of defects would increase the lattice strain and the expansion of as-synthesized CeO₂ nanorods. In addition, the thermal treatments would lead to the formation of polyhedral nanocavities within the nanorods due to the oxygen migration within the surface defect clusters. Molecular dynamic simulation also confirmed the agglomeration of oxygen vacancies within the as-prepared nanorods, which was ascribed to the evolution of nanocavities on the surface of CeO₂ nanorods.

However, the commonly used high-temperature treatment approach, somehow, is destructive because of the fragile CeO₂ nanostructures at high temperatures, which leads to the apparent sintering and consequent loss of specific surface areas as well as shielding/blocking of the surface active sites. Several novel strategies, including various physical and chemical methods, were then successfully developed to regulate the surface properties of CeO₂ with the aim to modulate its catalytic activity and selectivity.

The EB irradiation method was then developed to create more surface defects on the CeO₂ surface [90]. Various doses of EB irradiation received on CeO₂ nanoparticles could change their surface chemical states and compositions. A high dose generated more surface Ce³⁺ species and increased the concentration of the surface defects (Fig. 8). The defect-engineered CeO₂ nanoparticles would then facilitate their photocatalytic activity under visible light by enhancing the electron transfer and suppressing the recombination

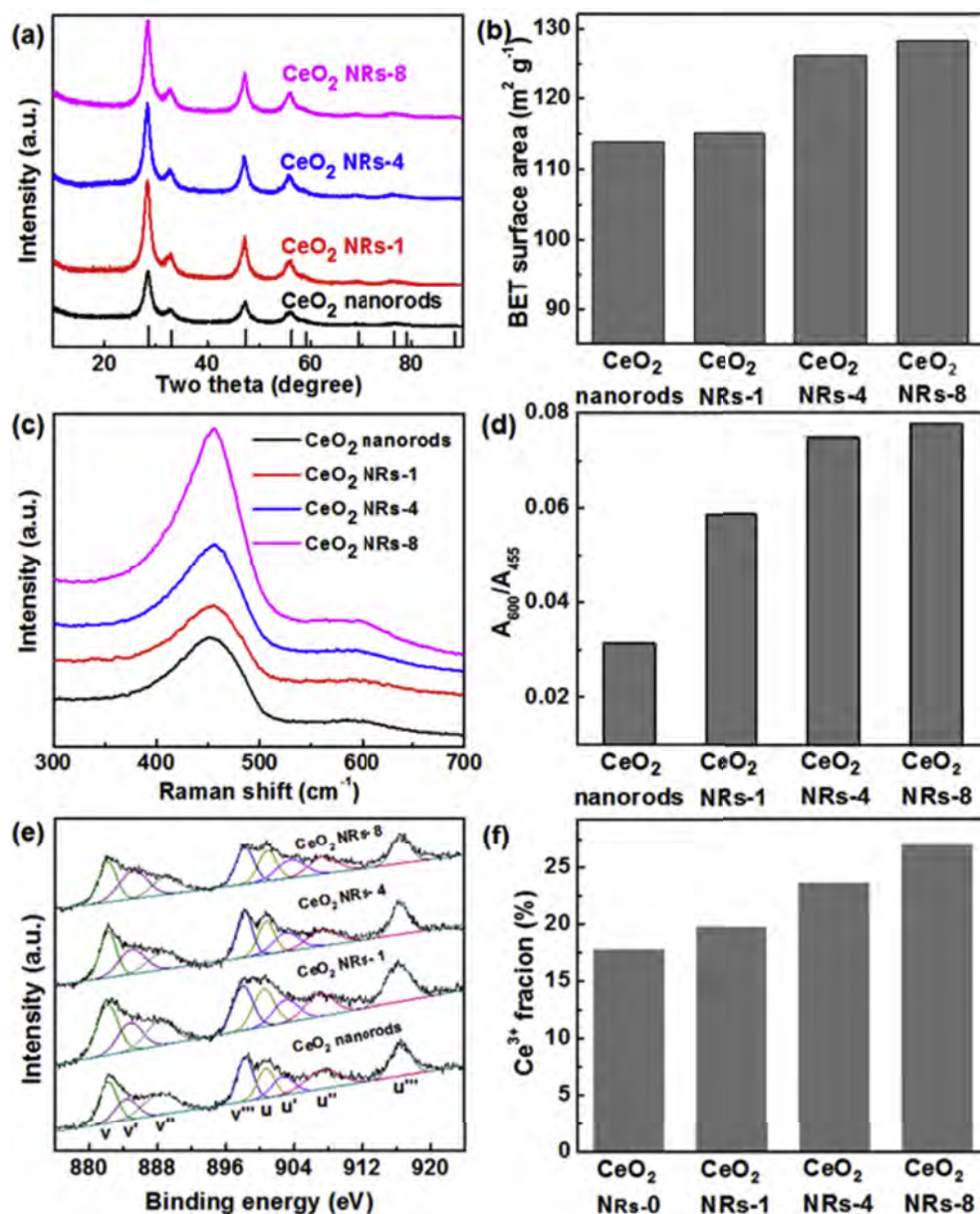


Fig. 10. Surface properties of CeO₂ nanorods treated with various cycles of the wet chemical etching. (a) XRD patterns, (b) Specific surface areas, and (c) Raman spectra of the as-synthesized CeO₂ nanorods and the treated CeO₂ nanorods with various cycles (1, 4, and 8) of the chemical reduction/oxidation. (d) Area ratio of Raman peaks at 455 and 600 cm⁻¹ for all CeO₂ nanorods derived from their Raman spectroscopic profiles, as shown in (c). (e) XPS spectra of Ce 3d core level regions, and (f) Surface Ce³⁺ fractions of the as-synthesized CeO₂ nanorods and the etched CeO₂ nanorods with 1, 4, and 8 reduction/oxidation cycles. Adapted with permission from Ref. [92]. Copyright © 2015, Royal Society of Chemistry.

of photogenerated holes and electrons.

Also, the post-treatment induced modulation of surface properties of CeO₂ and their morphology modification could be realized by the wet chemical redox etching approach [91]. Recently, our group demonstrated a facile wet chemical method to engineer the surface properties of CeO₂ nanorods [92]. In this work, ascorbic acid (AA) and hydrogen peroxide (H₂O₂) were functioned as the reducing agent and oxidizing agent, respectively, to react with the surface Ce³⁺ and Ce⁴⁺ species of CeO₂ nanorods. The processed CeO₂ nanorods using AA and H₂O₂ alternatively for various redox etching cycles could not only deliver the morphology evolution from a smooth surfaced to a rough surfaced structure but also give the controllable surface properties there (Fig. 9).

After the chemical etching process, the fluorite crystal structure and the rod-like morphology of CeO₂ nanorods were preserved,

similar to that of the as-synthesized CeO₂ nanorods (Fig. 10a). Importantly, the surface properties of CeO₂ can be effectively controlled by the number of chemical etching cycles. The specific surface areas of etched nanorods were increased to 115.1, 126.4, and 128.3 m² g⁻¹ after 1, 4, and 8 cycles of the treatments (Fig. 10b), respectively. Raman spectra also illustrated that a higher number of chemical reduction/oxidation cycles would lead to an increase in concentration of surface oxygen vacancies (Fig. 10c and d). The surface Ce³⁺ fractions of the processed CeO₂ nanorods was found to increase steadily with the increasing number of chemical redox cycles (Fig. 10e), which was consistent with the morphological changes observed under TEM and the evolutions of the measured peaks in their Raman spectra (Fig. 10f). Hence, the chemical etching process is known to be a facile approach to manipulate the controllable surface properties of CeO₂ for the desired applications.

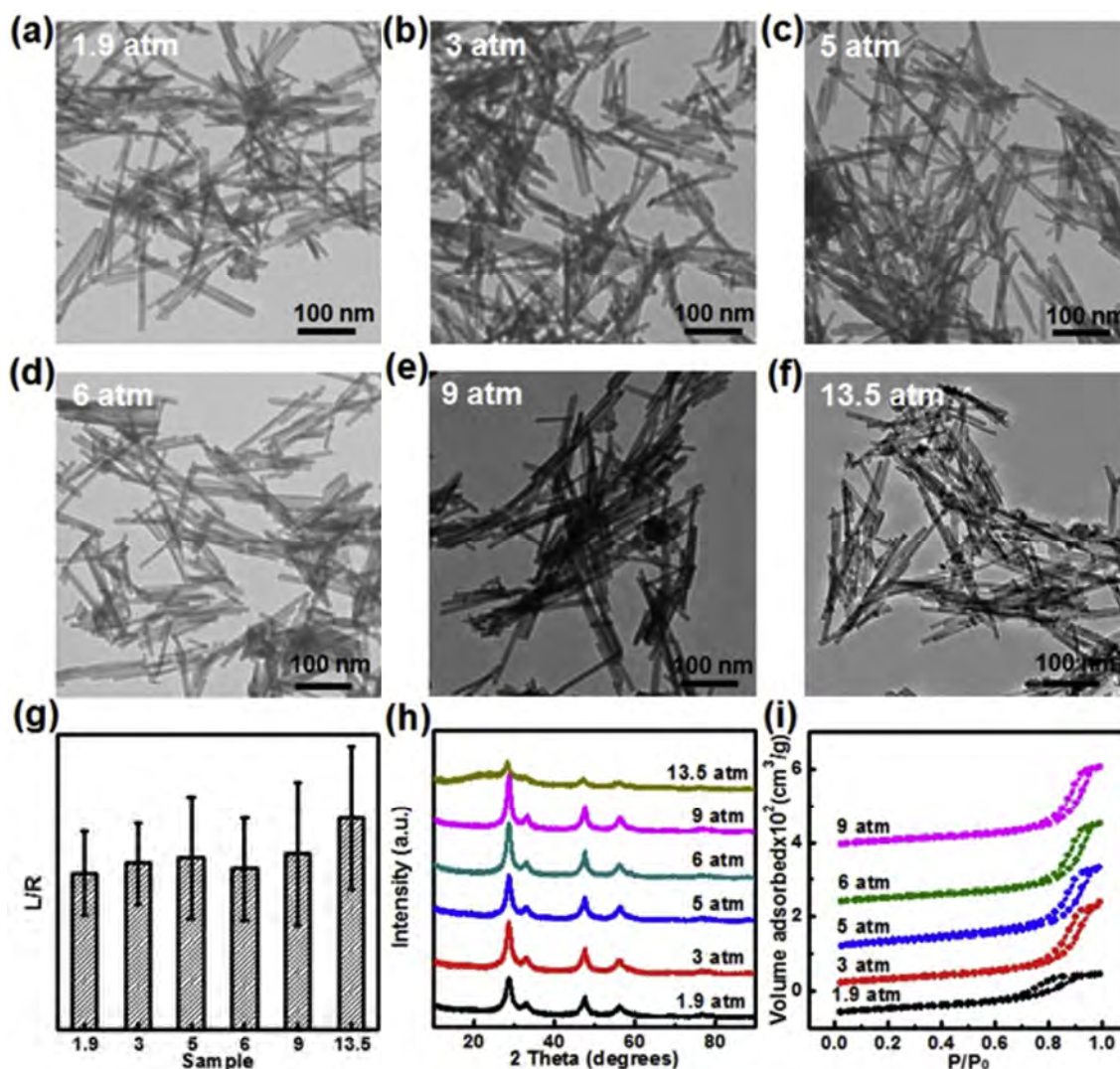


Fig. 11. Structural characterizations of CeO₂ nanorods synthesized at various pressures. TEM image of CeO₂ nanorods at (a) 1.9, (b) 3.0, (c) 5.0, (d) 6.0, (e) 9.0, and (f) 13.5 atm. (g) Plot of the L/W ratios of CeO₂ nanorods vs various pressures of the reaction vessels. (h) XRD patterns of CeO₂ nanorods. (i) N₂ adsorption-desorption isotherms of CeO₂ nanorods. Adapted with permission from Ref. [93]. Copyright © 2016, American Chemical Society.

Table 4

Structural characteristics of CeO₂ nanorods synthesized at various pressures. Adapted with permission from Ref. [93]. Copyright © 2016, American Chemical Society.

Pressure (atm)	Ce ³⁺ (%)	BET (m ² g ⁻¹)	OSC (mmol O ₂ per g)
1.9	17.6	93.4	167.9
3	21.5	106.2	211.9
5	23.4	105.6	280.8
6	22.3	98.9	238.1
9	17.7	96.8	183.9
13.5	16.4	92.7	181.2

Another effective strategy to controllably adjust the surface properties of CeO₂ nanorods is to regulate the synthetic pressures and the partial pressure of oxygen in reaction vessels during the hydrothermal processes [37,93]. Neither the air pressures nor the oxygen partial pressures would alter the rod-like morphology of CeO₂ except the different length/diameter ratio (Fig. 11). However, their surface properties, including the surface Ce³⁺ fractions, surface areas, and OSC values, could be effectively modulated by the total pressure and partial pressure of oxygen as summarized in

Table 4. An optimized pressure of 5.0 atm with a relatively low oxygen partial pressure was observed to produce CeO₂ nanorods with the highest concentration of oxygen vacancy, highest surface fraction of Ce³⁺ species, and largest value of OSC [92]. Generally, the growth mechanism of CeO₂ nanorods is considered as the formation of anisotropic rod-like Ce(OH)₃ nuclei followed by the subsequent dissolution/recrystallization process of the nuclei [70,71]. Thus, the dissolution/recrystallization rate of Ce(OH)₃ and the solubility of O₂ in the solution under various pressures essentially determine the surface properties of CeO₂ nanorods. These two factors would make CeO₂ nanorods reaching their maximum concentration of the surface defects at 5.0 atm. Therefore, the pressure is believed to play a considerable role in tailoring the surface Ce³⁺ fraction and the surface-bound defects of CeO₂ nanorods.

When the synthetic pressure was inversely reduced to ~1.2 atm, the hydrothermal approach would produce the rod-like precursor, composed of 41.5% Ce(OH)₃ and 58.5% cubic fluorite CeO₂, with a diameter of ~8 nm and a length of ~60 nm, as illustrated in Fig. 12. The second hydrothermal treatment over 160 °C would then lead to a new form of PN-CeO₂, which has a very large surface area of 144 m²/g and a high surface Ce³⁺ fraction of 32.8%. Impressively,

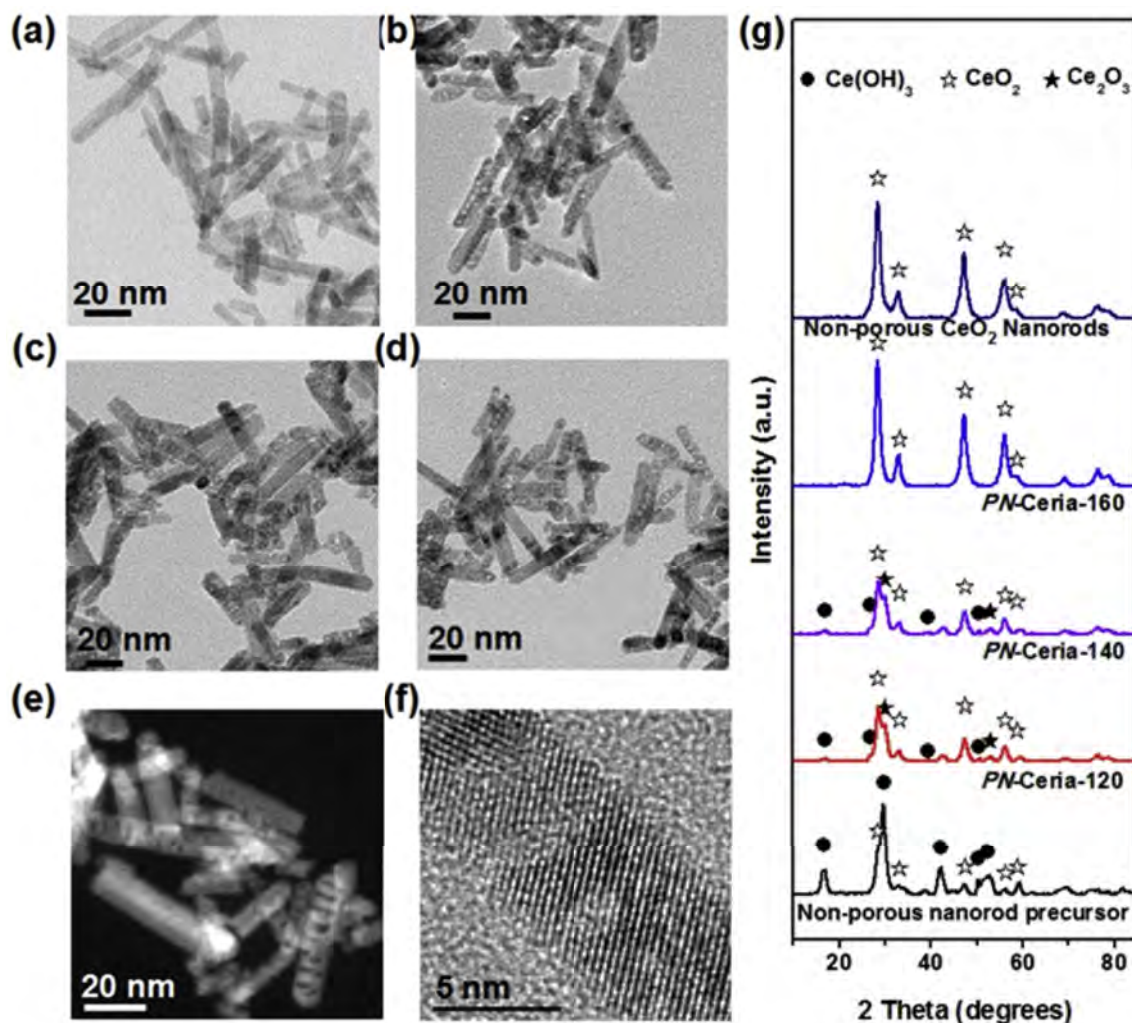


Fig. 12. Structural characterizations and surface properties of PN-CeO₂ (a) TEM image of the nonporous nanorod precursor. (b) TEM image of PN-CeO₂-120. (c) TEM image of PN-CeO₂-140. (d) TEM image of PN-CeO₂-160. (e) Dark-field TEM image of PN-CeO₂-160. (f) HRTEM image of PN-CeO₂-160. (g) XRD patterns of ceria-based nanostructures. Adapted with permission from Ref. [36]. Copyright © 2014, Royal Society of Chemistry.

Table 5

Structural characteristics of nanoceria synthesized at various conditions. Adapted with permission from Ref. [37]. Copyright © 2014, Royal Society of Chemistry.

Sample	Ce ³⁺ fraction (%)	BET(m ² g ⁻¹)	OSC (mmol O ₂ per g)
PN-Ceria-120	19.1	109	—
PN-Ceria-140	24.3	120	—
PN-Ceria-160	30.8	141	900.2
PN-Ceria-R-160	21.6	137	831.2
Nonporous nanorods	14.5	107	167.9
Nanocubes	16.7	12.2	84.2
Nanooctahedra	19.0	8.4	152.7

PN-CeO₂ also delivers an extremely large OSC value up to ~900 μmol O₂/g, being over four times higher than the values reported for any other nanostructured forms of ceria (Table 5). Furthermore, the surface properties of PN-CeO₂ can also be regulated by the hydrothermal temperatures at the second step. Its morphological features can as well be well preserved. These porous nanorods could reach the similar surface areas of 141, 131, and 122 m²/g for the catalysts synthesized at 160, 180, and 200 °C, respectively. The surface Ce³⁺ fractions and the concentrations of oxygen vacancy would generally decrease with the increasing

hydrothermal temperature during the reaction.

5. Catalytic performance

5.1. CO oxidation

Removal of carbon monoxide (CO) from a specific gas atmosphere is of great importance in daily life and industrial applications. For example, CO in the exhaust gas emission from vehicles due to the incomplete combustion of gasoline pollutes the environment and threatens the human health directly. Also, industrial production of hydrogen is usually done by the thermal reformation of coal, hydrocarbons or alcohols via the following reaction: fuels + O₂ + H₂O → CO_x + H₂. This reforming process always produces CO and CO₂. The water-gas shift (WGS) reaction (CO + H₂O → CO₂ + H₂) is then used to remove most of the accompanied CO [94]. However, ~1% of CO remains in the typical WGS effluent gas, which is a negative factor for any further catalytic applications. The CO residue can poison majority of the metal-based catalysts. Thus, it is necessary and important to remove CO to a trace level below 10 ppm. In this regard, CeO₂ is considered as a promising candidate for CO oxidation as both additive and catalytic

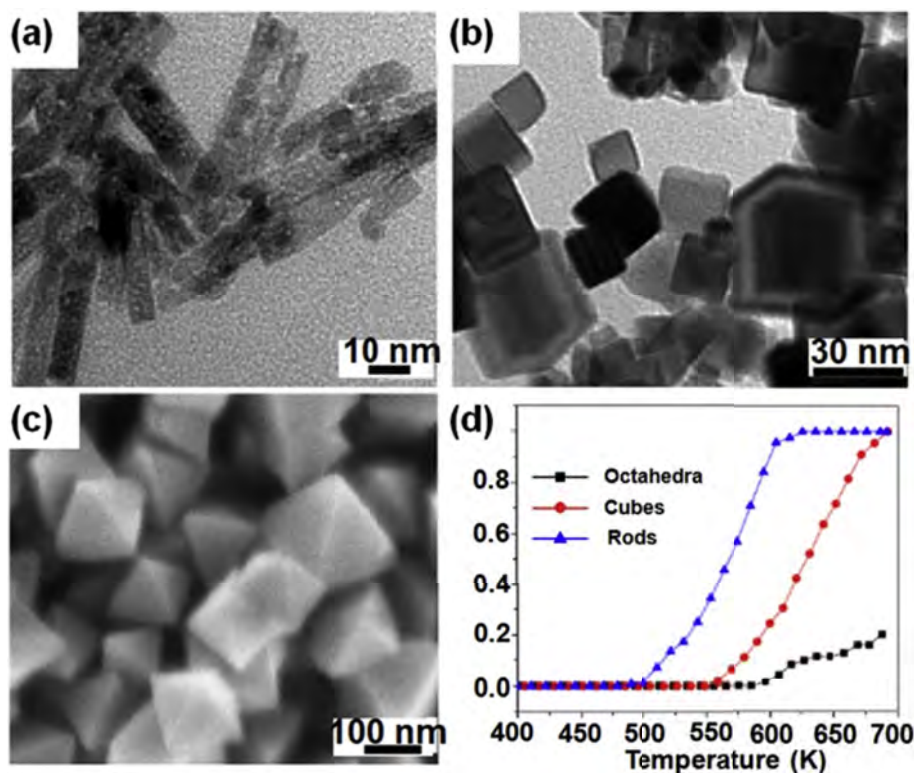


Fig. 13. (a) TEM image of ceria rods, (b) TEM image of cubes, and (c) SEM image of octahedra after CO oxidation to 673 K, and (d) light-off curves for CO oxidation over ceria rods, cubes, and octahedra. Adapted with permission from Ref. [104]. Copyright © 2012, Elsevier B. V. All rights preserved.

active component because of its reversible redox chemistry, large OSC value, and good thermal durability. Although many studies have demonstrated the excellent catalytic properties of CeO₂-incorporated noble metals (Pt, Au, and Pd, *etc.*), metal oxides (CuO, and Co₃O₄, *etc.*), CeO₂ and transition metal doped CeO₂ catalysts for CO oxidation as well as preferential CO oxidation in the presence of excessive H₂ have been rarely studied [32,94–103]. Herein, we emphasize on the relationship between CO oxidation activity and surface properties of pure CeO₂ catalysts.

CO oxidation reaction over CeO₂ usually precedes the Mars-van Krevelen mechanism, including the adsorption of CO on the top of surface Ce³⁺, the activation of CO by the lattice oxygen to form the intermediate COO*, the removal of CO₂ accompanied by the formation of oxygen vacancies, and the consequent annihilation of oxygen vacancies by gas phase oxygen [104]. Thus, the catalytic activity of CeO₂ for CO oxidation is well determined by its surface properties. In general, surface properties, such as the specific surface areas, surface Ce³⁺ fractions, surface planes, and oxygen vacancies are considered as the main factors to affect the performance of CeO₂ towards CO oxidation. CeO₂ catalysts with the features of high surface area, large concentration of surface defects, high mobility of lattice oxygen and low formation energy of oxygen vacancy can benefit CO oxidation. In this case, many efforts have been focused on the surface control of CeO₂.

Recently, several individual groups reported the significant effect of the exposed crystal planes of differently shaped CeO₂ catalysts on their CO oxidation activity, such as nanowires, nanorods, nanocubes, nanooctahedra, nanospindles, nanospheres, and nanotubes [37,104–107]. Overbury et al. studied the shape-activity relationships of various CeO₂ nanostructures for CO oxidation by using *in situ* diffuse reflectance infrared Fourier transform spectroscopy (DRIFTS) techniques (Fig. 13) [104]. The reactivity for CO oxidation is strongly surface dependent with the following trend:

nanorods > nanocubes > octahedral. The difference among surface oxygen vacancy formation energy, amount of low coordination sites and defects sites in various crystal planes of the differently shaped CeO₂ catalysts are recognized as the driving force of the surface-dependent catalytic behaviors for CO oxidation. The low oxygen vacancy formation energy and high mobility of lattice oxygen in CeO₂ (110) crystal plane (i.e. the dominated plane of CeO₂ nanorods) as well as the nature and amount of defects and low coordination sites of CeO₂ nanorods would enable the highest catalytic activity of CeO₂ nanorods for CO oxidation [102]. For the same reason, the similar surface-dependent catalytic phenomenon for Deacon process (i.e. a gas phase oxidation for converting HCl into Cl₂) catalyzed by CeO₂ was also observed [108–110]. Among CeO₂ catalysts with various morphologies, CeO₂ nanorods could deliver the highest catalytic activity and the best stability for Deacon oxidation [110].

To date, our group reported a new type of surface defect-abundant CeO₂ nanorods (PN-CeO₂) fabricated by a two-step hydrothermal method, which showed a very high catalytic activity for CO oxidation [37]. As shown in the catalytic light-off curve (Fig. 14), these PN-CeO₂ nanorods delivered the significantly improved CO oxidation activity and durability as compared with other CeO₂ catalysts. This improved CO oxidation performance of PN-CeO₂ can be attributed to the richer surface defects and the larger OSC value of the catalysts with abundant surface Ce³⁺ species as well as oxygen vacancies. PN-CeO₂ also showed a catalytic activity-temperature hysteresis between the light-off measurement spanning from low to high temperatures and the subsequent measurement covering from high to low temperatures (Fig. 14c). Such hysteresis can be rationalized in terms of the “overheating of active sites of the catalysts when decreasing the temperature of the reactor chamber.” The broad width (25 °C) of the hysteresis at 50% of CO conversion catalyzed by PN-CeO₂ was much larger than that

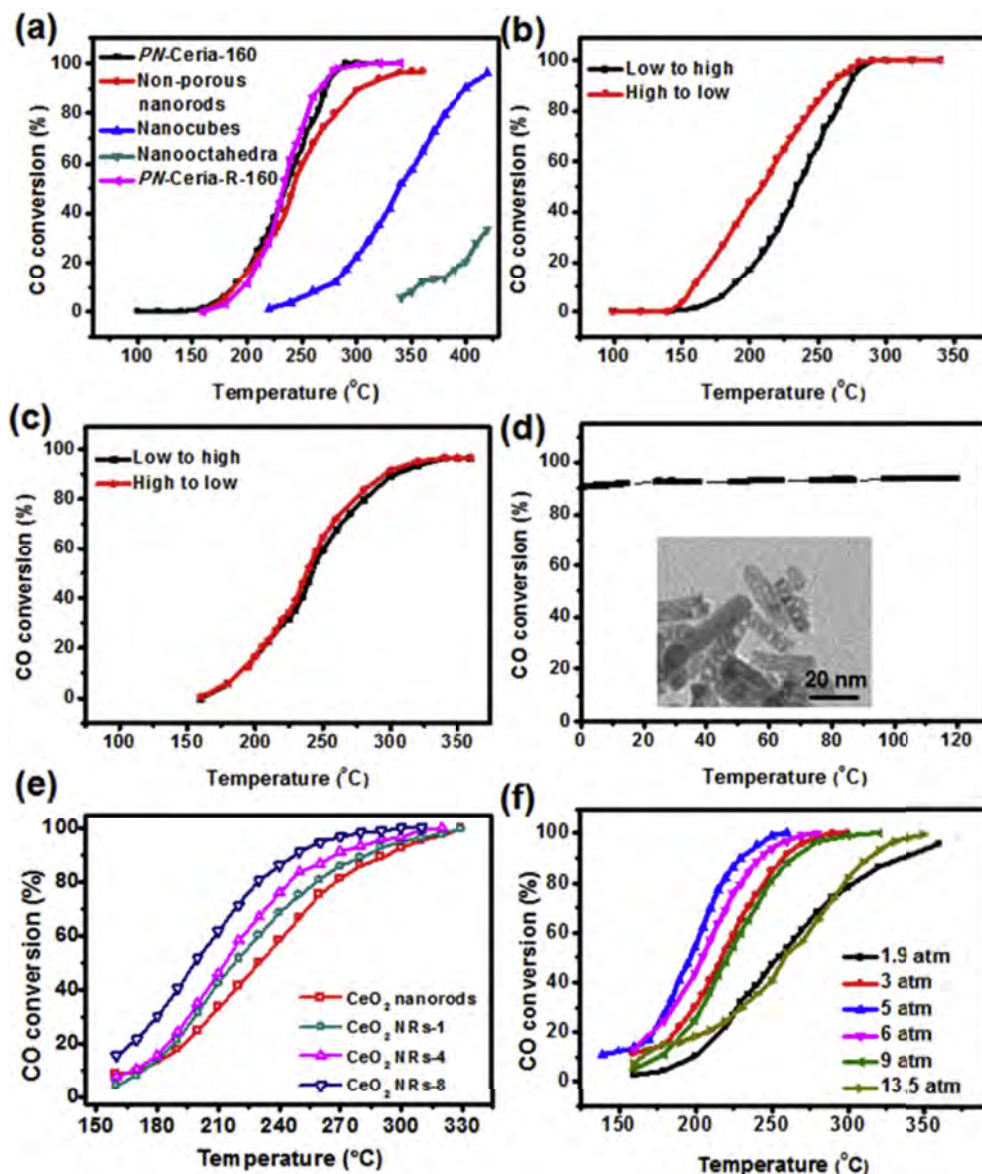


Fig. 14. CO oxidation performance of CeO₂ nanostructures. (a) CO oxidation catalyzed by various CeO₂ catalysts. (b) Temperature hysteresis of CO conversion on PN-CeO₂. (c) Temperature hysteresis of CO conversion catalyzed by nonporous CeO₂ nanorods. (d) Stability of PN-CeO₂ for CO oxidation at 270 °C. The inset is the TEM image of PN-CeO₂ after a 120-h stream-on-line running. Adapted with permission from Ref. [37]. Copyright © 2014, Royal Society of Chemistry. (e) CO oxidation catalyzed by CeO₂ nanorods with various chemical etching cycles. Adapted with permission from Ref. [92]. Copyright © 2015, Royal Society of Chemistry. (f) CO oxidation catalyzed by CeO₂ nanorods prepared under various pressures. Adapted with permission from Ref. [93]. Copyright © 2016, American Chemical Society.

(4 °C) by nonporous CeO₂ nanorods, reflecting the high CO oxidation activity of PN-CeO₂ with a larger width being associated with a more active catalyst. A similar catalytic performance of the surface-engineered CeO₂ for CO oxidation was also observed in the pressure-regulated CeO₂ nanorods. All results presented here indicate the strong correlation among the high surface area, large number of structural defects, and high fraction of Ce³⁺ of CeO₂ catalysts and their catalytic performance for CO oxidation.

Furthermore, the catalytic performance of CeO₂ nanorods regulated by the redox chemical etching methods [92] or pressure control [93] was also observed with the same tendency. As shown in Fig. 14e, the processed CeO₂ nanorods with the increased etching cycles would induce a steady increase in their surface areas, oxygen vacancies and surface Ce³⁺ fractions, which delivered the higher catalytic activity for CO oxidation. By optimizing the synthetic pressures, the CeO₂ nanorods prepared at 5.0 atm would present

the enhanced surface Ce³⁺ fractions and the larger concentration of oxygen vacancy, leading to the superior catalytic performance for CO oxidation (Fig. 14f).

Lately, atomically thin CeO₂ nanosheets with the abundant surface pits were exhibited with a very high catalytic activity for CO oxidation (Fig. 15). These ultrathin catalysts displayed the structural features of the existence of many pits (Fig. 15a). X-ray absorption spectroscopy revealed the fine structure of the nanosheets, in which there were many pits surrounding surface Ce sites with a very low average coordination number of 4.6. Fine structural characterizations showed that the coordination numbers of cerium species surrounded by the pits were mainly 4, 5, and 6 (Fig. 15d). These sites are widely recognized as the catalytically active sites for CO oxidation [85]. In this unique configuration, the CO molecules are preferentially adsorbed on top of the four-coordinated pits surrounding Ce sites, while the O₂ molecules yield a strong

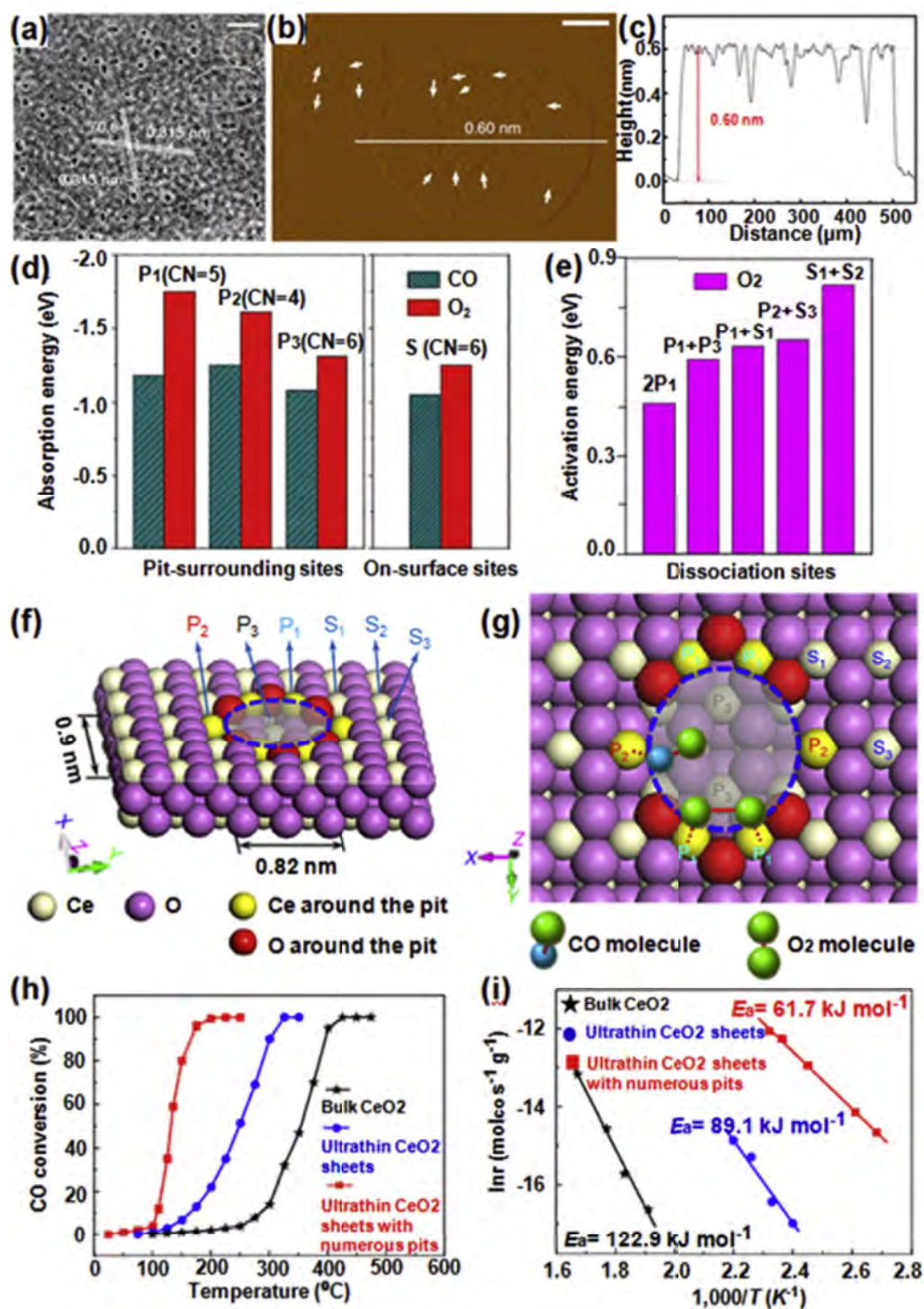


Fig. 15. CeO₂ nanosheets with abundant surface pits for CO oxidation and their catalytic mechanism. (a) HRTEM image, (b) AFM image, and (c) Height profiles along the white line indicated in (b) for the three-atom-thin CeO₂ sheets with numerous surface pits. The scale bars in (c) and (d) are 3 and 100 nm, respectively. The inset circles and arrows in (a) and (b) denote the presence of pits on their surface. (d) Calculated adsorption energies for CO and O₂ molecules on the pits surrounding Ce sites (P₁~P₃) and on surface Ce sites (S₁~S₃), and (e) Calculated activation energies for O₂ dissociation on adjacent Ce sites of ultrathin CeO₂ sheets with numerous pits; the coordination numbers of P₁, P₂, P₃, S₁, S₂, and S₃ are 5, 4, 6, 6, 6, and 6, respectively. (f) Overhead and (g) Top views of schematic structures for the three-atom-thick CeO₂ sheets with a pit size of 0.90 nm × 0.82 nm; the CO molecules prefer to adsorb at P₂ site, while the O₂ molecules tend to adsorb and dissociate at the adjacent P₁ sites. (d) Catalytic activity for CO oxidation versus reaction temperatures (experimental error: ±3%) and (e) the corresponding Arrhenius plot for the three CeO₂ samples (experimental error: ±3%). Adapted with permission from Ref. [85]. Copyright © 2013, Rights Managed by Nature Publishing Group.

adsorption at the five-coordinated pits surrounding Ce species (Fig. 15c). Such configuration of the catalytic centers can avoid the catalyst poison and promote the catalytic activity for CO oxidation (Fig. 15d–f). DFT calculations also showed that the dissociation of O₂ is the rate-determining step in CO oxidation. The lowest energy barrier for the activation of O₂ is occurred at the two adjacent five-coordinated pits surrounding Ce species (Fig. 15d). Subsequently, the surface-activated oxygen species at the five-coordinated Ce sites can diffuse to the four-coordinated Ce sites and then oxidize the adsorbed CO. Desorption of the generated CO₂ is found to recover the catalytic active phase for the oxidation of next CO molecules. In addition, the highly coordination-unsaturated pits surrounding Ce sites would lead to the increase in the hole carrier density and hence assured the rapid CO diffusion along the 2D conducting channel of the surface pits. Importantly, these pit-rich CeO₂ nanosheets delivered a much higher catalytic activity for CO oxidation with a low activation energy of only 61.7 kJ/mol, being much smaller than those of bulk CeO₂ and pit-free CeO₂ nanosheets (Fig. 15h–i).

Besides the recently developed synthetic methods for the optimization of surface properties of CeO₂ [111,112], post-synthesis treatments can also modulate their surface properties in order to promote CO oxidation. Cheung et al. reported the enhanced catalytic activity of nanostructured CeO₂ with various morphologies for CO oxidation by using the defect engineering under a low-pressure thermal activation process [88]. Chemical redox etching would induce the morphological evolution of CeO₂ nanorods from a smooth to a rough surfaced configuration accompanied with the increased specific surface areas, larger surface Ce³⁺ fraction, and higher concentration of oxygen vacancies, thus resulting in the significantly enhanced CO oxidation activity [92]. Therefore, the controlling the surface properties of CeO₂ is demonstrated with great potentials to tailor their fine structures, to construct the rationally designed catalytic active sites, and to promote their catalytic activity for CO oxidation.

5.2. CO₂ conversion

At the same time, physical/chemical capture and catalytically converting CO₂ into other chemicals, including useful hydrocarbon fuels and polymers, represent the practical and promising approaches to reduce CO₂ emission as well as to realize its reutilization [113–118]. However, the use of CO₂ as the C1 building block still faces many fundamental and technological challenges because of its chemically inert nature and very high bond energy. In this case, many homogeneous and heterogeneous catalysts have been designed to activate CO₂ at mild conditions. Particularly, CeO₂ catalysts with unique reversible chemical redox oxidation states between Ce³⁺ and Ce⁴⁺ can efficiently trap CO₂ molecules on top of

the surface basic sites, activate them, and promote the catalytic process in converting CO₂ into useful chemicals by various techniques, such as high-temperature gaseous phase reactions, liquid phase heterogeneous reactions, and photocatalysis. Generally, CeO₂ catalysts with the abundant surface defects can potentially enhance their catalytic performance for CO₂ conversion.

5.2.1. Catalytic synthesis of carbonates by CeO₂ catalysts

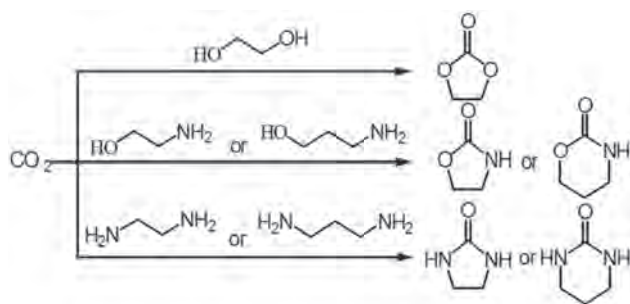
Because of the surface bifunctional acid-base properties of CeO₂, the efficient adsorption of amino groups, hydroxyl groups, and CO₂ would lead to the remarkable catalytic activity and selectivity in production of cyclic carbonates, cyclic carbamates, and cyclic ureas from diols, aminoalcohols, and diamines, respectively, with CO₂ as compared with other transitional metal oxides (ZrO₂, CaO, MgO, TiO₂, etc.) based catalysts [119]. The reaction mechanism catalyzed over CeO₂ is proposed in Scheme 1 [119]. Considering the formation of cyclic ureas as an example, four fundamental steps were involved, as demonstrated in Scheme 2: (1) the co-adsorption of one ethylenediamine molecule and two CO₂ molecules at the catalytic active site and the successive formation of the carbamate species on CeO₂ surfaces through the surface reaction between ethylenediamine and CO₂, (2) the transformation of the carbamate species into the surface-adsorbed amine with the release of one CO₂ molecule, (3) the nucleophilic addition of the amine group to the carbamate moiety on CeO₂ and the subsequent formation of the adsorbed 2-imidazolidinone, and (4) the desorption of 2-imidazolidinone and the regeneration of CeO₂ for further reaction. The third step is usually recognized as the rate-determining step.

For the synthesis of organic carbonates, especially dimethyl carbonate (DMC), from methanol and CO₂, the poor conversion efficiency (<10%) and the low chemoselectivity (60–90%) are generally observed even under high temperatures and pressures due to the thermodynamic limitation [120]. Various dehydrating agents are then added to remove the generated water, while a flow apparatus is generally used for the removal of the produced DMC to overcome the abovementioned problems.

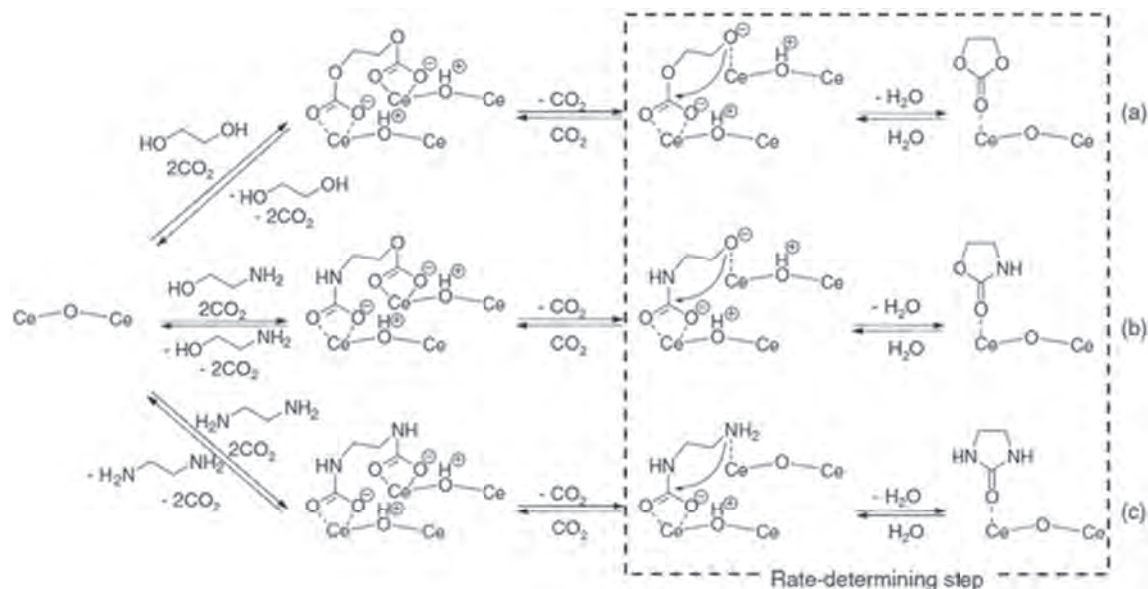
For instance, the catalytic activity of CeO₂ for the direct synthesis of DMC in the presence of dehydrating agents was systematically investigated by Tomishige's group [122–124]. A carboxylation/hydration cascade reaction was then realized to synthesize cyclic propylene carbonate, which was catalyzed by CeO₂ with 2-cyanopyridine (Scheme 3a). CeO₂, as a cascade catalyst, could not only catalytically convert diols into cyclic carbonates but also promoted the removal of water by the hydrolysis of nitrile into amide [121]. In specific, the catalytic mechanism was proposed as the following: (1) the adsorption of diol onto the CeO₂ surface through the interaction between hydroxyl group and Lewis acidic cerium sites, and the subsequent formation of the surface cerium alkoxide species; (2) the insertion of CO₂ into the Ce–O bond to form the surface alkyl carbonate species; (3) the nucleophilic attack of other hydroxyl groups on the carbonyl carbon in carbonate species to generate the products and water, and then consequently recover the surface active sites; and (4) the removal of water by dehydrating chemicals from CeO₂ surfaces (Scheme 3b) [97].

In addition, continuous flowing systems were also developed to further improve the conversion of methanol and the selective transformation of methanol into DMC. In this catalytic system, CeO₂ nanoparticles and 2-cyanopyridine were chosen as the catalyst and the recyclable dehydrating agent, respectively [125]. Controllable CO₂ feeding and stoichiometric amount of methanol and 2-cyanopyridine mixture under various pressures would lead to the high methanol conversion efficiency (>95%) and DMC selectivity (>99%) under the optimized reaction conditions (Fig. 16).

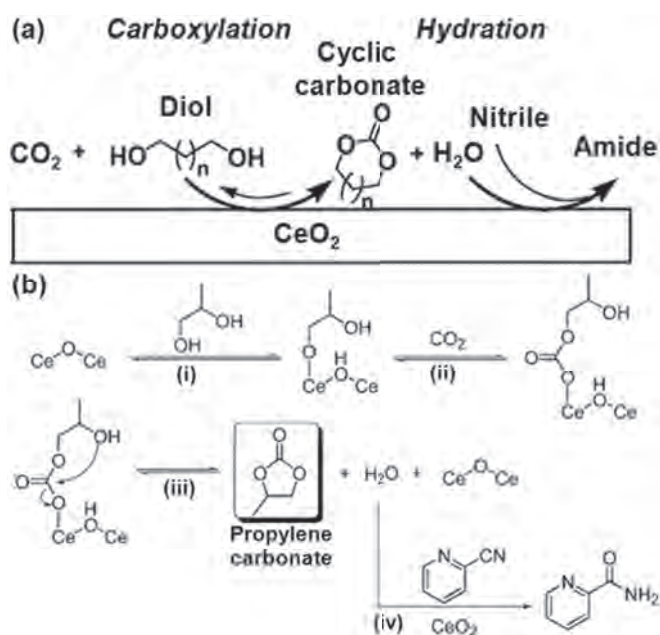
In any case, as efficient heterogeneous catalysts for the direct



Scheme 1. Transformation of CO₂ to cyclic carbonates, cyclic carbamates, and cyclic ureas from diols, aminoalcohols, and diamines, respectively. Adapted with permission from Ref. [119]. Copyright © 2014, WILEY-VCH Verlag GmbH & Co. KGaA, Weinheim.



Scheme 2. Reaction mechanisms for the synthesis of cyclic carbonate, cyclic carbamate, and cyclic urea over CeO_2 . Adapted with permission from Ref. [119]. Copyright © 2014, WILEY-VCH Verlag GmbH & Co. KGaA, Weinheim.



Scheme 3. (a) Carboxylation/hydration cascade catalyst of CeO_2 with nitrile and (b) proposed reaction mechanism. Adapted with permission from Ref. [121]. Copyright © 2014, American Chemical Society.

alcohol conversion with CO_2 , the catalytic structure-function relationship has been dedicated with efforts to illustrate the effects of surface properties of CeO_2 on both catalytic activity and selectivity. The yields of DMC were proportional to the specific surface area of catalysts. Stable crystal planes, such as CeO_2 (111), could provide the active catalytic sites [126]. The relationships between the DMC yields and the morphologies of CeO_2 catalysts are then revealed in Fig. 17, which established the consistent correlation among morphology, crystal planes, acid-base sites, and activity of CeO_2 . Also, spindle-like nanosized CeO_2 catalysts, with the large specific surface area, abundant exposed active (111) planes and substantial

amount of acid-base sites, would deliver the highest DMC yield, followed by nanorods, nanocubes, and nanooctahedra with the decreasing yield [127].

The efficient synthesis of DMC could also be achieved by the transesterification method from ethylene carbonate, which was catalyzed by mesoporous CeO_2 catalysts with the high surface area [128]. The surface basic hydroxyl ($\text{Ce}-\text{O}-\text{H}$) species were performed as catalytic active sites for the adsorption and subsequent activation of CH_3OH molecules in order to produce the highly active CH_3O^- intermediates. CeO_2 has as well been employed in synthesizing other organic carbonates, such as diethyl carbonate (DEC) from CO_2 and ethanol [102,103]. Typically, the amount of surface basic sites and the specific surface areas of CeO_2 were crucial for the adsorption of intermediates. Murzin et al. investigated systematically the effects of surface properties of CeO_2 catalysts synthesized by various methods on their catalytic performances. The DEC yield was observed to be positively related to the amounts of their surface basic sites and their specific surface areas of CeO_2 [129,130].

5.2.2. Reduction of CO_2

Another effective approach to recycle the heavily discharged CO_2 is to catalytically reduce CO_2 into hydrocarbon fuels (e.g. methane, methanol, and CO) through thermochemical and photocatalytic reactions. In terms of catalysts, as compared with other metal oxides, CeO_2 consists of the advantage of oxygen non-stoichiometry, high rates of oxygen chemical diffusivity, facile-regulated crystal planes and controllable band gaps, in which all these are demonstrated with potentials for the chemical reduction of CO_2 [131,132]. Moreover, surface control on CeO_2 , by creating more defects, can enhance the visible light absorption, obviously benefiting the corresponding photocatalysis. However, introducing too many defects might lower the photocatalytic efficiency due to the fact that these defects can also acted as the trapping centers of subsequently photogenerated charges. Thus, the optimized surface properties of CeO_2 are beneficial for the enhanced catalytic conversion of CO_2 .

Furthermore, the samarium-doped CeO_2 catalysts have also be demonstrated to thermochemically reduced CO_2 with water into hydrogen and CO at high temperatures (over 800°C) [133]. By using

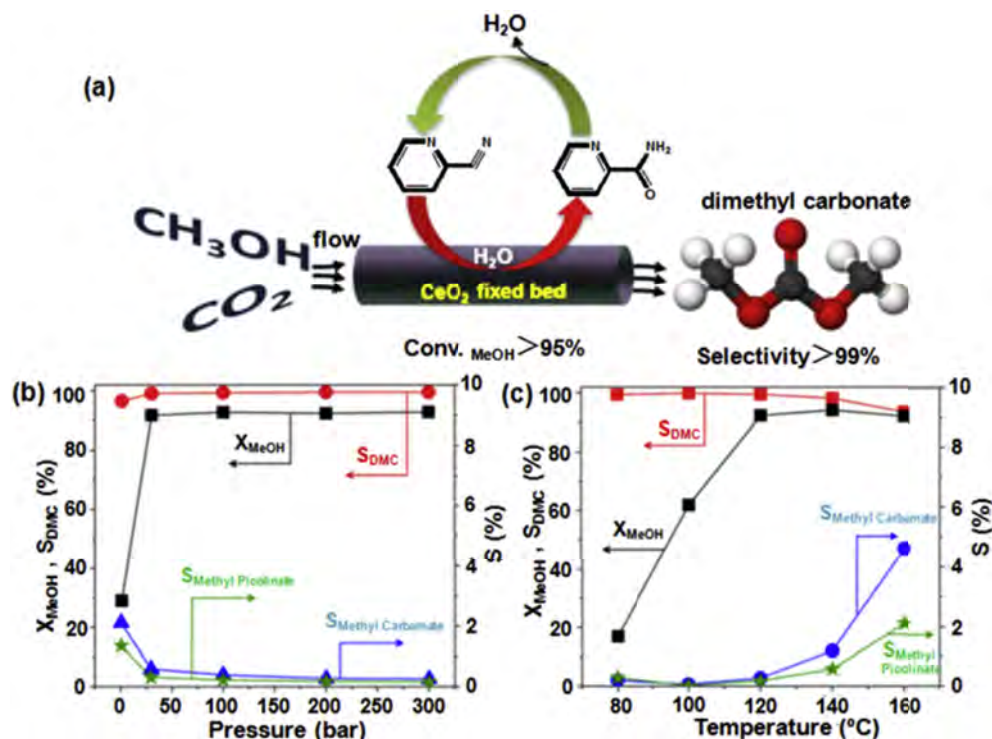


Fig. 16. (a) Scheme of DMC formation using CeO_2 fixed bed and dehydrating agent and effects of (b) pressure and (c) temperature on methanol conversion and product selectivity. Adapted with permission from Ref. [125]. Copyright © 2014, American Chemical Society.

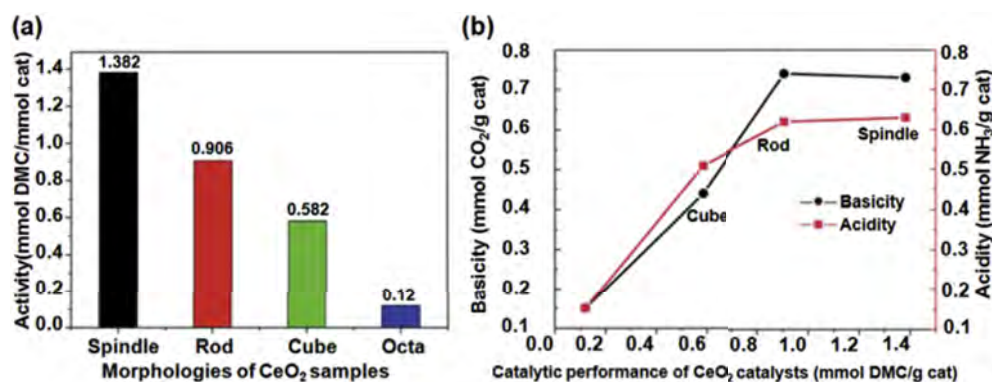
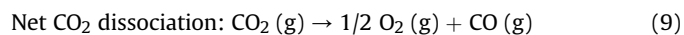
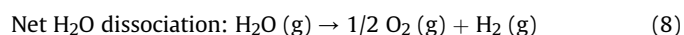
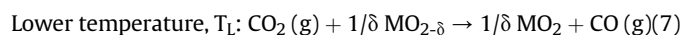
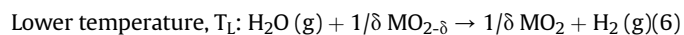
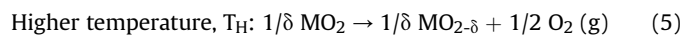


Fig. 17. (a) Catalytic performance of CeO_2 catalysts with different morphologies. (b) Correlation between acid-basicity and catalytic performance of CeO_2 catalysts with different morphologies. Adapted with permission from Ref. [126]. Copyright © 2006, Elsevier B. V. All rights preserved.

this approach, the rapid thermal conversion of CO_2 into useful fuel feedstocks of hydrogen, CO, syngas, or methane could be realized. However, the thermochemical reduction at high temperatures is unfavorable for practical applications because of the poor chemoselectivity, high energy consumption at the endothermic step, and thermal collapse of the catalysts. In this case, the solar-thermal reduction technique was hence considered as the more effective and practical methodology here. Later, a solar cavity-receiver reactor was designed to achieve the high-flux solar-driven thermochemical dissociation of CO_2 and H_2O with the utilization of nonstoichiometric CeO_2 catalysts [134]. As shown in Fig. 18, a solar reactor was constructed to include a cavity receiver with a windowed aperture in which the concentrated solar radiation could pass through. Porous CeO_2 was then functioned as a catalyst for promoting the dissociation of CO_2 and H_2O to generate syngas (H_2 and CO) and O_2 , simultaneously.

The thermochemical H_2O – CO_2 -splitting cycle over a non-stoichiometric oxide can be described by the following reactions (Equations (5)–(9)) [134]:



where M represents Ce or the combination of Ce and a dopant element. When the local temperature was over 900 $^\circ\text{C}$, CO_2

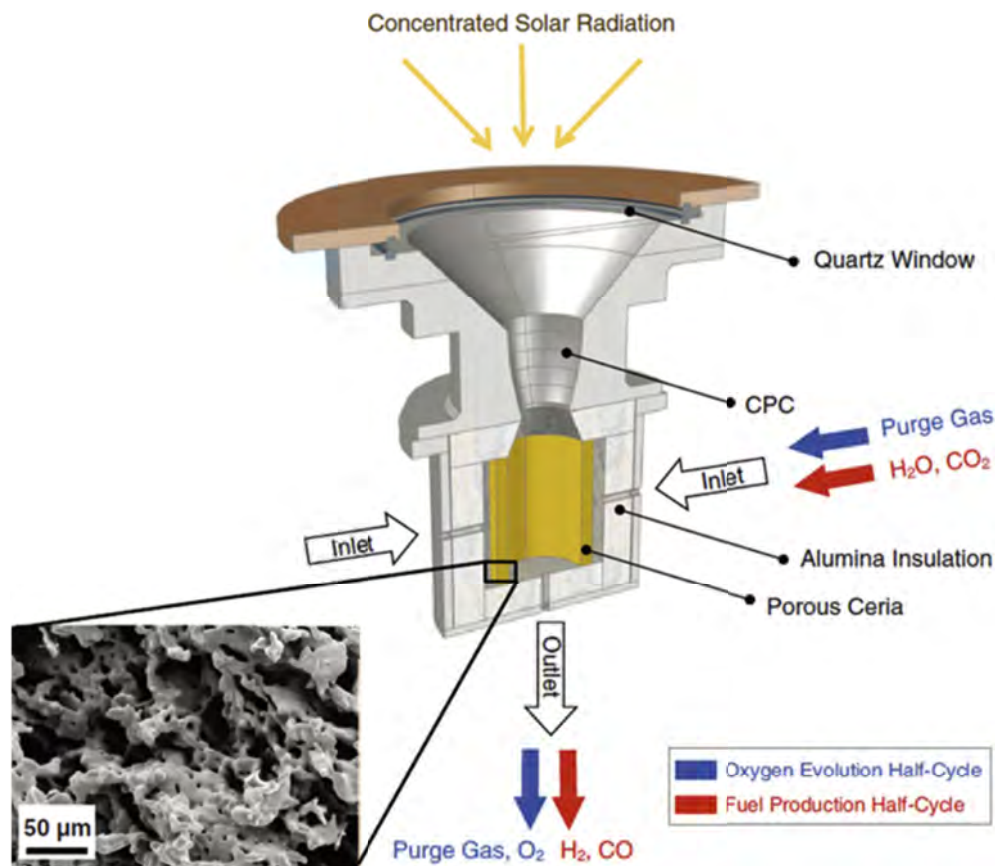


Fig. 18. Schematic of the solar reactor for the two-step, solar-driven thermochemical production of fuels. Concentrated solar radiation enters through a windowed aperture and impinges on the inner walls of ceria. Reacting gases flow radially across the porous ceria toward the cavity inside, whereas product gases exit the cavity through an axial outlet port at the bottom. Adapted with permission from Ref. [134]. Copyright © 2010 American Association for the Advancement of Science.

dissociation was initiated. Then, a selectivity of 100% towards CO production without any detectable amount of carbonaceous species was obtained. Also, the high catalytic stability of porous ceria catalysts could be maintained even after 500 thermochemical cycles such that these catalysts were suitable for practical applications. Typically, the capability of the solar-driven system with a fluidized bed reactor for CO₂/H₂O conversions was analyzed based on the second law of thermodynamics and the catalytic mechanism of CeO₂ [135]. With the assistance of CeO₂ catalysts and the recapture of waste heat, an increase in the temperature of the carrier gas and the concentration ratio of CO₂/H₂O would further promote the conversion efficiency of solar to chemical energy up to 43.2%.

In addition, the photocatalytic conversion of CO₂ into useful hydrocarbons under mild conditions is also a promising approach [136–142]. In order to suppress the energy barrier for producing CO, the formation of bent CO₂^{•−} intermediates on a semiconductor surface through the efficient activation of CO₂ is considered the most important step, followed by the reductive dissociation of the C–O bond. Similar to that in the synthesis of DMC, the catalytic surface properties, including oxygen vacancies and acidity-basicity of CeO₂, are of great importance in the CO₂ adsorption, diffusion, and electron-facilitated redox chemistry over the catalysts [137]. The defect-enriched CeO₂ nanorods showed the excellent capability of photochemical conversion of CO₂ to CO with a high selectivity under ambient conditions [137]. Experimental results also demonstrated that the elimination of surface oxygen vacancies and the enhanced electrophilic species would weaken the CO₂ activation, suppressing the migration of the energetic electrons and

terminating the photoreduction of CO₂ (Fig. 19). Thus, the surface oxygen vacancies and the defect-induced local strain accommodated in the defective nanorods were expected to facilitate the activation of CO₂, to lower the energy barrier, and to provide abundant catalytic sites for the reduction of CO₂. However, the high concentration of surface defects might inevitably reduce the diffusion of photogenerated charges because of the charge trapping nature of the surface defects.

The photocatalytic activity of CeO₂ for CO₂ reduction is also highly depended on the crystal orientation of the catalysts. For example, a CeO₂ homojunction, consisting of the hexahedron prism-anchored octahedra with the exposed prism surfaces of {100} facets and the exposed octahedral surfaces of {111} facets, could be constructed by the solution-based crystallographic-oriented epitaxial growth (Fig. 20a–d) [140]. Strong structure-activity relationships for the photocatalytic CO₂ conversion were then observed, where Pt was used as the cocatalyst (Fig. 20e–f). This homojunctioned structure were known to contribute to the following three crucial factors: (1) the efficient transfer of photogenerated electrons and holes to the octahedral and prism surfaces, respectively, where this efficient spatial charge separation could promote the separation and duration of photogenerated charges; (2) the CeO₂ hexahedron prism arms as the fast pathways for photogenerated carrier transportation within the homojunction; (3) the different effective mass of electrons and holes on {100} and {111} facets equipped with the higher charge carrier mobility and more facilitated charge separation [113]. As a result, by the rational design of CeO₂ arms, the optimized properties towards methane

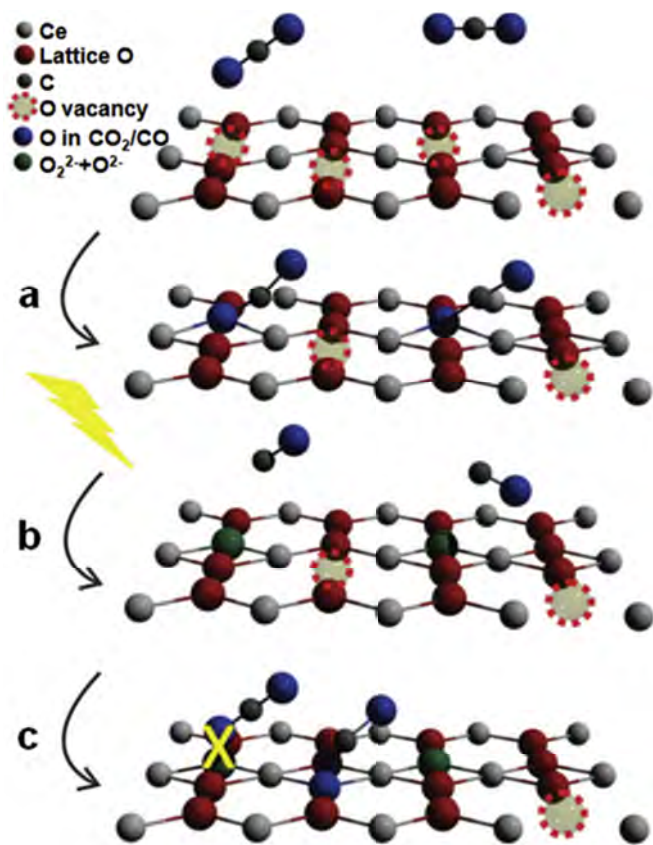


Fig. 19. Proposed representation of the oxygen vacancy and strain-mediated photochemical CO_2 reduction over rod-like ceria. Reduced ceria (110) is taken for example. Adapted with permission from Ref. [137]. Copyright © 2014, Royal Society of Chemistry.

generation could then be obtained (Fig. 20).

However, the corresponding light adsorption is only limited to the range of ultraviolet and blue region with the wavelength smaller than 360 nm due to the relatively large band gap of CeO_2 (~3.2 eV). In this case, CeO_2 is usually hindered from photocatalysis because of its inappropriate band gap, in which it can only be functioned as the co-catalyst/additive to promote the electron-hole separation and oxygen mobility due to its recyclable $\text{Ce}^{3+}/\text{Ce}^{4+}$ pair and OSC [5,90]. As discussed, increasing the surface defect concentration of CeO_2 by controlling the morphology, doping foreign ions, and different post-treatments can apparently narrow down its band gap to broaden the light adsorption as well as to generate more active sites for CO_2 adsorption. Future investigations on the control of surface properties of ceria can further enhance its catalytic activity towards photochemical reduction of CO_2 .

5.3. Organic transformation

As a multi-functional oxide materials, CeO_2 has attracted considerable attentions in the organic catalytic reactions, such as hydrolysis, dehydration, reduction, oxidation, addition, substitution, ring opening, and coupling reactions [6,143–145]. Both the surface-versatile acid-base features and the reversible redox properties of CeO_2 trigger its highly catalytic performances for numerous organic transformations. In general, the surface Ce^{3+} and oxygen vacancy have been reported as the active catalytic sites for hydrolysis and oxidation reactions [6]. The surface Lewis basic sites and oxygen vacancy can mediate the electron transfer and modulate the electronic density of the surface active centers, which can

further affect their catalytic capabilities for the reduction and coupling reactions. A wide range of organic reactions catalyzed by CeO_2 have been well summarized by Vivier et al. in 2010 and references therein [6]. Herein, we discuss the recent progress on the catalytic performance of CeO_2 for various organic reactions with the special emphasis on correlations between the surface properties and the catalytic performance.

5.3.1. Hydrolysis and dehydration reactions

Hydrolysis and dehydration reactions, which are of great importance for organic synthesis and industrial production, can be generally catalyzed by various homogeneous Lewis acid catalysts. It is well known that the controllability on the amount and strength of the surface Lewis acid/base is important for these two reactions. For heterogeneous Lewis acid catalysts, the Lewis acid sites will be easily malfunctioned by the chemical dissociation of water on the surface of heterogeneous catalysts during hydrolysis. This irreversible process would lead to the rapid decline of the catalysts' activity. Recent studies demonstrated that CeO_2 synthesized by a specific method was belonged to a type of catalyst that is water tolerant during hydrolysis [146]. In this work, CeO_2 catalysts showed the exceptionally high activity with a turnover number of up to 260 and a good recyclability for the hydrolysis of 4-methyl-1,3-dioxane to 1,3-butanediol (Fig. 21a and b). The general interaction between water and CeO_2 forms the proton- and hydroxide-covered surface of CeO_2 under hydrothermal conditions or at high temperatures. This irreversible process completely changes the surface acid-base properties of the catalysts. Importantly, the analysis of temperature-programmed desorption of water on the specific CeO_2 catalysts indicated that the water molecules were associatively adsorbed as weak protons and hydroxides on the catalyst surface (type 3 in the profile, Fig. 21c), in which this reversible process was confirmed by the FTIR and nuclear magnetic resonance (NMR) measurements on the acidity of freshly prepared catalysts and water-treated ones. As a result, the CeO_2 catalysts reported in this study are illustrated as water resistant.

The catalytic mechanism for hydrolysis by CeO_2 is also proposed in Fig. 21d. In specific, the associatively adsorbed water located on top of the Lewis acidic sites of CeO_2 catalysts can protonate 4-methyl-1,3-dioxane, leading to the formation of surface adsorbed acetal and leaving the active site for the associate adsorption of the second water molecule. The second water molecule is then activated at the surface Lewis acidic site of CeO_2 catalysts and subsequently hydrolyzes the surface acetal into 1,3-butanediol as the product. Simultaneously, the surface active phase, the Lewis acidic site, is available again for the next hydrolysis process. It is noted that the (111) surface of CeO_2 was confirmed to be the catalytically active crystalline facet for hydrolysis. The surface property-dependent catalytic activity of CeO_2 nanorods was also evaluated for the hydrolysis of 4-methyl-1,3-dioxane, in which the catalysts with the highest concentration of surface defects would yield the highest catalytic activity.

At the same time, hydration of nitriles to amides is another important hydrolysis reaction. In general, this transformation is catalyzed by strong acids or bases. However, these catalysts always induce the over-hydrolysis of amides into carboxylic acids and the formation of salts after the neutralization of catalysts [147]. Similarly, the metal-based homogeneous and heterogeneous catalysts also suffer from restricted reaction conditions, high cost, and difficulties in the separation of product from the reaction systems. In contrast, the surface-engineered CeO_2 could deliver a catalytically selective hydration of 2-cyanopyridine, thereby being capable to produce the corresponding amide at low temperatures (30–100 °C). The surface low-coordinated Ce species or oxygen vacancies of CeO_2 are recognized as the catalytic active phases for

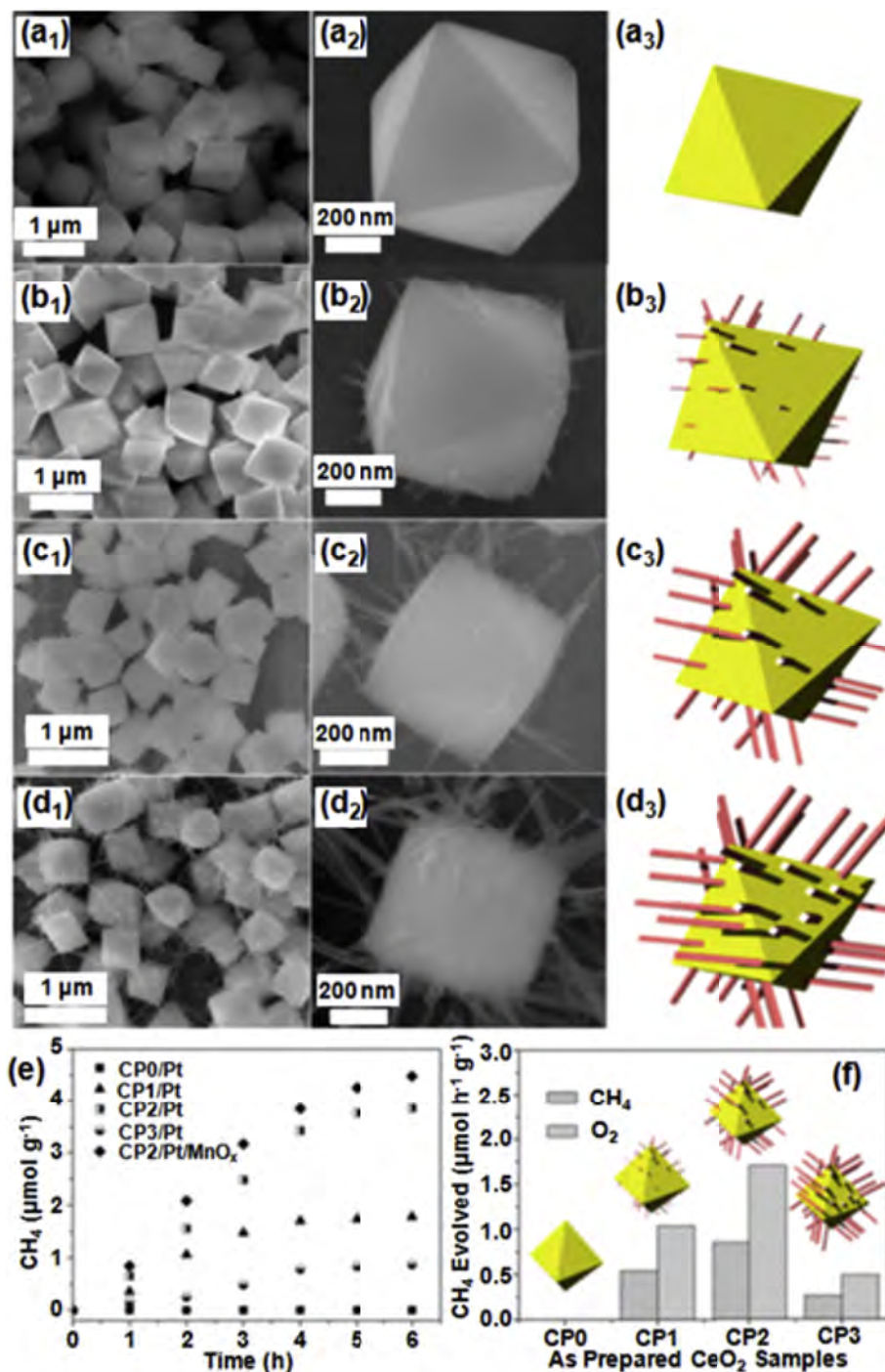


Fig. 20. (a–d) SEM images of homojunction structure of CeO₂ hexahedron prism-anchored octahedra with various hexahedron structures, (e) corresponding specific methane evolution activities, and (f) methane and oxygen evolution rates. Adapted with permission from Ref. [140]. Copyright © 2015, American Chemical Society.

the reaction [148]. As shown in the proposed catalytic mechanism (Fig. 22a), the hydrolysis reaction starts with the dissociation of water molecule on the surface oxygen vacancy sites of CeO₂ to produce H^{δ+} and OH^{δ-}. Nitrile is then adsorbed on the surface of CeO₂ through the weak interaction between N atom in the ring and surface Lewis acidic cerium sites, forming a nitrile-CeO₂ complex. Subsequently, the adsorbed complex undergoes an addition of OH^{δ-} to become a nitrile carbon atom, yielding the final amide. This step is typically considered as the rate-determining step. The final desorption of the products always accompanies with the

regeneration of the surface active sites. Based on the catalytic mechanism, one would expect that the post-treatment on CeO₂ catalysts creating more surface defects can further promote the corresponding catalytic activity for hydrolysis of nitriles. When nitriles have a heteroatom (N or O) adjacent to the α-C of CN group, the rate of hydrolysis reaction is considerably higher than that of other common nitriles (Fig. 22b) [149].

Notably, the nanocrystalline CeO₂ materials have also been found to function as the enhanced catalyst for the dehydration of aldoximes into nitriles as compared with other acid-base metal

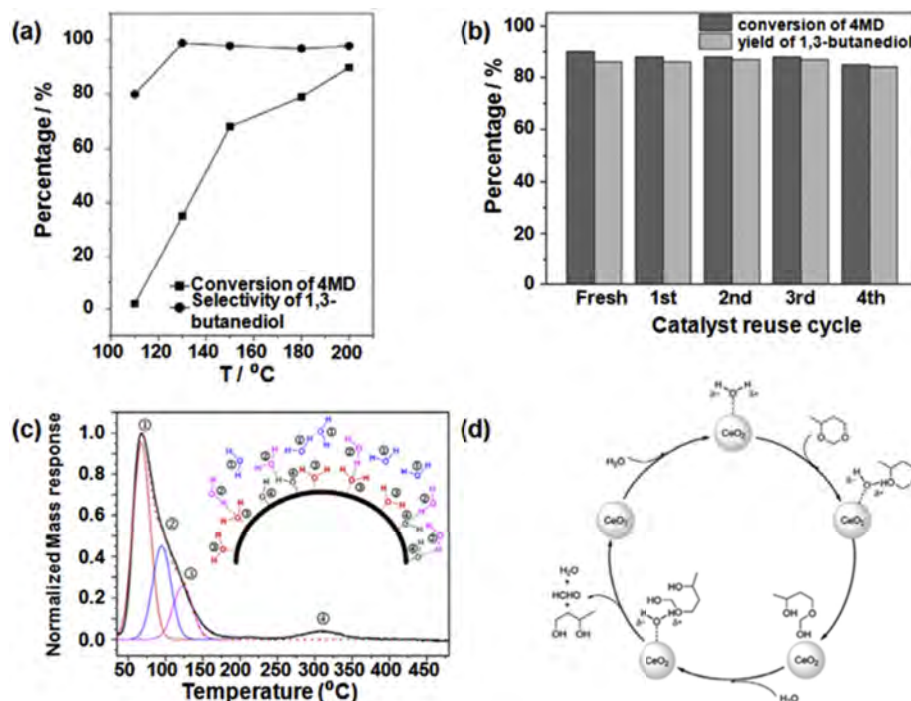


Fig. 21. (a, b) Catalytic performance of CeO₂ for the hydrolysis of 4-methyl-1,3-dioxane to 1,3-butanediol. (c) Profile of temperature-programmed desorption of water from ceria in flowing Ar gas (30 mL min⁻¹). The numbers in circles indicate different adsorbed water species on ceria. The inset shows structures of the four types of surface water. (d) Tentative reaction mechanism for the hydrolysis of 4-methyl-1,3-dioxane to 1,3-butanediol. Adapted with permission from Ref. [146]. Copyright © 2013, American Chemical Society.

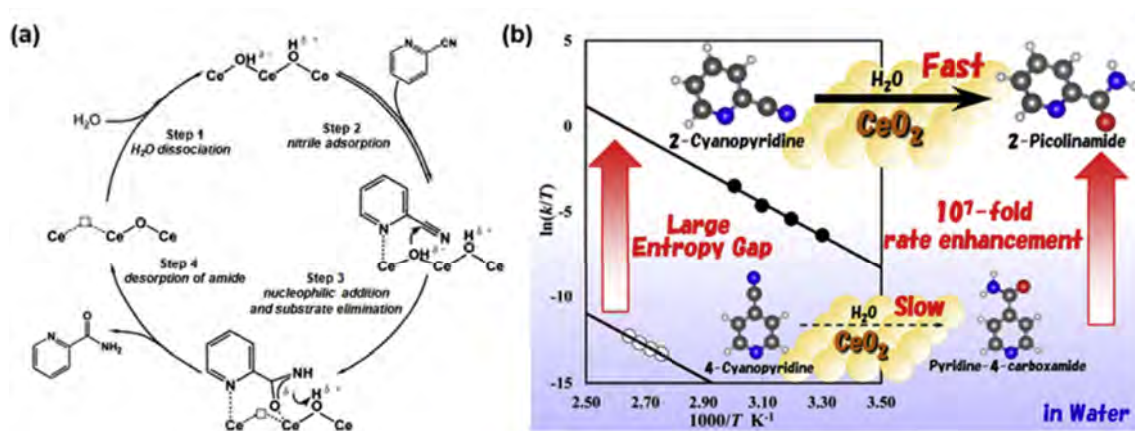


Fig. 22. (a) A proposed mechanism for nitrile hydration on CeO₂. Adapted with permission from Ref. [148]. Copyright © 2013, Royal Society of Chemistry. (b) Catalytic activity of CeO₂ for the hydration of different nitriles. Adapted with permission from Ref. [149]. Copyright © 2015, American Chemical Society.

oxides (e.g. Al₂O₃, TiO₂, and MgO) [150]. Many investigations of their catalytic mechanisms suggest that the Lewis acid sites are generally involved in the adsorption of oxime on the surface of CeO₂ through the interaction between N atoms and surface Lewis acidic sites. The surface Lewis base sites are responsible for catalyzing the C–H bond cleavage [150]. Combining these two results together, the surface acidic and basic sites can be employed for the dehydration of oximes. As discussed above, the nanocrystalline CeO₂ can also be utilized to catalyze the hydrolysis of nitriles. Thus, the picolinamide and picolinic acid alkyl ester derivatives can be obtained from 2-pyridinaldoxime with good yields in the one-pot process.

5.3.2. Oxidation reactions

For oxidation reactions, CeO₂ is as well commonly considered as one of the most promising catalysts because of its superior redox

ability and large OSC. In general, the redox ability of CeO₂ is important for the reaction performed at temperatures over 200 °C [151]. Until recently, numerous studies have proved that oxidations catalyzed by CeO₂ catalysts can be achieved at low temperatures (even less than 100 °C) by controlling their morphology, crystal facets, or chemical doping by foreign elements. For instance, CeO₂ alone is observed to exhibit the impressive catalytic activity to oxidize benzyl alcohol into benzaldehyde at 60 °C in presence of air as the oxidant, and the produced benzaldehyde can further couple with aniline to yield imine [152]. The catalytic activity of CeO₂ catalysts for oxidation can be additionally enhanced by loading Au nanocatalysts or Au nanoclusters onto their surface [153]. Au/CeO₂ are demonstrated to catalyze the aerobic oxidation of aromatic anilines to aromatic azo compounds under 100 °C. As compared with the pure CeO₂ catalyst, the catalytic activity of Au/CeO₂ enhances by almost 10 times under the same reaction conditions.

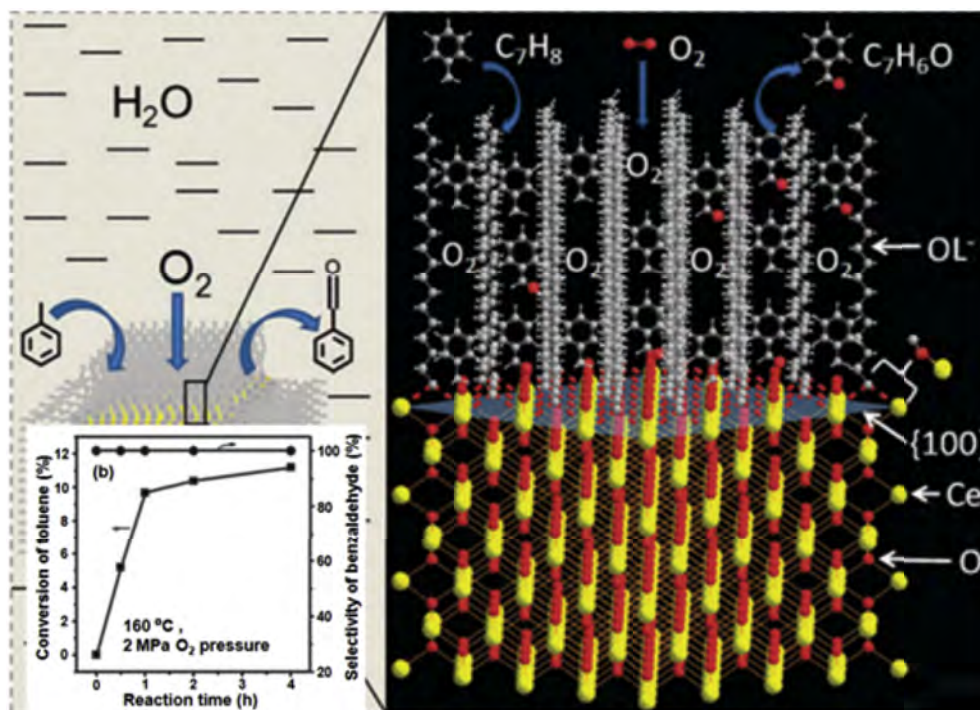


Fig. 23. Oxidation of toluene into benzaldehyde with well-defined CeO₂ nanocubes covered by oleic acid. Adapted with permission from Ref. [158]. Copyright © 2010, Royal Society of Chemistry.

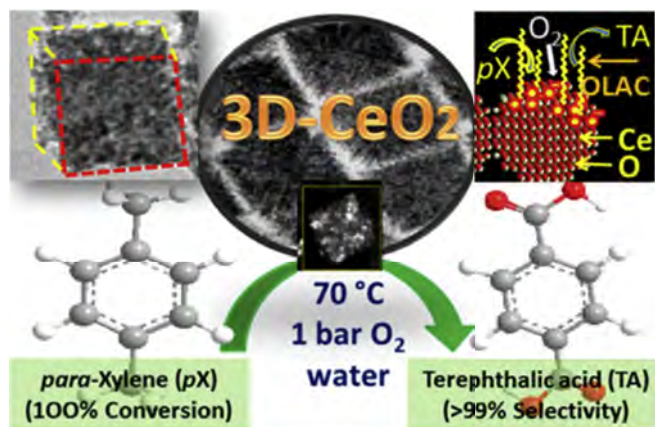


Fig. 24. Catalytic oxidation of *para*-xylene into terephthalic acid with 3D self-assembly of CeO₂ nanocubes. Adapted with permission from Ref. [159]. Copyright © 2014, American Chemical Society.

Regarding the selective oxidation of benzyl alcohol to benzaldehyde, visible-light-driven oxidations can be occurred even at room temperature catalyzed by Au/CeO₂ catalysts with various morphologies [154–156]. The Mn-doped CeO₂ catalysts with multiple redox states and very high OSC exhibit the superior catalytic performance for the selective oxidation of hydrocarbons under reaction temperatures between 100 and 120 °C [157]. The pronounced catalytic activity of MnCeO_x catalysts here can be attributed to the formation of Mn_{0.5}Ce_{0.5}O_x solid solution, which provides the maximum number of active surface oxygen species for the activation of C–H bonds.

After that, the oxidation of C–H bonds catalyzed by pure CeO₂ will be discussed thoroughly in the following. This reaction imposes a profound challenge for the development of efficient

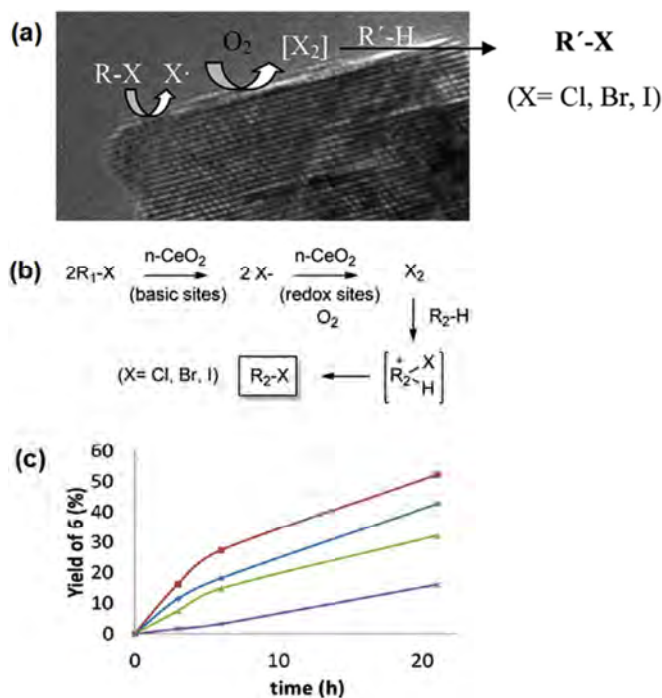


Fig. 25. (a) Oxyhalogenation of activated arenes with nanocrystalline ceria. (b) Possible mechanism for the nanocrystalline ceria-mediated aerobic oxidative halogenation of activated arenes with organic halides. (c) Time-yield plot for the halogenation of 1,3,5-trimethoxybenzene (0.62 mmol) in 1-bromo-3-chloropropane, under oxygen (6 bar, 0.9 mmol) at 140 °C in the presence of 1.2 mmol of ceria nanorods (□), standard nanocrystalline ceria (◇), nanooctahedra (Δ), or nanocubes (×). Adapted with permission from Ref. [160]. Copyright © 2013, American Chemical Society.

heterogeneous catalysts because of the large bond energy of C–H bonds involved. The well-defined CeO₂ nanocubes covered by oleic

acid are demonstrated with the exclusive selectivity for the oxidation of toluene into benzaldehyde [158]. The surface oleic acids do not only stabilize the {100} crystal facets but also favor the accessibility of organic reactants to the surface of CeO_2 nanocubes in the water media. Importantly, the highly regular surface of CeO_2 nanocubes is characterized as a smooth crystal plane with uniform surface states. Thus, the catalysts can produce only one type of active oxygen, which leads to the exclusively selective oxidation of toluene into benzaldehyde (Fig. 23) [158].

The 3D self-assembly of CeO_2 nanocubes can also be facilitated by a strong coordinating property of oleic acid towards (100) planes of the nanocrystals. The oriented attachment of CeO_2 nanocrystal

building blocks forms the (100) surfaces of the exposed porous CeO_2 cubic by sharing the {111} facets (Fig. 24). The assembled CeO_2 nanocubes then exhibited the superior oxidizability for the efficient alkylarene oxidation in water at low temperatures (below 85°C) and 1 bar O_2 pressure [159]. The features of high concentration of surface oxygen vacancies, small crystalline size of cubic building blocks, large surface area and pore size, and large quantity of hydrophobic oleic acid surfactants are believed to play important roles in the catalytic oxidation of alkylarenes. In this structure, the oxygen vacancy is the catalytically active site for the oxidation. As compared with CeO_2 (111), the (100) facets favor the formation of oxygen vacancy and deliver a large value of OSC. The long tail of

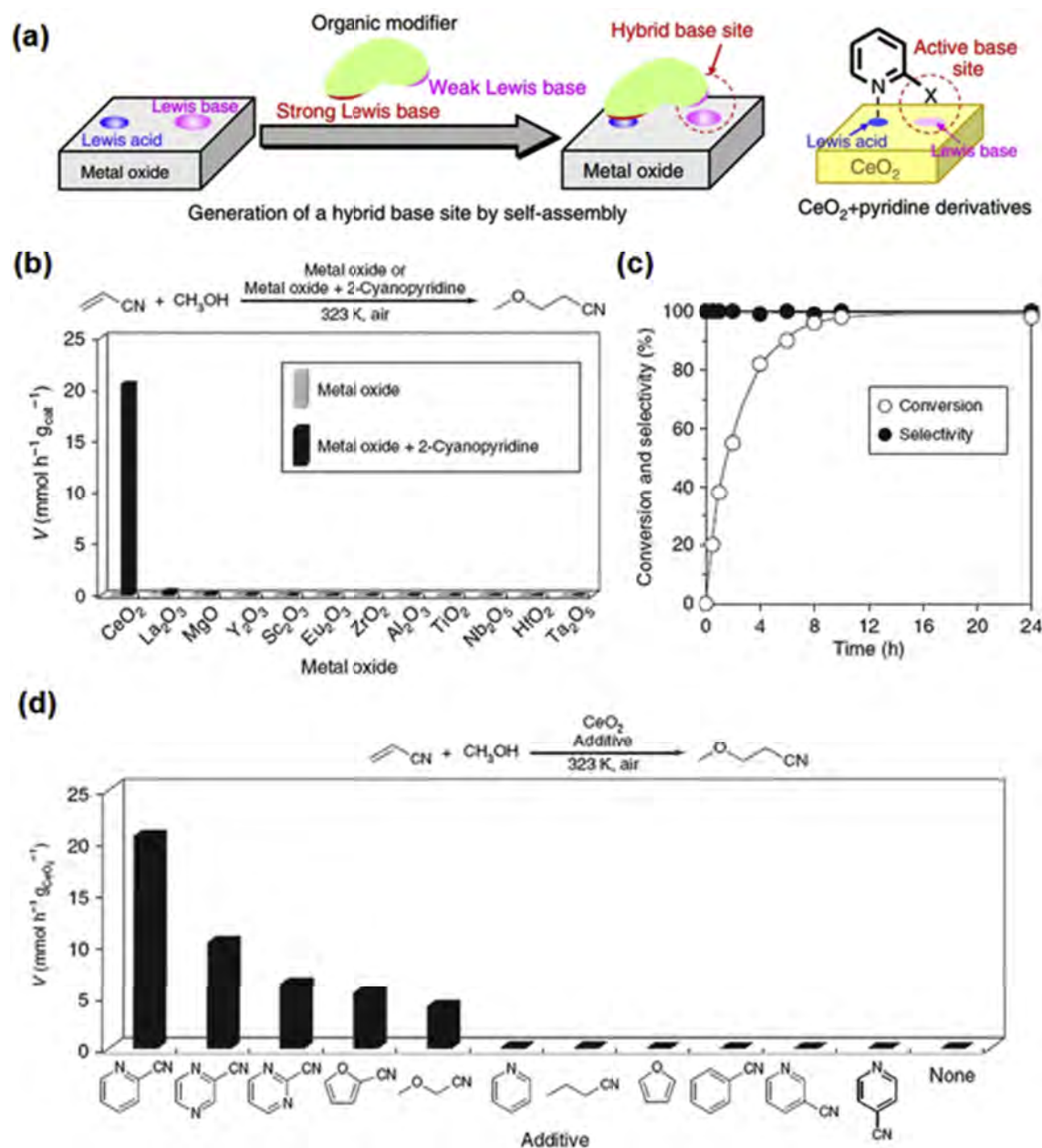


Fig. 26. Metal oxide and nitrile screening and the time course. (a) Comparison of the combination of metal oxide catalysts and 2-cyanopyridine. Reaction conditions without 2-cyanopyridine (gray bar): acrylonitrile (10 mmol), methanol (20 mmol), metal oxide (172 mg), 323 K, air, 12–48 h. Reaction conditions with 2-cyanopyridine (black bar): acrylonitrile (10 mmol), methanol (20 mmol), metal oxide (172 mg), 2-cyanopyridine (2 mmol), 323 K, air, 0.5–48 h. (b) Time course of the reaction over CeO_2 +2-cyanopyridine hybrid catalyst. Reaction conditions: acrylonitrile (10 mmol), methanol (15 mmol), CeO_2 (1 mmol), 2-cyanopyridine (1 mmol), 323 K, air. (c), Effect of organic compounds on the catalytic activity. Reaction conditions: acrylonitrile (10 mmol), methanol (20 mmol), CeO_2 (1 mmol), organic additive (2 mmol), 323 K, air. Adapted with permission from Ref. [161]. Copyright © 2015, Rights Managed by Nature Publishing Group.

hydrophobic oleic acid can also trap the alkylarenes into the pores and help them to reach the catalyst surface. The defective sites on the catalyst surface can as well promote the formation of intermediates, which further react with oxygen to release the products. After the removal of the surfactants, the catalysts are found to give the very poor catalytic activity and selectivity.

In any case, CeO_2 nanostructures are also revealed to deliver the remarkable catalytic activity for the oxidative oxyhalogenation of arenes under aerobic conditions [160]. Halogenation of hydrocarbons is an important process in the chemical industry. As illustrated in Fig. 25a, the C–H bond of the arenes can be activated effectively by CeO_2 catalysts and halogenated by the organic or inorganic halogen compounds in the presence of oxygen. The possible reaction mechanism is shown in Fig. 25b. Initially, the surface basic species of CeO_2 activates the halogen compounds to produce anionic halides, where the halogen radicals can be later generated at the surface redox sites of CeO_2 . When the two radicals interact with the dihalogen species, the products can be obtained by an electrophilic aromatic substitution. Notably, the formation of CeO_2 -halogen intermediates is also possible. Thus, regulating the surface properties of CeO_2 catalysts is also important for the enhancement of their catalytic activities. CeO_2 nanoparticles with the smaller crystalline size can as well give the higher catalytic activity, suggesting that the available surface areas and the abundance of surface defects contribute dominantly to the oxidative reactions. The plane orientations also play important roles for the catalytic oxidative halogenation of arenes. Among all the different morphologies, CeO_2 nanorods gave the best catalytic performance for oxidation reactions.

5.3.3. Hydromethoxylation of acrylonitrile

As compared with the unmodified catalysts, creating new catalytic active sites on the surface of heterogeneous catalysts by using small molecules as modifiers can improve their catalytic efficiency and chemoselectivity dramatically [161]. For example, there is a recent work employing pyridine and its derivatives as organic modifiers to construct a novel charge-transfer complex as the hybrid interface basic site on the surface of CeO_2 nanoparticles (Fig. 26a). In this strategy, the surface Lewis acidic sites of CeO_2 provide the adsorption sites for the organic modifiers. The defect-abundant surface of CeO_2 exhibits a structural feature with the adjacent surface Lewis acidic and basic sites. When the organic modifiers are existed in the presence of Lewis basic functional groups, the surface modification would produce a new Lewis base configuration composed of two bases, with one from the organic modifiers while another one from the surface adjacent Lewis bases. Once 2-cyanopyridine is used as the organic modifier, such a structure can deliver a 2000-fold enhancement for the hydromethoxylation of acrylonitrile with a very high selectivity as compared with CeO_2 alone (Fig. 26b). This impressive catalytic behavior is only observed on the complex of CeO_2 and pyridine modifiers, suggesting the importance of unique acid-base properties of CeO_2 for the formation of new surface catalytic active sites. Among various organic modifiers, 2-cyanopyridine is considered to be the most effective one (Fig. 26c).

5.3.4. Catalytic hydrogenation

In general, CeO_2 can serve as the promoter, stabilizer, or additive to improve the hydrogenation catalytic activity of anchored metal active phases (e.g. Pt, and Pd) [2]. The strong metal-support interaction effects between CeO_2 and metal active phases can enrich the electron density of supporting metals and subsequently promote their capability for hydrogen activation and dissociation [2,162,163]. Combining with the acid-base and redox properties of CeO_2 , the catalytic activity and selectivity of metal/ CeO_2 catalysts

for hydrogenation reactions can be dramatically modulated [162,164]. With CeO_2 as the support, Cu and Au catalysts also exhibit the strong ability for hydrogen activation and deliver the excellent catalytic activity for hydrogenation of unsaturated compounds [165,166]. In particular, Cu/ CeO_2 catalysts are revealed with the good activity towards the hydrogenation of DMCs to methanol at a temperature of 160 °C and a low H_2 pressure of 2.5 MPa [167]. Because of the large amount of surface defects, specific organic groups will be preferentially adsorbed on the surface of CeO_2 rather than the surface of metal nanocatalysts. This highly selective adsorption model of substrates may also dramatically promote the catalytic hydrogenation performance of CeO_2 -based catalysts. Recently, the subnano Pd clusters anchored on the surface defect-abundant PN-CeO_2 were shown to deliver the enhanced catalytic efficiency and chemoselectivity for the hydrogenation of nitroarenes [163]. For the hydrogenation of 4-nitrophenol, the catalyst yielded a TOF of $\sim 44059 \text{ h}^{-1}$ and a chemoselectivity to 4-aminophenol of >99.9%. This superior catalytic performance could be attributed to a cooperative effect between the highly dispersed subnano Pd clusters for the hydrogen activation and the unique surface sites of PN-CeO_2 with a high concentration of oxygen vacancy for the energetically and geometrically preferential adsorption of nitroarenes *via* the nitro group.

In fact, the catalytic activity of pure CeO_2 is commonly observed for oxidations rather than reductive hydrogenations. Previous DFT calculations indicated that CeO_2 (111) can effectively activate hydrogen molecules with a low activation energy of 0.2 eV and a high exothermicity (-2.82 eV) [168]. The adsorption energies of hydrogen species on CeO_2 (110) and CeO_2 (111) surfaces are calculated to be -150.8 and -128.3 kJ/mol , respectively. These simulation results indicated that the H_2 molecule can be effectively activated and energetically adsorbed on the CeO_2 surface. Early in 2007, it was reported that pure CeO_2 nanoparticles could hydrogenate benzoic acid into benzaldehyde at 380 °C in a fixed bed reactor [169]. Their rapid deactivated performance was attributed to the coke formation on the surface of CeO_2 nanoparticles; however, there is not any detailed catalytic mechanism explored for benzoic acid hydrogenations catalyzed by CeO_2 [169,170].

Lately, pure CeO_2 nanoparticles were discovered to exhibit their high catalytic activity and chemoselectivity in the partial hydrogenation of alkynes into olefins [171]. The hydrogenation of propyne at ambient pressure in the gas phase was used as a demonstration [141]. The hydrogenation conditions were optimized at 523 K with a $\text{H}_2/\text{C}_3\text{H}_4$ ratio of 30:1 and a contact time of 0.21 s. The conversion of propyne could reach a maximum of 96% with a selectivity to propene of 91%. An increase in the partial pressure of H_2 was positively related to both hydrogenation activity and chemoselectivity. However, either an increase or decrease in the reaction temperature would lead to a decreased catalytic activity. Also, the chemoselectivity of propene is generally decreased with the increasing reaction temperature. It is recognized that the mutative surface properties of CeO_2 catalysts under the operation conditions were critical to understand their hydrogenation performance. The propyne conversion was strongly dependent on the calcination temperature of catalysts (Fig. 27a), while the chemoselectivity to propene was moderately influenced by the calcination temperature. This catalytic phenomenon can be attributed to the decrease of the surface area of CeO_2 catalysts as a result of the increase in the calcination temperature. When the catalysts were pretreated with H_2/He , both the hydrogenation activity and selectivity decreased dramatically (Fig. 27b), which suggested that the surface reduction levels of CeO_2 catalysts were important to their catalytic performance.

At the same time, the corresponding catalytic mechanism can be proposed from the results of operando infrared spectroscopy. In the

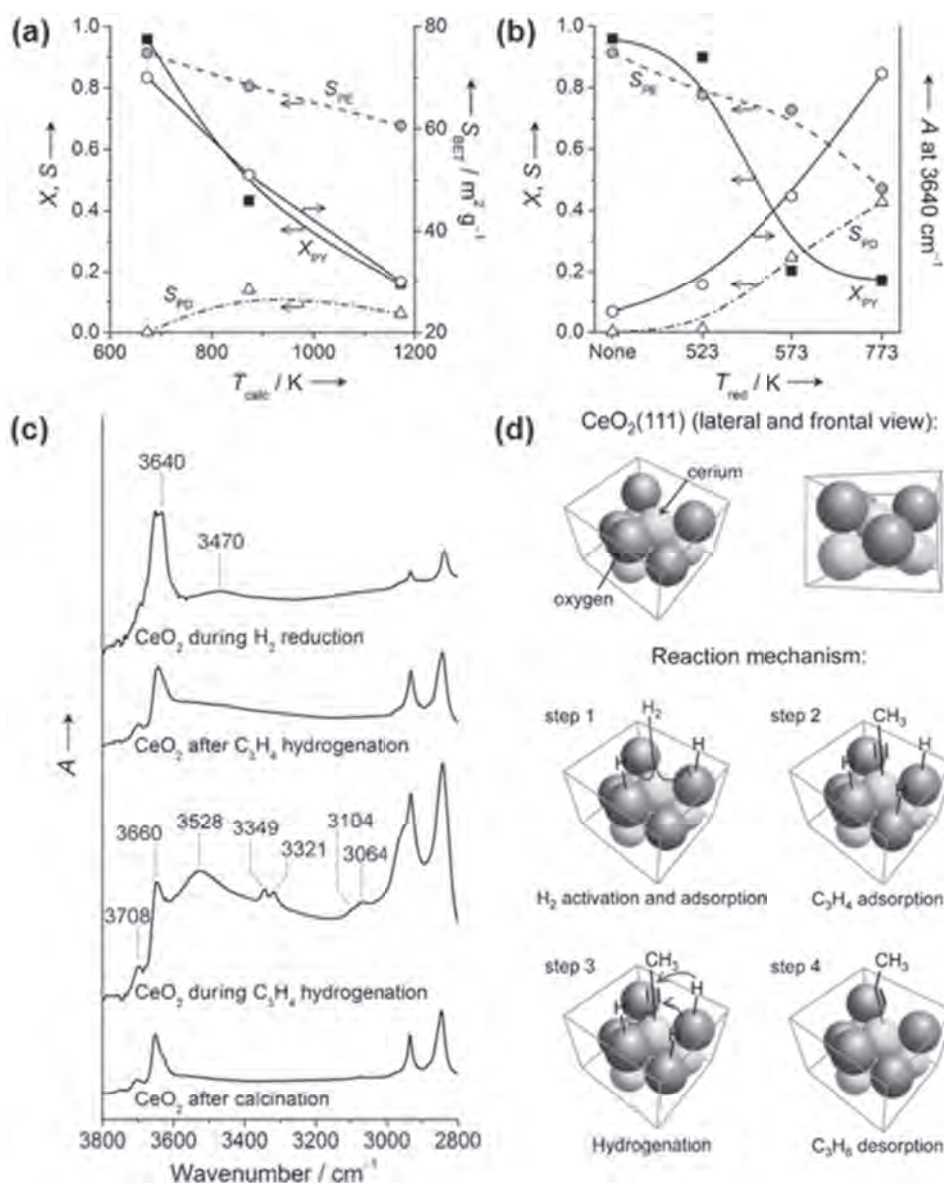


Fig. 27. (a) Conversion of propyne (XPY) and selectivity to propene (SPE) and propadiene (SPD) at 1 bar as a function of (a) the calcination temperature and (b) the reduction temperature of CeO_2 . Reaction conditions: $\text{H}_2/\text{C}_3\text{H}_4$ ratio of 30:1, $T = 523 \text{ K}$, and $t = 0.21 \text{ s}$. The influence of the calcination temperature on a specific surface area of the solid (S_{BET} ; determined by N_2 adsorption) and the reduction temperature on the extent of surface vacancies (determined by infrared spectroscopy; A = absorbance) are plotted in the secondary y axis of (a) and (b), respectively. (c) DRIFT spectra of CeO_2 recorded at 523 K, after calcination of propyne (in He flow), during hydrogenation of propyne ($\text{H}_2/\text{C}_3\text{H}_4$ ratio of 30:1 and $t = 0.21 \text{ s}$), after hydrogenation of propyne (in He flow), and during reduction of H_2 (in 5 vol % H_2/He ; A = absorbance). (d) Lateral and frontal views of the $\text{CeO}_2(111)$ facet depicting the proposed reaction mechanism. Adapted with permission from Ref. [171]. Copyright © 2012, WILEY-VCH Verlag GmbH & Co. KGaA, Weinheim.

first step, hydrogen molecules are activated on the surface oxygen of CeO_2 , whereas two surface OH groups are formed as a consequence (Fig. 27d). The strong surface acidic and basic sites of CeO_2 can then be employed to dissociate propyne into methylacetylide ($\text{CH}_3\text{—C}\equiv\text{C}$) on top of the cerium and another OH group. The evolution of diffuse reflection infrared Fourier transform (DRIFT) spectra provides evidence of the proposed activation process (Fig. 27c). The activated hydrogen species hydrogenates the methylacetylide into propene (step 3). Then, the desorption of propene recovers the surface properties of CeO_2 catalysts (step 4). As a result, the surface area and oxidation states of CeO_2 catalysts determine their catalytic activity and chemoselectivity for hydrogenation of alkynes into alkenes. The high reduction degree of CeO_2 catalysts would generate a high concentration of oxygen vacancy, which minimizes the available surface sites for the dissociation of

alkynes, leading to a decrease in the catalytic activity. The surface oxygen species are also crucial for the stabilization of activated hydrogen species for the next hydrogenation. In this case, CeO_2 catalysts with the exposed facets with low vacancy content can benefit the hydrogenation of alkynes into alkenes. The higher catalytic performance of CeO_2 is then typically dominated by the (111) surface, as compared to that of CeO_2 nanocubes enclosed with (100) facets [172].

However, the exact catalytic mechanism is still under debate till now. A recent DFT calculation study suggested a concerted pathway for the hydrogenation of alkynes (Fig. 28) [173]. The high ratio of $\text{H}_2/\text{C}_3\text{H}_4$ makes the CeO_2 surface completely hydroxylated. Both H_2 and C_3H_4 can be adsorbed on the top of Ce^{3+} . In this approach, the adsorbed H_2 molecule, the two carbon atoms from unabsorbed alkynes, and one OH group form a six-member ring structure as the

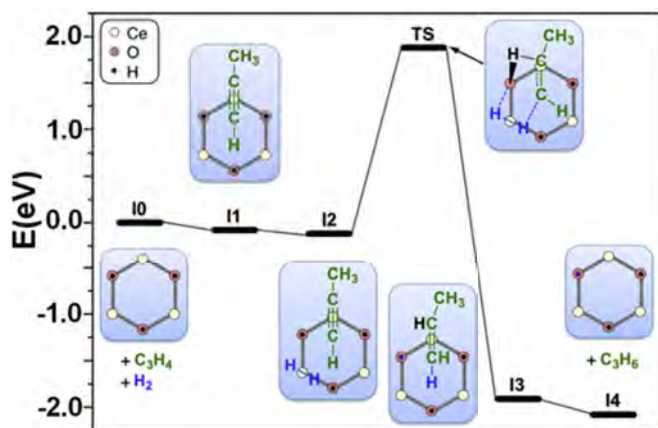


Fig. 28. Overall reaction energy profile for the selective hydrogenation of propyne. For the sake of clarity, the fully hydroxylated $\text{CeO}_2(111)$ surface is represented by a gray hexagon, where the Ce, O, and H surface atoms are depicted as pale yellow, red, and black spheres, respectively. The energy of TS has been corrected by the ZPVE. Adapted with permission from Ref. [173]. Copyright © 2014, American Chemical Society. (For interpretation of the references to color in this figure legend, the reader is referred to the Web version of this article.)

transition state. The calculated activation energy of 1.88 eV indicated that the proposed concerted pathway is plausible under the calculated conditions. It should also be noted that this hydrogenation mechanism is proposed on the basis of highly H-covered surface of CeO_2 catalysts.

In general, high temperature is required for the hydrogenation catalyzed by CeO_2 because of its inherent low capability of the heterolytic (between lattice Ce^{4+} and O^{2-}) pathway for H_2

dissociation. Moreover, the substrate selection is limited to alkynes with the terminal $\text{C}\equiv\text{C}$ triple bond because of the pre-requirements of the dissociation of $-\text{C}\equiv\text{C}-\text{H}$ at the catalyst surface. Recently, PN-CeO_2 catalysts with regulated surface properties have been reported to deliver a very high catalytic activity for the hydrogenation of alkenes and alkynes with the wider scope under mild conditions (Fig. 29a) [174]. As compared to others in the literature, three important factors were outlined: (1) PN-CeO_2 catalysts have a very high concentration of the surface defects, (2) both alkynes and alkenes can be reduced into alkanes, (3) the reaction conditions ($T = 100^\circ\text{C}$ and $P(\text{H}_2) = 1.0\text{ MPa}$) are much milder than those specified in the literature. Moreover, DFT calculations and control experiments suggest that the richness of surface defects is critical for the construction of a new surface Lewis acidic center by two adjacent reduced surface Ce atoms near the oxygen vacancy. The “fixed” surface lattice oxygen as Lewis base and the constructed Lewis acid have a large possibility to be close enough but independent due to the richness of surface defects as well as the unique geometrical and electronic configurations, being analogy to the molecular homogeneous FLPs. The theoretical results as well demonstrated that the created FLP sites can be easily used to dissociate H–H bond with a low activation energy of 0.17 eV (Fig. 29c).

The necessity of the co-existence of constructed Lewis acidic and basic sites of PN-CeO_2 for the hydrogenation of styrene was further confirmed in the presence of other molecular Lewis acid or base during the catalytic process. The addition of very small amount of Lewis base pyridine and Lewis acid pyrrole could completely terminate the hydrogenation activity of PN-CeO_2 (Fig. 29b). The blockage of surface sites of PN-CeO_2 by trace amount of pyridine/pyrrole molecules were found to give a low possibility

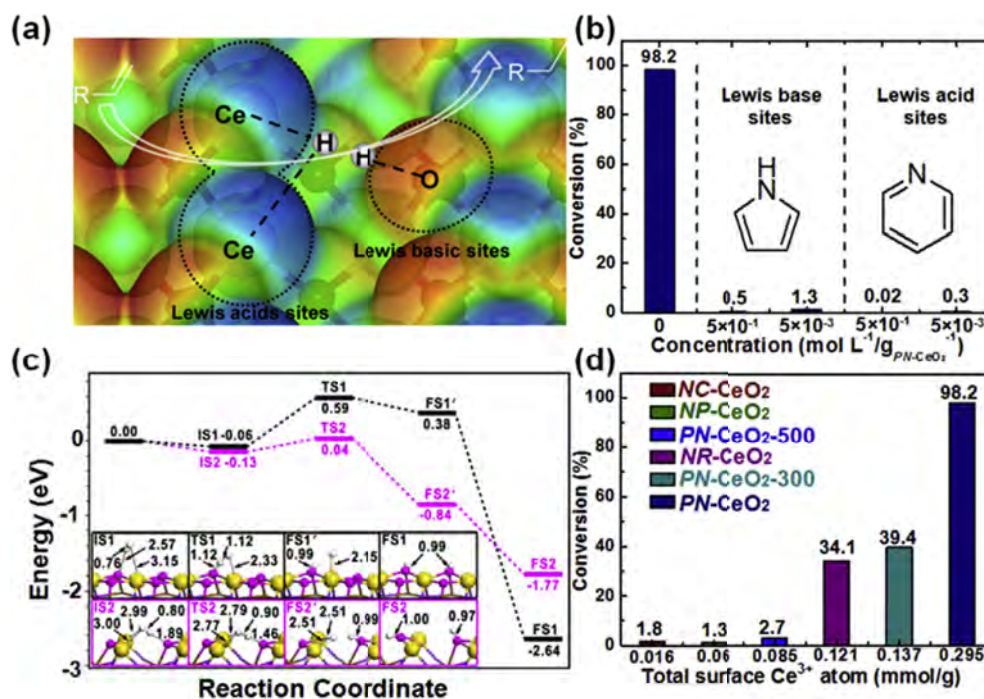


Fig. 29. (a) Schematic of created “FLP” catalytic sites on the surface of CeO_2 . (b) Energy profile for H_2 dissociation on ideal $\text{CeO}_2(110)$ shown by the black curve and on $\text{CeO}_2(110)$ with two oxygen vacancies shown by red curves. The optimized structures of initial states (IS), transition states (TS), and final states (FS) are labeled with bond distance (in Å). The zero energy reference corresponds to the sum energy of H_2 in the gas phase and the corresponding clean CeO_2 surfaces. (c) Effects of molecular Lewis base or Lewis acid on the catalytic activity of PN-CeO_2 for the hydrogenation of styrene. (d) Effects of the total number of surface Ce^{3+} atoms on the hydrogenation of styrene. NC- CeO_2 (Nanocube CeO_2), NP- CeO_2 (Nanoparticle CeO_2), PN- CeO_2 -500 (Porous CeO_2 nanorod calculation under air at 500°C for 10 h), NR- CeO_2 (Nanorod CeO_2), PN- CeO_2 -300 (Porous CeO_2 nanorod calculation under air at 300°C for 10 h), and PN- CeO_2 (Porous CeO_2 nanorods). Adapted with permission from Ref. [174]. Copyright © 2017, Rights Managed by Nature Publishing Group. (For interpretation of the references to color in this figure legend, the reader is referred to the Web version of this article.)

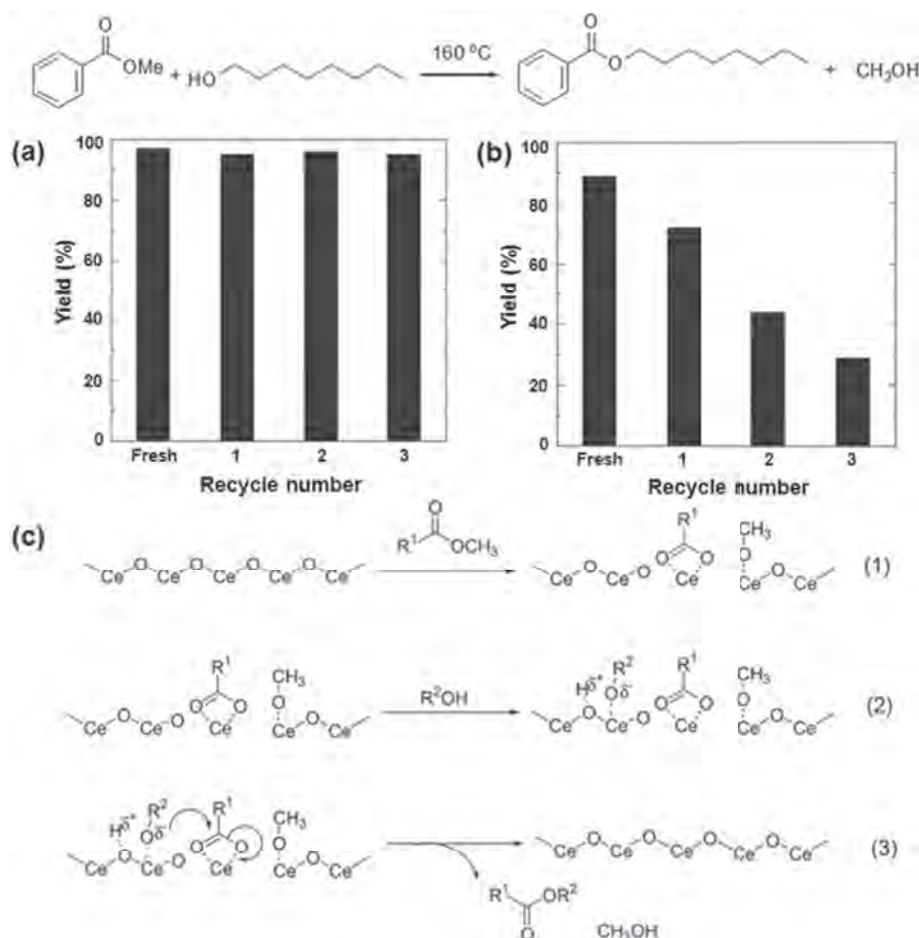


Fig. 30. Recycle tests of (a) CeO₂ and (b) CaO for the transesterification of methyl benzoate with n-octyl alcohol. (c) A proposed mechanism of transesterification by CeO₂ catalysts. Adapted with permission from Ref. [177]. Copyright © 2013, Royal Society of Chemistry.

for the formation of surface FLP sites in the aspect of population of adjacent surface Ce³⁺. Fig. 29d shows the conversion efficiency of styrene as a function of the total amount of the surface Ce³⁺ species per gram of various CeO₂ catalysts, which evidently demonstrates the importance of surface defects for the construction of surface FLP-like active sites and their consequent hydrogenation activity.

In addition, CeO₂ nanorods covered by {110} planes are also observed to efficiently and selectively catalyze the hydrogenation of nitroaromatics by using N₂H₄ as the reducing agent [175]. These {110} planes usually exhibit the higher catalytic activity for the hydrogenation as compared with the {100} and {111} counterparts. Theoretical studies showed that the surface reduction reaction on the {110} planes is energetically much more favorable because the oxygen vacancies are more easily formed on the {110} planes than on the {111} and {100} planes [175].

All the above hydrogenation performances of CeO₂ suggest that the surface properties of catalysts play very important roles in the reaction. Initially, the surface defects of CeO₂ are believed to be detrimental for the hydrogen activation [171,172]. Surprisingly, further increasing the surface defects of CeO₂ would lead to the formation of defect clusters and the construction of new surface active sites of the solid frustrated Lewis pairs, which can be used efficiently for the hydrogen activation and subsequent hydrogenation [174,176]. Such a strategy is of great interest to develop high-performance heterogeneous catalysts with the modulated active sites by regulating their surface properties.

5.3.5. Other catalytic organic reactions

Apart from conventional organic reactions, pure CeO₂ nanostructures have also been explored for many other organic catalysis. The transesterification of esters with alcohols is generally catalyzed by homogeneous protic acids, Lewis acids, and basic catalysts. Although heterogeneous catalysts (e.g., CaO, MgO, and polyoxometalates) have been reported for transesterification reactions, most of them are suffered from the catalyst leaching and narrow substrate scopes. Inspired from the co-existence of both surface acidic and basic species, CeO₂ was lately developed as the robust heterogeneous catalyst for the solvent-free transesterification of esters [177]. As compared with the catalytic performance of CaO, CeO₂ nanoparticles exhibited the higher catalytic efficiency with the good recyclability for transesterification of esters (Fig. 30a and b). Also, a catalytic mechanism of transesterification by CeO₂ is proposed in Fig. 30c. In the first step, the ester molecule is cleaved and adsorbed on the top of surface cerium sites, yielding the surface carboxylate species. Assisted by the surface basic sites of CeO₂, the dissociative adsorption of alcohol is also occurred at the catalyst surface to form the alkoxide species. The subsequent nucleophilic substitution between surface alkoxides and carboxylate species as well as the corresponding desorption would leave the products. It is noted that the proton abstraction of alcohol by a Lewis base site of CeO₂ is considered the rate-limiting step. Thus, the high concentration of surface basic sites will be expected to promote the catalytic performance of CeO₂.

Furthermore, CeO₂ nanoparticles also exhibited their catalytic

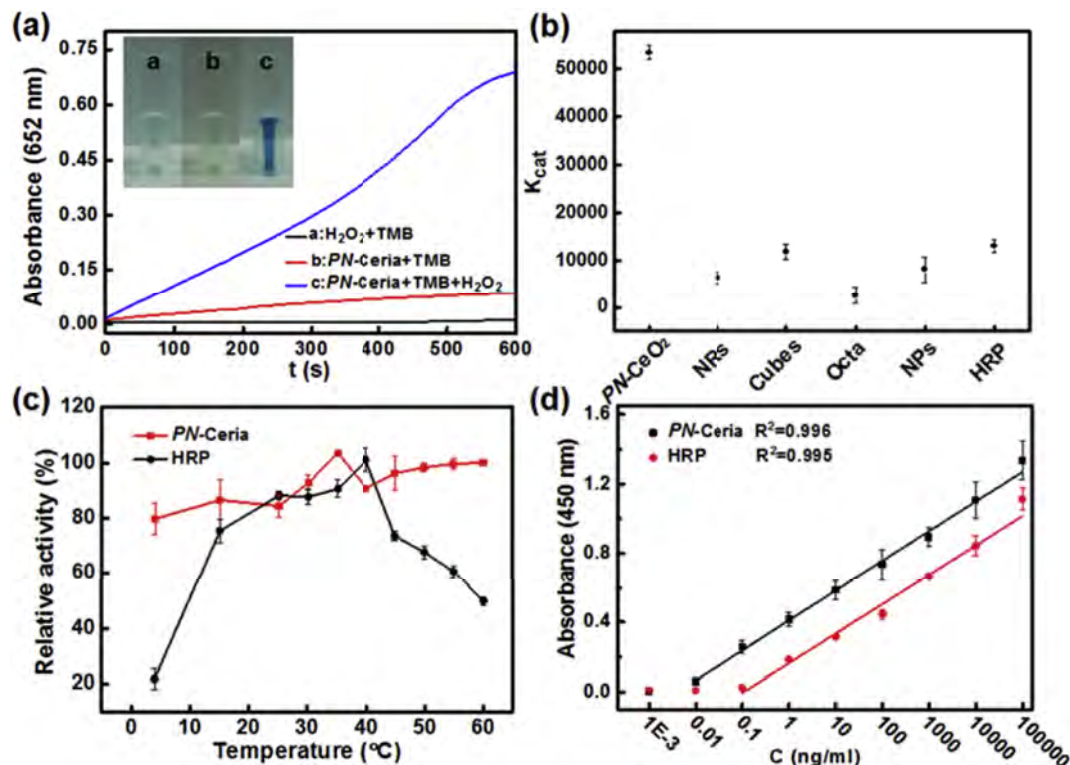


Fig. 31. Peroxidase A. Peroxidase-like activity of *PN-Ceria*. (a) Photograph of the mixture of TMB and H₂O₂ in the absence of *PN-Ceria*. (b) Photograph of the mixture of TMB and *PN-Ceria*. (c) Photograph of the mixture of TMB, H₂O₂, and *PN-Ceria*. Blue color was observed. B. Comparison of the K_{cat} for ceria nanomaterials and HRP. C. The temperature-dependent peroxidase-like activity of *PN-Ceria* and HRP. The pH and H₂O₂ concentration were 4.0 and 100 mM, respectively. The maximum point in each curve was set as 100%. D. Comparison of the detection limit of *PN-Ceria* and HRP system. Adapted with permission from Ref. [183]. Copyright © 2015, Elsevier B. V. All rights preserved. (For interpretation of the references to color in this figure legend, the reader is referred to the Web version of this article.)

activity for the one-step synthesis of esters from nitriles and alcohols [178]. The initial step of the catalytic reaction is similar to that of the selective hydrolysis of nitriles into amides. The surface amide-CeO₂ complex then undergoes an addition of alcohol to become the amide carbon atom to yield the ester. Likewise, the surface defects determine the catalytic activity. Thus, CeO₂ catalysts could deliver more than two orders of magnitude higher activity than other metal oxides (TiO₂, SnO₂, MnO₂, and ZrO₂, etc.), which was attributed to the unique surface acid-base and reversible redox properties of CeO₂. In another case, the Pr-doped CeO₂ catalysts showed the enhanced catalytic activity to convert isobutene, formaldehyde, and water into 3-methyl-1,3-butanediol in one step as contrasted to that enabled by pure CeO₂. This enhancement is largely due to the fact that the Pr doping can create more surface oxygen vacancies on the catalyst surface and subsequently improve the Lewis acidity of catalysts for the promoted catalytic activity [178].

5.4. Biomimetic catalysis

In addition, CeO₂ nanostructures have as well been extensively explored to mimic various natural enzymes, such as superoxide dismutase (SOD), peroxidase, catalase, and oxidase [179–184]. The multiple enzyme-like properties of CeO₂ can contribute diverse applications for clinic diagnosis, biosensing, drug delivery, and antioxidants against oxidative stress [185–198]. The use of CeO₂ nanostructures as artificial nanozymes has been originated from their surface reversible mutation of the oxidation states between Ce³⁺ and Ce⁴⁺ [179,181,182,199] as well as their features of biocompatibility and nontoxic nature [200,201]. Therefore, the

surface defects of CeO₂ typically serve as the catalytic active sites. Regulating their surface by chemical techniques can considerably affect the catalytic performances of CeO₂ nanostructures as artificial enzymes [179]. Comprehensive reviews on the artificial nanozymes, including CeO₂, have been performed. In this work, we aim to focus on the recent progress of biomimetic catalytic behavior of nanoceria, especially on those through the surface control.

5.4.1. Peroxidase-like activity of CeO₂

Peroxidases are a class of natural enzymes that catalyze the oxidation of compounds by the decomposition of hydrogen peroxide or organic peroxide [202]. Despite that CeO₂ nanostructures are widely explored as artificial SODs, oxidases, and catalases as well as for potential applications in biology [184,203,204], their peroxidase activity are seldom investigated because of their relatively low peroxidase activity [205]. Previous catalytic mechanism studies suggested that the surface properties of CeO₂ with a large surface Ce³⁺ fraction would play an important role to boost the peroxidase activity since the peroxidase-like activity of CeO₂ is originated from their ability of Ce³⁺/Ce⁴⁺ rapid cycling [182,183]. In this case, the highest available amount of Ce³⁺ on the surface of CeO₂ may promote the reaction efficiency and catalytic activity.

Recently, we reported that *PN-CeO₂* displayed a very strong peroxidase-like activity by catalyzing the oxidation of 3,3',5,5'-tetramethylbenzidine (TMB) in the presence of H₂O₂ (Fig. 31a), which demonstrated the importance of surface properties of CeO₂ as artificial nanozymes on their catalytic performance [183]. As compared with the natural horseradish peroxidase (HRP) and other nanoceria with various morphologies (e.g. nanoparticles,

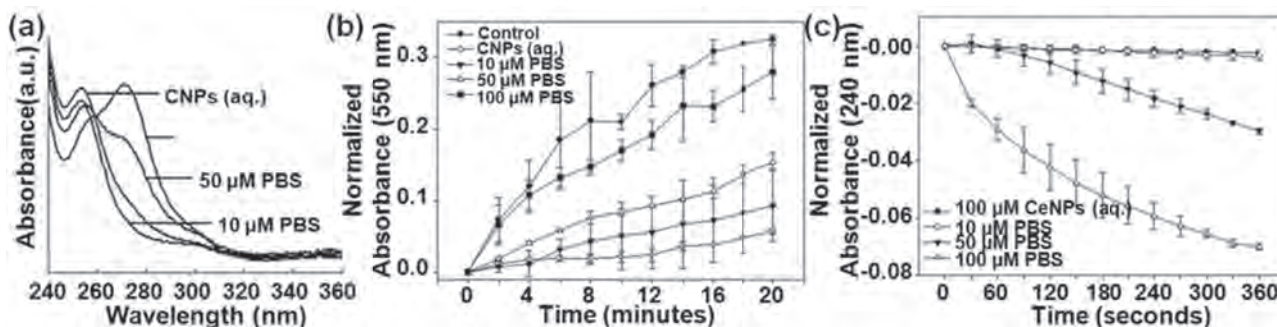


Fig. 32. SOD and catalase dose-dependent shift in surface oxidation state of CeNPs by treatment with phosphate anions (PO_4). CeNPs (100 mM) were dispersed in a range of phosphate concentrations (10, 50, and 100 mM) and incubated for 24 h before UV–visible spectroscopy (a), SOD mimetic (b) and catalase mimetic (c) activity measurements from the resulting suspensions. A kinetic measurement of catalase-like activity was analyzed by following H_2O_2 degradation at 240 nm. Adapted with permission from Ref. [207]. Copyright © 2011, Elsevier B. V. All rights preserved.

nonporous nanorods, cubes and octahedra), apparent steady-state kinetic studies indicate the best affinity of TMB with PN-CeO_2 and the highest catalytic activity of PN-CeO_2 as the peroxidase (Fig. 31b). Kinetic studies also suggest that the defective sites can serve as catalytic centers with the enhanced ability for activation of H_2O_2 . Thus, PN-CeO_2 with the highest surface Ce^{3+} fraction and the largest oxygen vacancy could deliver the superior peroxidase-like activity. This also explains the very low catalytic activity of commonly reported CeO_2 nanoparticles. Another unique aspect of PN-CeO_2 as the artificial peroxidase is its almost constant activity at various measurement temperatures of 4–60 °C (Fig. 31c). In addition, PN-CeO_2 as the artificial peroxidase shows a very high chemical and catalytic stability under harsh conditions. Later, an accurate and reliable immunoassay based on PN-CeO_2 was also

demonstrated for the specific detection of CA15-3 (a biomarker of breast cancer, Fig. 31d). The detection limit of PN-CeO_2 was 0.01 ng/mL, which was one order of magnitude higher than that of the HRP system.

5.4.2. SOD and catalase activity

SOD is a natural enzyme that catalyzes the dismutation of superoxide radicals into either O_2 or H_2O_2 . Catalase is a common enzyme that catalyzes the decomposition of H_2O_2 to H_2O and O_2 . Thus, both enzymes have protective effects against the oxidative stress induced by strong oxidants and exhibit the potential to protect the living organisms from the oxidative stress [186–188]. When CeO_2 mimics the SOD enzymes, the produced H_2O_2 , as the source of hydroxyl radicals (i.e. the most deconstructive ROS), is

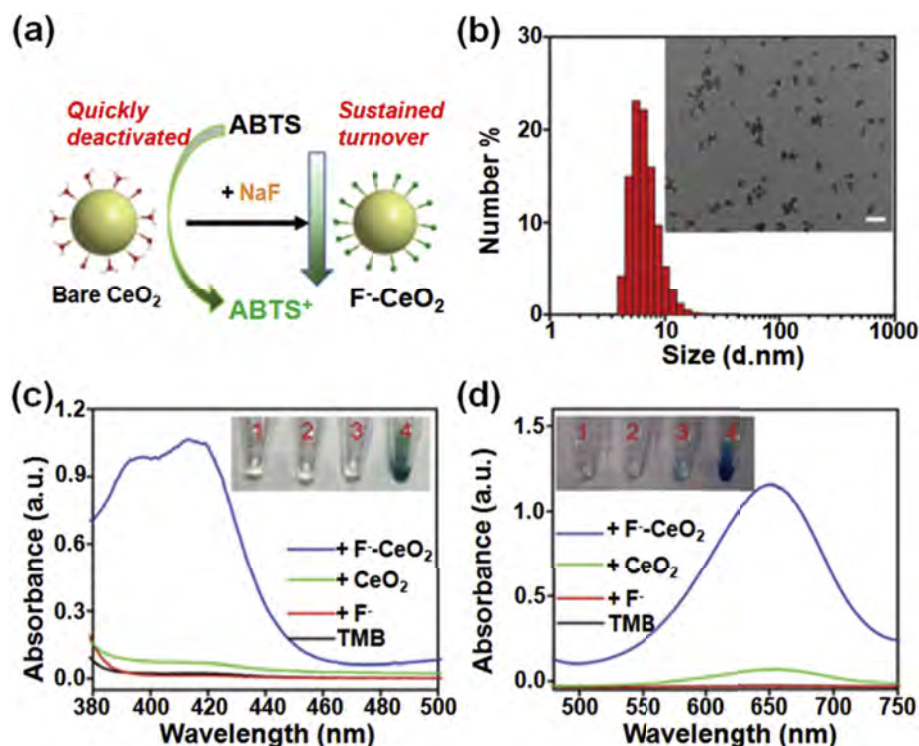


Fig. 33. Oxidase mimicking activity of nanoceria by fluoride capping. (a) A scheme showing F^- -capped nanoceria with improved oxidase turnovers. (b) DLS size distribution and a TEM image (inset) of nanoceria. The scale bar in the inset of (b) is 20 nm. UV–vis spectra of (c) ABTS (0.5 mM) and (d) TMB (1 mM) oxidation by nanoceria (100 $\mu\text{g mL}^{-1}$) with or without F^- (1 mM for ABTS, 5 mM for TMB) at pH 4 (acetate buffer, 20 mM) after 30 min of reaction. The insets are 1: the free substrate, 2: the substrate with F^- , 3: the substrate with bare CeO_2 , 4: the substrate with F^- -capped CeO_2 . Adapted with permission from Ref. [211]. Copyright © 2016, Royal Society of Chemistry.

considered as the more toxic species over superoxide for biological systems [179,187,206]. Fortunately, CeO_2 artificial nanozymes can also serve as catalases and decompose H_2O_2 into harmless O_2 and H_2O . As a result, CeO_2 nanozymes are promising to be used as antioxidants for the therapy involving oxidative stress. Many factors, including the morphology, size, surface $\text{Ce}^{3+}/\text{Ce}^{4+}$ ratio, and reaction conditions (e.g., pH, buffer species), affect the SOD and catalase activity of CeO_2 [181,182]. It has been recognized that the high surface $\text{Ce}^{3+}/\text{Ce}^{4+}$ ratio of CeO_2 nanozymes is a positive factor for their SOD-like activity but deconstructive for their catalase-like activity [182]. Thus, it is important to control the surface properties of CeO_2 to combine the SOD and catalase mimetic processes together, where the generated H_2O_2 from SOD mimetic system can be immediately consumed by the catalase mimetic system.

At the same time, inorganic ions, such as phosphate ions (PO_4^{3-}), have been recently found to effectively modulate the SOD and catalase activity of CeO_2 nanoparticles [207]. The phosphate ions are strongly adsorbed on the surface of cerium as a hard Lewis acid. When the concentration of phosphate ions is increased in the reaction environment, the SOD-like activity of CeO_2 is gradually inhibited but the catalase-like activity is enhanced (Fig. 32). Thus, it provides a practical approach to reach the equilibrium between H_2O_2 generation from the SOD process and subsequent H_2O_2

decomposition from catalase process.

5.4.3. Oxidase activity

Oxidase is an enzyme that catalyzes the oxidation-reduction reaction involving O_2 as the electron acceptor, in which O_2 is reduced to H_2O or H_2O_2 . In general, the oxidase-like activity of CeO_2 nanozymes has been evaluated and then further developed to use as colorimetric sensors for the selective detection of dopamine and catechol [208–210]. Similarly, the oxidase mimetic activity of CeO_2 is also considerably affected by the surface properties of artificial enzymes. Fluoride-treated CeO_2 nanoparticles showed over a 100-fold enhancement on their oxidase-like activity, as compared with the untreated counterparts (Fig. 33) [211]. This vast enhanced catalytic activity can be attributed to the alternated surface charge after the fluoride modification, in which the strong electron withdrawing properties of fluoride ions can promote the efficient adsorption of the substrates and desorption of the products.

5.4.4. Phosphatase-mimetic activity

In addition, phosphatase is an enzyme that hydrolyzes the phosphoric acid monoester into a phosphate ion and a free hydroxyl group [212]. Actually, phosphatase enzymes are essential to many biological functions, especially in the cellular regulation and

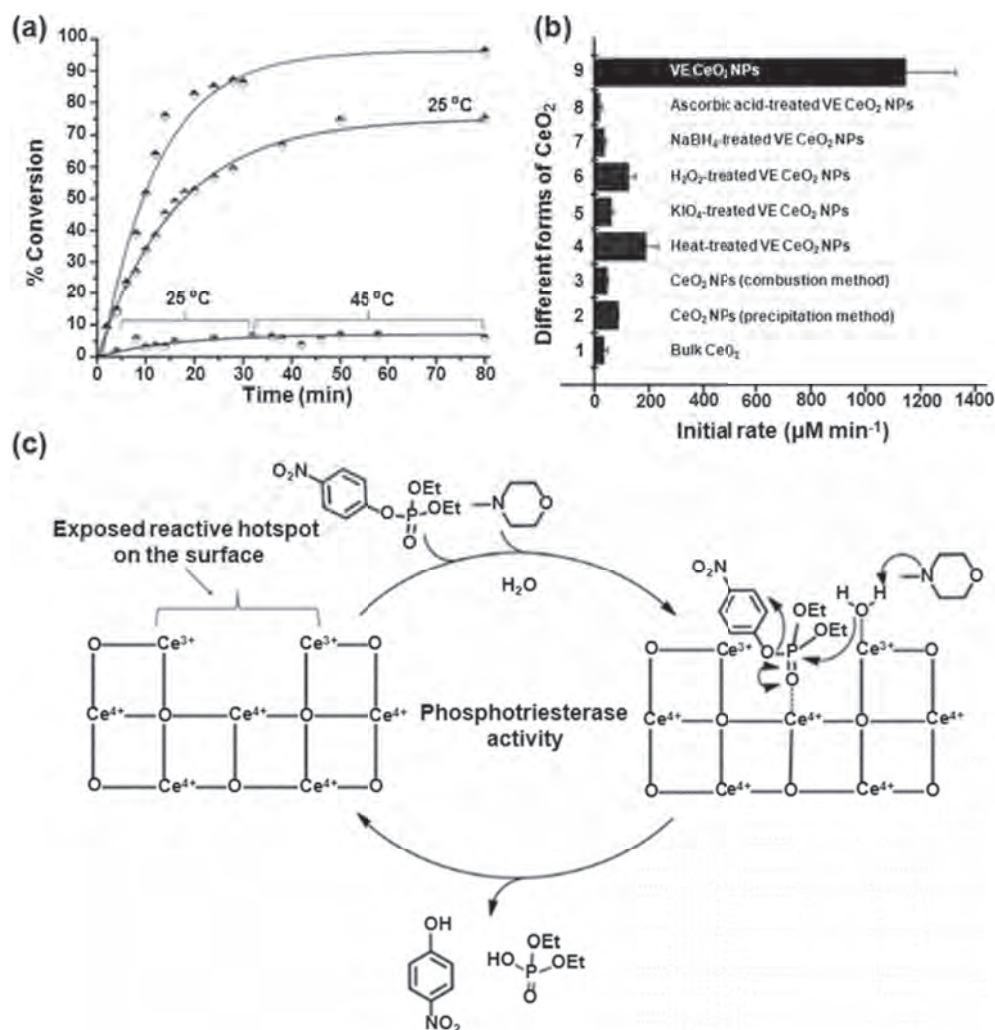


Fig. 34. (a) Comparison of initial rates of degradation of paraoxon by different forms of CeO_2 NPs. (b) Comparison of initial rates of various nanomaterials. (c) Proposed mechanism for the degradation of phosphotriesters by VE CeO_2 NPs. Adapted with permission from Ref. [220]. Copyright © 2016, WILEY-VCH Verlag GmbH & Co. KGaA, Weinheim.

signaling [213]. Also, many chemical warfare agents are toxic organophosphorus compounds containing phosphonate ester bonds [214,215]. Thus, the phosphatase activity of natural and artificial enzymes has been widely improved for the rapid hydrolysis of these toxic chemicals. Previous studies showed that CeO₂ nanostructures could mimic the phosphatase enzymes to cleave the phosphonate ester bonds [216–219]. Recent systematic dephosphorylation reaction kinetics demonstrated that the morphology and surface defects determined the catalytic activity of CeO₂ nanozymes in an order of nanosphere > nano-octahedron > nanorod > nanocube based on their morphologies [218]. It is noted that the surface oxygen vacancy is recognized as the catalytic active site for the cleavage of phosphonate ester bonds. In this case, introducing more surface defects may be able to significantly enhance the phosphatase-mimetic activity of CeO₂.

The effect of surface defects in terms of surface Ce³⁺ fractions was investigated by using the vacancy-engineered (VE) CeO₂ nanoparticles with the size of several nanometers [220]. As compared with other common CeO₂ nanoparticles, VE CeO₂ nanoparticles were synthesized in the presence of H₂O₂. A relative higher surface Ce³⁺/Ce⁴⁺ fraction of 14.28% was then achieved for the VE CeO₂ nanoparticles. The synergistic activity between surface Ce³⁺ and Ce⁴⁺ could facilitate the hydrolysis of phosphonate ester bonds. In particular, the mimetic hydrolysis of paraoxon could be performed as a model reaction in weak basic solutions (pH ~ 10) with *N*-methylmorpholine as a base. The VE CeO₂ nanoparticles were demonstrated to give the very high initial hydrolysis rate over 1000 μM min⁻¹ at 45 °C (Fig. 34a). In contrast, common CeO₂ nanoparticles and other metal oxides showed the poor catalytic activity for hydrolysis reactions (Fig. 34b). Interestingly, either an increase in the surface Ce³⁺ fraction of VE CeO₂ nanoparticles by reductants (e.g., NaBH₄, ascorbic acid) or a decrease in the value of artificial enzymes by oxidants (e.g., H₂O₂, KIO₄), combining with thermal treatment in the presence of O₂, would result in a sharp decrease in the mimetic activity for hydrolysis of paraoxon.

In details, catalytic mechanism investigations suggested that the surface Ce⁴⁺ sites typically served as the adsorption sites for paraoxon molecules because of the polar nature of phosphoryl oxygen and the surface Ce³⁺ species bind and activate H₂O molecules. As shown in Fig. 34c, the cooperative surface Ce³⁺ and Ce⁴⁺ species facilitated the efficient nucleophilic attack of activated water or hydroxide at the phosphorus center. When the surface of CeO₂ catalysts was dominated by the Ce³⁺ species, the surface of nanozymes was then mainly occupied by water molecules. Thus, the organophosphorus compounds became inaccessible to the catalyst surface, which led to degradation in the hydrolysis activity. Conversely, the surface of heavily oxidized CeO₂ nanozymes allowed the selective adsorption of organophosphorus compounds and prevented the accessibility of water or hydroxide, which in turn reduced the phosphatase-mimetic activity. As a result, the optimized Ce³⁺/Ce⁴⁺ ratio of CeO₂ was essential to induce the co-adsorption of both reactants and to enable the mimetic hydrolysis activity.

6. Conclusions and perspectives

In summary, the present review highlights the recent research developments in controlling the surface physicochemical properties of CeO₂ catalysts and their practical applications in advanced catalysis. It is evident that the catalytic activity of CeO₂ is boosted from the surface reversible oxidation states between Ce³⁺ and Ce⁴⁺, which serves as the driving force for the redox chemistry, leads to the formation of the surface oxygen vacancy, and gives the unique surface bifunctional acid-base characteristics. Moreover, as the support of metal catalysts, manipulating the surface chemistry of

CeO₂ is also critical to the corresponding metal dispersion and size, catalytic activity and selectivity, and their capability for anti-sintering and anticoke formation. In general, surface properties of CeO₂ nanostructures can be effectively altered by different synthetic methods, various post-treatments, and surface modifications by small ions and molecules. Besides, the chemical redox etching and the synthetic pressure as well as the partial pressure of O₂ in reaction vessels can also deliver operative and precise modulations of the surface chemical characteristics of CeO₂ nanorods in a wide window. Benefiting from the controllable surface chemistry of CeO₂ catalysts, the catalytic efficiency and chemoselectivity can be well controlled for various catalytic reactions. From these observations, the recent progress and practical applications of heterogeneous CeO₂ catalysts are thoroughly discussed with the focus in CO oxidation, CO₂ conversion, organic synthesis, and their biomimetic performance.

At the same time, regulating the surface chemistry of CeO₂ materials is revealed as a powerful and useful tool to tailor their catalytic selectivity and activity, and even to stimulate new catalytic phenomena evidenced by numerous studies mentioned in this review. Despite the significant progress has been achieved, understandings on the surface chemistry of CeO₂ are still far from being resolved. In order to achieve the further insights, especially disclosing the detailed catalytic mechanism of surface regulated CeO₂ at the molecular and/or atomic levels as well as seeking for the more practical catalytic applications, there remain more critical issues to be addressed.

- (1) Identifications of the spatial distribution of surface defects. Both the locations and concentrations of surface defects are observed to considerably affect the spatial and electronic structures of the catalytic active sites of CeO₂ catalysts. However, although the concentrations of surface defects might be assessed by various characterization techniques (e.g., XPS, and Raman), it is still difficult to evaluate the spatial locations of these species. For example, oxygen vacancies can be existed with many possible configurations, which are usually located on the surface, subsurface or even bulk, significantly affecting the electronic structures of corresponding surface/interface active sites in various ways. Also, the distance between these surface defects can considerably affect the catalytic activity of solid catalysts. It has been reported that CeO₂ nanorods with clusters of oxygen vacancies could deliver the high catalytic activity for CO oxidation [221]. As a result, we can envision the importance of the spatial distribution of surface defects of a catalyst for specific catalytic reactions. Till now, this front has not been well explored because of the lack of sufficient technologies and synthetic strategies to manipulate the defects with well-defined configurations.
- (2) Catalytic performance of CeO₂ modified by small ions and molecules. The bifunctional acid-base properties of CeO₂ catalysts are widely recognized for their selective adsorption of small ions or molecules at the surface-specific sites of catalysts. Recently, the surface modifications of CeO₂ have been successfully demonstrated to further optimize the catalytic efficiency and selectivity for biomimetic reactions and organic catalysis [222]. In specific, the adsorption of small surface species can effectively regulate or even completely change the surface properties of solid catalysts in at least three aspects: (a) the re-distribution of the surface charge, (b) the modulation of the absorption of reactants and desorption of products, and (c) the construction of new surface catalytic sites. However, the effective surface area would get reduced because of the adsorbed species, as

compared with that of the “bare” ones. Therefore, it is highly important to find a descriptor to balance the surface modification and the available surface area. Along this direction, the current progress on modifying the surface chemistry of CeO₂ catalysts with small species remains quite limited. We need to understand the mechanism at the atomic level for surface modifications and make the adsorbed species cope with the existing surface species of CeO₂ catalysts in order further to promote their catalytic activity, selectivity, and stability. Moreover, surface modifications by large molecules, such as polymers and biological molecules, should also be considered, which can then create a microenvironment for specific reactions.

- (3) Precise controllability of surface properties of CeO₂. The surface composition and electronic structure of CeO₂ nano-materials are more complex than that we can imagine. Therefore, an atomic “observation” of the CeO₂ surface before any surface control is important. However, the residue ions adsorbed on the CeO₂ surface from wet chemical synthesis and the surface adsorbed gases (e.g., H₂O, and CO₂) after exposure to ambient conditions are difficult to be removed. They would inevitably add the uncertainty for the precise surface control to realize the desired surface catalytic configurations for advanced catalysis. In this case, it is essential to develop additional novel techniques to recognize the surface species accurately and to manipulate the surface chemistry precisely.
- (4) In-situ and operando characterizations of CeO₂ catalysts under the reaction conditions to provide a structure-activity relation. Generally, nanostructured catalysts are mostly synthesized using wet chemistry approaches, in which the obtained composition/structure may not as perfect as expected. Under the operating catalytic conditions, nano-sized catalysts would probably undergo the surface reconstruction. For example, since CeO₂-base catalysts have been widely used for various catalytic reactions, including oxidation, hydrogenation, and hydrolysis, etc., any change on their surface states under catalytic conditions are unavoidable. Nevertheless, the precise understanding on their evolutions correlated to the catalytic performance have not been well recognized. Thus, it is recommended to emphasize that the in-situ and operando characterization techniques are urgently required in order to deliver an unambiguous structure-activity correlation of CeO₂ catalysts for the further performance enhancement.
- (5) Development of the theoretical methodology. Theoretical calculations are always employed to predict the surface chemistry of solid catalysts and to provide the guidelines for the design of catalysts by using engineered catalytic sites. However, majority of the current theoretical calculations always model the catalyst surface in a simplified way without considering the realistic reaction environments and complicated surface states of the catalysts. All these are wide known as so-called the “modeling-gap.” For example, there are too many possibilities to simulate the surface defects of CeO₂ by considering their spatial configurations. It would become even worse when the dopants or surface adsorbed molecules are involved. Moreover, the dynamic surface reconstruction of CeO₂ under the operative catalytic conditions is also not considered for most of the cases. Therefore, more advanced computational methodologies are needed to clarify minimize the modeling gap, especially to assess the effect of above factors on the surface chemistry of solid catalysts and subsequently their catalytic behaviors.

Acknowledgments

We acknowledge the financial support from the National Natural Science Foundation of China Grant 21401148 and the National 1000-Plan program. This work was also funded by the Fundamental Research Funds for the Central Universities under Grants xjj2013102 and xjj2013043. Prof. Qu is also supported by the Cyrus Tang Foundation through Tang Scholar program.

References

- [1] J. Paier, C. Penschke, J. Sauer, *Chem. Rev.* 113 (2013) 3949.
- [2] T. Montini, M. Melchionna, M. Monai, P. Fornasiero, *Chem. Rev.* 116 (2016) 5987.
- [3] J. Beckers, G. Rothenberg, *Green Chem.* 12 (2010) 939.
- [4] C. Sun, H. Li, L. Chen, *Energy Environ. Sci.* 5 (2012) 8475.
- [5] K. Wu, L.D. Sun, C.H. Yan, *Adv. Energy Mater.* 6 (2016) 1600501.
- [6] L. Vivier, D. Duprez, *ChemSusChem* 3 (2010) 654.
- [7] R.J. Gorte, *AIChE J.* 56 (2010) 1126.
- [8] M. Mogensen, N.M. Sammes, G.A. Tompsett, *Solid State Ionics* 129 (2000) 63.
- [9] W. Huang, Y. Gao, *Catal. Sci. Technol.* 4 (2014) 3772.
- [10] D. Zhang, X. Du, L. Shi, R. Gao, *Dalton Trans.* 41 (2012) 14455.
- [11] A. Trovarelli, *Catal. Rev.* 38 (1996) 439.
- [12] W. Huang, *Acc. Chem. Res.* 49 (2016) 520.
- [13] A. Trovarelli, *Catalysis by Ceria and Related Materials*, World Scientific, 2002.
- [14] C. Sun, U. Stimming, *J. Power Sources* 171 (2007) 247.
- [15] X. Feng, D.C. Sayle, Z.L. Wang, M.S. Paras, B. Santora, A.C. Sutorik, T.X. Sayle, Y. Yang, Y. Ding, X. Wang, *Science* 312 (2006) 1504.
- [16] S. Armini, J. De Messemaker, C. Whelan, M. Moinpour, K. Maex, *J. Electrochem. For. Soc.* 155 (2008) H653.
- [17] T. Morimoto, H. Tomonaga, A. Mitani, *Thin Solid Films* 351 (1999) 61.
- [18] J. Kaspar, P. Fornasiero, M. Graziani, *Catal. Today* 50 (1999) 285.
- [19] M. Haneda, T. Kaneko, N. Kamiuchi, M. Ozawa, *Catal. Sci. Technol.* 5 (2015) 1792.
- [20] M. Boaro, M. Vicario, C. de Leitenburg, G. Dolcetti, A. Trovarelli, *Catal. Today* 77 (2003) 407.
- [21] A. Paulenova, S. Creager, J. Navratil, Y. Wei, *J. Power Sources* 109 (2002) 431.
- [22] Z. Xie, F. Xiong, D. Zhou, *Energy Fuels* 25 (2011) 2399.
- [23] M. Zaki, M. Hasan, L. Pasupulety, *Langmuir* 17 (2001) 768.
- [24] T. Na, J. Liu, S. Wenjie, *Chin. J. Catal.* 34 (2013) 838.
- [25] E. Grulke, K. Reed, M. Beck, X. Huang, A. Cormack, S. Seal, *Environ. Sci. Nano* 1 (2014) 429.
- [26] R. Sakla, R. Hemamalini, K. Pranaw, S. Kumar Khare, *Curr. Bionanotechnol* 2 (2016) 122.
- [27] C. Walkey, S. Das, S. Seal, J. Erlichman, K. Heckman, L. Ghibelli, E. Traversa, J.F. McGinnis, W.T. Self, *Environ. Sci. Nano* 2 (2015) 33.
- [28] S. Sato, R. Takahashi, M. Kobune, H. Gotoh, *Appl. Catal. A Gen.* 356 (2009) 57.
- [29] W. Huang, *Top. Catal.* 56 (2013) 1363.
- [30] D.R. Mullins, P.M. Albrecht, F. Calaza, *Top. Catal.* 56 (2013) 1345.
- [31] S.D. Senanayake, D. Stacchiola, J.A. Rodriguez, *Acc. Chem. Res.* 46 (2013) 1702.
- [32] S. Song, X. Wang, H. Zhang, *NPG Asia Mater.* 7 (2015) e179.
- [33] J.A. Rodriguez, D.C. Grinter, Z. Liu, R.M. Palomino, S.D. Senanayake, *Chem. Soc. Rev.* 46 (2017) 1824.
- [34] J.F. Jerratsch, X. Shao, N. Nilius, H.J. Freund, C. Popa, M.V. Ganduglia-Pirovano, A.M. Burow, J. Sauer, *Phys. Rev. Lett.* 106 (2011) 246801.
- [35] C.T. Campbell, C.H. Peden, *Science* 309 (2005) 713.
- [36] B.W. Sheldon, V.B. Shenoy, *Phys. Rev. Lett.* 106 (2011) 216104.
- [37] J. Li, Z. Zhang, Z. Tian, X. Zhou, Z. Zheng, Y. Ma, Y. Qu, *J. Mater. Chem. A* 2 (2014) 16459.
- [38] Q. Yuan, H.H. Duan, L.L. Li, L.D. Sun, Y.W. Zhang, C.H. Yan, *J. Colloid Interface Sci.* 335 (2009) 151.
- [39] J.Y. Park, L.R. Baker, G.A. Somorjai, *Chem. Rev.* 115 (2015) 2781.
- [40] J.B. Park, J. Graciani, J. Evans, D. Stacchiola, S. Ma, P. Liu, A. Nambu, J.F. Sanz, J. Hrbek, J.A. Rodriguez, *Proc. Natl. Acad. Sci. USA* 106 (2009) 4975.
- [41] K. Yoon, Y. Yang, P. Lu, D. Wan, H.C. Peng, K. Stamm Masias, P.T. Fanson, C.T. Campbell, Y. Xia, *Angew. Chem. Int. Ed.* 51 (2012) 9543.
- [42] D. Kong, G. Wang, Y. Pan, S. Hu, J. Hou, H. Pan, C.T. Campbell, J. Zhu, *J. Phys. Chem. C* 115 (2011) 6715.
- [43] D.R. Mullins, *Surf. Sci. Rep.* 70 (2015) 42.
- [44] W. Huang, G. Sun, T. Cao, *Chem. Soc. Rev.* 46 (2017) 1977.
- [45] M.A. Henderson, C. Perkins, M.H. Engelhard, S. Thevuthasan, C.H. Peden, *Surf. Sci.* 526 (2003) 1.
- [46] K. Deori, D. Gupta, B. Saha, S. Deka, *ACS Catal.* 4 (2014) 3169.
- [47] H. Yao, Y.Y. Yao, *J. Catal.* 86 (1984) 254.
- [48] D. Duprez, C. Descorme, T. Birchem, E. Rohart, *Top. Catal.* 16 (2001) 49.
- [49] Y. Madier, C. Descorme, A. Le Govic, D. Duprez, *J. Phys. Chem. B* 103 (1999) 10999.
- [50] P. Fornasiero, R. Dimonte, G.R. Rao, J. Kaspar, S. Meriani, A. Trovarelli, M. Graziani, *J. Catal.* 151 (1995) 168.
- [51] T. Murota, T. Hasegawa, S. Aozasa, H. Matsui, M. Motoyama, *J. Alloy. Comp.*

- 193 (1993) 298.
- [52] T. Miki, T. Ogawa, M. Haneda, N. Kakuta, A. Ueno, S. Tateishi, S. Matsuura, M. Sato, *J. Phys. Chem.* 94 (1990) 6464.
- [53] T. Maillet, Y. Madier, R. Taha, J. Barbier, D. Duprez, *Stud. Surf. Sci. Catal.* 112 (1997) 267.
- [54] B.K. Cho, *J. Catal.* 131 (1991) 74.
- [55] E. Su, C. Montreuil, W. Rothschild, *Appl. Catal.* 17 (1985) 75.
- [56] J.T. Kummer, *Prog. Energ. Combust.* 6 (1980) 177.
- [57] X.F. Yang, A. Wang, B. Qiao, J. Li, J. Liu, T. Zhang, *Acc. Chem. Res.* 46 (2013) 1740.
- [58] M. Yang, S. Li, Y. Wang, J.A. Herron, Y. Xu, L.F. Allard, S. Lee, J. Huang, M. Mavrikakis, M. Flytzani-Stephanopoulos, *Science* 346 (2014) 1498.
- [59] S. Liang, C. Hao, Y. Shi, *ChemCatChem* 7 (2015) 2559.
- [60] C.R. Henry, *Surf. Sci. Rep.* 31 (1998) 231.
- [61] V. Polshettiwar, R.S. Varma, *Green Chem.* 12 (2010) 743.
- [62] J.K. Norskov, T. Bligaard, B. Hvolbaek, F. Abild-Pedersen, I. Chorkendorff, C.H. Christensen, *Chem. Soc. Rev.* 37 (2008) 2163.
- [63] S. Schaueremann, N. Nilius, S. Shaikhutdinov, H.J. Freund, *Acc. Chem. Res.* 46 (2013) 1673.
- [64] M. Hirano, E. Kato, *J. Mater. Sci. Lett.* 15 (1996) 1249.
- [65] A.I.Y. Tok, F.Y.C. Boey, Z. Dong, X. Sun, *J. Mater. Process. Technol.* 190 (2007) 217.
- [66] M. Hirano, E. Kato, *J. Am. Ceram. Soc.* 82 (1999) 786.
- [67] M. Hirano, E. Kato, *J. Am. Ceram. Soc.* 79 (1996) 777.
- [68] H.X. Mai, L.D. Sun, Y.W. Zhang, R. Si, W. Feng, H.P. Zhang, H.C. Liu, C.H. Yan, *J. Phys. Chem. B* 109 (2005) 24380.
- [69] G. Shen, Q. Wang, Z. Wang, Y. Chen, *Mater. Lett.* 65 (2011) 1211.
- [70] L. Yan, R. Yu, C. Jun, X. Xianran, *Growth Des.* 8 (2008) 1474.
- [71] F. Lin, D.T. Hoang, C.K. Tsung, W. Huang, S.H.Y. Lo, J.B. Wood, H. Wang, J. Tang, P. Yang, *Nano Res.* 4 (2010) 61.
- [72] Z. Guo, F. Du, G. Li, Z. Cui, *Inorg. Chem.* 45 (2006) 4167.
- [73] Q. Wu, F. Zhang, P. Xiao, H. Tao, X. Wang, Z. Hu, Y. Lu, *J. Phys. Chem. C* 112 (2008) 17076.
- [74] C. Sun, J. Sun, G. Xiao, H. Zhang, X. Qiu, H. Li, L. Chen, *J. Phys. Chem. B* 110 (2006) 13445.
- [75] J.G. Caporaso, J. Kuczyński, J. Stombaugh, K. Bittinger, F.D. Bushman, E.K. Costello, N. Fierer, A.G. Peña, J.K. Goodrich, J.I. Gordon, *Br. J. Pharmacol.* 7 (2010) 335.
- [76] S. Yang, L. Gao, *J. Am. Chem. Soc.* 128 (2006) 9330.
- [77] X. Wang, Z. Jiang, B. Zheng, Z. Xie, L. Zheng, *CrystEngComm* 14 (2012) 7579.
- [78] D. Wang, Y. Kang, V. Doan-Nguyen, J. Chen, R. Küngas, N.L. Wieder, K. Bakhtmutsky, R.J. Gorte, C.B. Murray, *Angew. Chem. Int. Ed.* 50 (2011) 4378.
- [79] S. Laha, R. Ryoo, *Chem. Commun.* (2003) 2138.
- [80] W. Yuejuan, M. Jingmeng, L. Mengfei, F. Ping, H. Mai, *J. Rare Earth* 25 (2007) 58.
- [81] C. Sun, H. Li, Z. Wang, L. Chen, X. Huang, *Chem. Lett.* 33 (2004) 662.
- [82] L. González-Rovira, J.M. Sánchez-Amaya, M. López-Haro, E. del Rio, A.B. Hungria, P. Midgley, J.J. Calvino, S. Bernal, F.J. Botana, *Nano Lett.* 9 (2009) 1395.
- [83] R.J. La, Z.A. Hu, H.L. Li, X.L. Shang, Y.Y. Yang, *Mat. Sci. Eng. A Struct.* 368 (2004) 145.
- [84] Y. Chen, J. Lu, *J. Porous Mater.* 19 (2012) 289.
- [85] Y. Sun, Q. Liu, S. Gao, H. Cheng, F. Lei, Z. Sun, Y. Jiang, H. Su, S. Wei, Y. Xie, *Nat. Commun.* 4 (2013) 2899.
- [86] E. Mamontov, T. Egami, R. Brezny, M. Koranne, S. Tyagi, *J. Phys. Chem. B* 104 (2000) 11110.
- [87] N. Shehata, K. Meehan, I. Hassounah, M. Hudait, N. Jain, M. Clavel, S. Elhelw, N. Madi, *Nanoscale Res. Lett.* 9 (2014) 1.
- [88] N.J. Lawrence, J.R. Brewer, L. Wang, T.S. Wu, J. Wells-Kingsbury, M.M. Ihrig, G. Wang, Y.L. Soo, W.N. Mei, C.L. Cheung, *Nano Lett.* 11 (2011) 2666.
- [89] T.S. Sakhivel, D.L. Reid, U.M. Bhatta, G. Möbus, D.C. Sayle, S. Seal, *Nanoscale* 7 (2015) 5169.
- [90] M.M. Khan, S.A. Ansari, D. Pradhan, D.H. Han, J. Lee, M.H. Cho, *Ind. Eng. Chem. Res.* 53 (2014) 9754.
- [91] Y.J. Wang, H. Dong, G.M. Lyu, H.Y. Zhang, J. Ke, L.Q. Kang, J.L. Teng, L.D. Sun, R. Si, J. Zhang, *Nanoscale* 7 (2015) 13981.
- [92] W. Gao, Z. Zhang, J. Li, Y. Ma, Y. Qu, *Nanoscale* 7 (2015) 11686.
- [93] J. Li, Z. Zhang, W. Gao, S. Zhang, Y. Ma, Y. Qu, *ACS Appl. Mater. Interfaces* 8 (2016) 22988.
- [94] K. Liu, A. Wang, T. Zhang, *ACS Catal.* 2 (2012) 1165.
- [95] S. Chen, L. Luo, Z. Jiang, W. Huang, *ACS Catal.* 5 (2015) 1653.
- [96] Z. Hu, X. Liu, D. Meng, Y. Guo, Y. Guo, G. Lu, *ACS Catal.* 6 (2016) 2265.
- [97] Y. Gao, W. Wang, S. Chang, W. Huang, *ChemCatChem* 5 (2013) 3610.
- [98] K. An, S. Alayoglu, N. Musselwhite, S. Plamthottam, G.R.M. Melaet, A.E. Lindeman, G.A. Somorjai, *J. Am. Chem. Soc.* 135 (2013) 16689.
- [99] S.L. Zhong, L.F. Zhang, L. Wang, W.X. Huang, C.M. Fan, A.W. Xu, *J. Phys. Chem. C* 116 (2012) 13127.
- [100] J. Qin, J. Lu, M. Cao, C. Hu, *Nanoscale* 2 (2010) 2739.
- [101] J. Li, P. Zhu, R. Zhou, *J. Power Sources* 196 (2011) 9590.
- [102] D.M. Kempaiah, S. Yin, T. Sato, *CrystEngComm* 13 (2011) 741.
- [103] S. Chang, M. Li, Q. Hua, L. Zhang, Y. Ma, B. Ye, W. Huang, *J. Catal.* 293 (2012) 195.
- [104] Z. Wu, M. Li, S.H. Overbury, *J. Catal.* 285 (2012) 61.
- [105] C. Ho, J.C. Yu, T. Kwong, A.C. Mak, S. Lai, *Chem. Mater.* 17 (2005) 4514.
- [106] C. Pan, D. Zhang, L. Shi, J. Fang, *Eur. J. Inorg. Chem.* 2008 (2008) 2429.
- [107] Z. Yang, J. Wei, H. Yang, L. Liu, H. Liang, Y. Yang, *Eur. J. Inorg. Chem.* 2010 (2010) 3354.
- [108] A.P. Amrute, C. Mondelli, M. Moser, G. Novell-Leruth, N. López, D. Rosenthal, R. Farra, M.E. Schuster, D. Teschner, T. Schmidt, J. Pérez-Ramírez, *J. Catal.* 286 (2012) 287.
- [109] R. Farra, M. Eichelbaum, R. Schlögl, L. Szentmiklósi, T. Schmidt, A.P. Amrute, C. Mondelli, J. Pérez-Ramírez, D. Teschner, *J. Catal.* 297 (2013) 119.
- [110] C. Li, Y. Sun, I. Djerdj, P. Voepel, C.C. Sack, T. Weller, R. Ellinghaus, J. Sann, Y. Guo, B.M. Smarsly, H. Over, *ACS Catal.* 7 (2017) 6453.
- [111] Z. Yang, D. Han, D. Ma, H. Liang, L. Liu, Y. Yang, *Cryst. Growth Des.* 10 (2009) 291.
- [112] G. Hua, L. Zhang, G. Fei, M. Fang, *J. Mater. Chem.* 22 (2012) 6851.
- [113] C.H. Huang, C.S. Tan, *Aerosol Air Qual. Res.* 14 (2014) 480.
- [114] Y. Li, X. Cui, K. Dong, K. Junge, M. Beller, *ACS Catal.* 7 (2017) 1077.
- [115] J. Klankermayer, S. Wesselbaum, K. Beydoun, W. Leitner, *Angew. Chem. Int. Ed.* 55 (2016) 7296.
- [116] G. Centi, E.A. Quadrelli, S. Perathoner, *Energy Environ. Sci.* 6 (2013) 1711.
- [117] M. Aresta, A. Dibenedetto, A. Angelini, *Chem. Rev.* 114 (2014) 1709.
- [118] Q. Liu, L. Wu, R. Jackstell, M. Beller, *Nat. Commun.* 6 (2015) 5933.
- [119] M. Tamura, M. Honda, Y. Nakagawa, K. Tomishige, *J. Chem. Technol. Bio-technol.* 89 (2014) 19.
- [120] B. Santos, C. Pereira, V. Silva, J. Loureiro, A. Rodrigues, *Appl. Catal. A Gen.* 455 (2013) 219.
- [121] M. Honda, M. Tamura, K. Nakao, K. Suzuki, Y. Nakagawa, K. Tomishige, *ACS Catal.* 4 (2014) 1893.
- [122] M. Honda, M. Tamura, Y. Nakagawa, K. Tomishige, *Catal. Sci. Technol.* 4 (2014) 2830.
- [123] M. Honda, S. Kuno, S. Sonehara, K. Fujimoto, K. Suzuki, Y. Nakagawa, K. Tomishige, *ChemCatChem* 3 (2011) 365.
- [124] M. Honda, M. Tamura, Y. Nakagawa, S. Sonehara, K. Suzuki, K. Fujimoto, K. Tomishige, *ChemSusChem* 6 (2013) 1341.
- [125] A. Bansode, A. Urakawa, *ACS Catal.* 4 (2014) 3877.
- [126] Y. Yoshida, Y. Arai, S. Kado, K. Kunimori, K. Tomishige, *Catal. Today* 115 (2006) 95.
- [127] S. Wang, L. Zhao, W. Wang, Y. Zhao, G. Zhang, X. Ma, J. Gong, *Nanoscale* 5 (2013) 5582.
- [128] J. Xu, K.Z. Long, F. Wu, B. Xue, Y.X. Li, Y. Cao, *Appl. Catal. A Gen.* 484 (2014) 1.
- [129] E. Leino, P. Mäki-Arvela, V. Eta, N. Kumar, F. Demoisson, A. Samikannu, A.R. Leino, A. Shchukarev, D.Y. Murzin, J.P. Mikkola, *Catal. Today* 210 (2013) 47.
- [130] E. Leino, N. Kumar, P. Mäki-Arvela, A. Aho, K. Kordás, A.R. Leino, A. Shchukarev, D.Y. Murzin, J.P. Mikkola, *Mater. Chem. Phys.* 143 (2013) 65.
- [131] K. Reed, A. Cormack, A. Kulkarni, M. Mayton, D. Sayle, F. Klaessig, B. Stadler, *Environ. Sci. Nano* 1 (2014) 390.
- [132] R.K. Grasselli, *Top. Catal.* 15 (2001) 93.
- [133] W.C. Chueh, S.M. Haile, *ChemSusChem* 2 (2009) 735.
- [134] W.C. Chueh, C. Falter, M. Abbott, D. Scipio, P. Furler, S.M. Haile, A. Steinfeld, *Science* 330 (2010) 1797.
- [135] B. Wei, R. Fakhrai, B. Saadatfar, *Int. J. Hydrogen Energy* 39 (2014) 12353.
- [136] Y. Wang, B. Li, C. Zhang, L. Cui, S. Kang, X. Li, L. Zhou, *Appl. Catal. B Environ.* 130 (2013) 277.
- [137] D. Jiang, W. Wang, E. Gao, S. Sun, L. Zhang, *Chem. Commun.* 50 (2014) 2005.
- [138] J. Jiao, Y. Wei, Z. Zhao, J. Liu, J. Li, A. Duan, G. Jiang, *Ind. Eng. Chem. Res.* 53 (2014) 17345.
- [139] X. Yang, S. Kattel, S.D. Senanayake, J.A. Boscoboinik, X. Nie, J.S. Graciani, J.A. Rodriguez, P. Liu, D.J. Stacchiola, J.G. Chen, *J. Am. Chem. Soc.* 137 (2015) 10104.
- [140] P. Li, Y. Zhou, Z. Zhao, Q. Xu, X. Wang, M. Xiao, Z. Zou, *J. Am. Chem. Soc.* 137 (2015) 9547.
- [141] P. Kumar, A. Kumar, C. Joshi, R. Singh, S. Saran, S.L. Jain, *RSC Adv.* 5 (2015) 42414.
- [142] A. Primo, T. Marino, A. Corma, R. Molinari, H. Garcia, *J. Am. Chem. Soc.* 133 (2011) 6930.
- [143] X. Zhang, R. You, D. Li, T. Cao, W. Huang, *ACS Appl. Mater. Interfaces* 9 (2017) 35897.
- [144] R. You, X. Zhang, L. Luo, Y. Pan, H. Pan, J. Yang, L. Wu, X. Zheng, Y. Jin, W. Huang, *J. Catal.* 348 (2017) 189.
- [145] Y. Liu, L. Luo, Y. Gao, W. Huang, *Appl. Catal. B Environ.* 197 (2016) 214.
- [146] Y. Wang, F. Wang, Q. Song, Q. Xin, S. Xu, J. Xu, *J. Am. Chem. Soc.* 135 (2013) 1506.
- [147] J.C. Westfahl, T.L. Gresham, *J. Am. Chem. Soc.* 77 (1955) 936.
- [148] M. Tamura, A. Satsuma, K.I. Shimizu, *Catal. Sci. Technol.* 3 (2013) 1386.
- [149] M. Tamura, K. Sawabe, K. Tomishige, A. Satsuma, K.I. Shimizu, *ACS Catal.* 5 (2015) 20.
- [150] A. Rapczyk, M.J. Climent, A. Corma, P. Concepción, S. Iborra, *ACS Catal.* 6 (2016) 4564.
- [151] J. Liu, X.P. Wu, S. Zou, Y. Dai, L. Xiao, X.Q. Gong, J. Fan, *J. Phys. Chem. C* 118 (2014) 24950.
- [152] M. Tamura, K. Tomishige, *Angew. Chem. Int. Ed.* 54 (2015) 864.
- [153] A. Grirrane, A. Corma, H. García, *Science* 322 (2008) 1661.
- [154] B. Li, T. Gu, T. Ming, J. Wang, P. Wang, J. Wang, J.C. Yu, *ACS Nano* 8 (2014) 8152.
- [155] B. Zhang, S. Kaziz, H. Li, M.G. Hevia, D. Wodka, C. Mazet, T. Bürgi, N. Barrabés, *J. Phys. Chem. C* 119 (2015) 11193.
- [156] A. Primo, T. Marino, A. Corma, R. Molinari, H. Garcia, *J. Am. Chem. Soc.* 133

- (2011) 6930.
- [157] P. Zhang, H. Lu, Y. Zhou, L. Zhang, Z. Wu, S. Yang, H. Shi, Q. Zhu, Y. Chen, S. Dai, *Nat. Commun.* 6 (2015) 8446.
- [158] J. Lv, Y. Shen, L. Peng, X. Guo, W. Ding, *Chem. Commun.* 46 (2010) 5909.
- [159] K. Deori, D. Gupta, B. Saha, S. Deka, *ACS Catal.* 4 (2014) 3169.
- [160] A. Leyva-Pérez, D. Cómbita-Merchán, J.R. Cabrero-Antonino, S.I. Al-Resayes, A. Corma, *ACS Catal.* 3 (2013) 250.
- [161] M. Tamura, R. Kishi, Y. Nakagawa, K. Tomishige, *Nat. Commun.* 6 (2015) 8580.
- [162] S. Zhang, J. Li, Z. Xia, C. Wu, Z. Zhang, Y. Ma, Y. Qu, *Nanoscale* 9 (2017) 3140.
- [163] S. Zhang, C.R. Chang, Z.Q. Huang, J. Li, Z. Wu, Y. Ma, Z. Zhang, Y. Wang, Y. Qu, *J. Am. Chem. Soc.* 138 (2016) 2629.
- [164] S. Zhang, Z. Xia, T. Ni, H. Zhang, C. Wu, Y. Qu, *J. Mater. Chem. A* 5 (2017) 3260.
- [165] N. Perret, X. Wang, J.J. Delgado, G. Blanco, X. Chen, C.M. Olmos, S. Bernal, M.A. Keane, *J. Catal.* 317 (2014) 114.
- [166] S.D. Senanayake, P.J. Ramirez, I. Waluyo, S. Kundu, K. Mudiyansele, Z. Liu, Z. Liu, S. Axnanda, D.J. Stacchiola, J. Evans, J.A. Rodriguez, *J. Phys. Chem. C* 120 (2016) 1778.
- [167] M. Tamura, T. Kitanaka, Y. Nakagawa, K. Tomishige, *ACS Catal.* 6 (2016) 376.
- [168] G. Vicario, G. Balducci, S. Fabris, S. de Gironcoli, S. Baroni, *J. Phys. Chem. B* 110 (2006) 19380.
- [169] M. Chong, D.G. Cheng, L. Liu, F. Chen, X. Zhan, *Catal. Lett.* 114 (2007) 198.
- [170] D.G. Cheng, M. Chong, F. Chen, X. Zhan, *Catal. Lett.* 120 (2007) 82.
- [171] G. Vile, B. Bridier, J. Wichert, J. Perez-Ramirez, *Angew. Chem. Int. Ed.* 51 (2012) 8620.
- [172] G. Vile, S. Colussi, F. Krumeich, A. Trovarelli, J. Perez-Ramirez, *Angew. Chem. Int. Ed.* 53 (2014) 12069.
- [173] M. Garcia-Melchor, L. Bellarosa, N. López, *ACS Catal.* 4 (2014) 4015.
- [174] S. Zhang, Z.Q. Huang, Y. Ma, W. Gao, J. Li, F.X. Cao, L. Li, C.R. Chang, Y. Qu, *Nat. Commun.* 8 (2017) 15266.
- [175] H.Z. Zhu, Y.M. Lu, F.J. Fan, S.H. Yu, *Nanoscale* 5 (2013) 7219.
- [176] Z.Q. Huang, L.P. Liu, S. Qi, S. Zhang, Y. Qu, C.R. Chang, *ACS Catal.* (2017) 546.
- [177] M. Tamura, S.M.A. Hakim Siddiki, K.I. Shimizu, *Green Chem.* 15 (2013) 1641.
- [178] Z. Zhang, Y. Wang, J. Lu, C. Zhang, M. Wang, M. Li, X. Liu, F. Wang, *ACS Catal.* 6 (2016) 8248.
- [179] E.G. Heckert, A.S. Karakoti, S. Seal, W.T. Self, *Biomaterials* 29 (2008) 2705.
- [180] K.L. Heckman, W. DeCoteau, A. Estevez, K.J. Reed, W. Costanzo, D. Sanford, J.C. Leiter, J. Clauss, K. Knapp, C. Gomez, *ACS Nano* 7 (2013) 10582.
- [181] A. Karakoti, S. Singh, J.M. Dowding, S. Seal, W.T. Self, *Chem. Soc. Rev.* 39 (2010) 4422.
- [182] S. Das, J.M. Dowding, K.E. Klump, J.F. McGinnis, W. Self, S. Seal, *Nanomedicine* 8 (2013) 1483.
- [183] Z. Tian, J. Li, Z. Zhang, W. Gao, X. Zhou, Y. Qu, *Biomaterials* 59 (2015) 116.
- [184] C. Xu, X. Qu, *NPG Asia Mater.* 6 (2014) e90.
- [185] C.K. Kim, T. Kim, I.Y. Choi, M. Soh, D. Kim, Y.J. Kim, H. Jang, H.S. Yang, J.Y. Kim, H.K. Park, *Angew. Chem. Int. Ed.* 51 (2012) 11039.
- [186] S.S. Lee, W. Song, M. Cho, H.L. Puppala, P. Nguyen, H. Zhu, L. Segatori, V.L. Colvin, *ACS Nano* 7 (2013) 9693.
- [187] F. Pagliari, C. Mandoli, G. Forte, E. Magnani, S. Pagliari, G. Nardone, S. Licocchia, M. Minieri, P. Di Nardo, E. Traversa, *ACS Nano* 6 (2012) 3767.
- [188] P. Xu, B. Maidment 3rd, V. Antonic, I. Jackson, S. Das, A. Zodda, X. Zhang, S. Seal, Z. Vujaskovic, *Radiat. Res.* 185 (2016) 516.
- [189] H. Wei, E. Wang, *Chem. Soc. Rev.* 42 (2013) 6060.
- [190] J. Chen, S. Patil, S. Seal, J.F. McGinnis, *Nat. Nanotechnol.* 1 (2006) 142.
- [191] B. Liu, J. Liu, *Nano Res.* (2017) 1.
- [192] G. Song, Y. Chen, C. Liang, X. Yi, J. Liu, X. Sun, S. Shen, K. Yang, Z. Liu, *Adv. Mater.* 28 (2016) 7143.
- [193] C. Zhang, W. Bu, D. Ni, S. Zhang, Q. Li, Z. Yao, J. Zhang, H. Yao, Z. Wang, J. Shi, *Angew. Chem. Int. Ed.* 55 (2016) 2101.
- [194] H. Li, C. Liu, Y.P. Zeng, Y.H. Hao, J.-W. Huang, Z.Y. Yang, R. Li, *ACS Appl. Mater. Interfaces* 8 (2016) 31510.
- [195] S.M. Hirst, A.S. Karakoti, R.D. Tyler, N. Sriranganathan, S. Seal, C.M. Reilly, *Small* 5 (2009) 2848.
- [196] E.J. Park, J. Choi, Y.K. Park, K. Park, *Toxicology* 245 (2008) 90.
- [197] I. Celardo, J.Z. Pedersen, E. Traversa, L. Ghibelli, *Nanoscale* 3 (2011) 1411.
- [198] X. Wu, Y. Zhang, Y. Lu, S. Pang, K. Yang, Z. Tian, Y. Pei, Y. Qu, F. Wang, Z. Pei, *J. Mater. Chem. B* 5 (2017) 3483.
- [199] C. Korsvik, S. Patil, S. Seal, W.T. Self, *Chem. Commun.* (2007) 1056.
- [200] T. Xia, M. Kovochich, M. Liong, L. Mädler, B. Gilbert, H. Shi, J.I. Yeh, J.I. Zink, A.E. Nel, *ACS Nano* 2 (2008) 2121.
- [201] B.K. Pierscioneck, Y. Li, A.A. Yasseen, L.M. Colhoun, R.A. Schachar, W. Chen, *Nanotechnology* 21 (2009) 035102.
- [202] L. Gao, J. Zhuang, L. Nie, J. Zhang, Y. Zhang, N. Gu, T. Wang, J. Feng, D. Yang, S. Perrett, *Nat. Nanotechnol.* 2 (2007) 577.
- [203] A.K. Yagati, T. Lee, J. Min, J.W. Choi, *Biosens. Bioelectron.* 47 (2013) 385.
- [204] Y. Yang, Z. Mao, W. Huang, L. Liu, J. Li, J. Li, Q. Wu, *Sci. Rep.* 6 (2016).
- [205] X. Jiao, H. Song, H. Zhao, W. Bai, L. Zhang, Y. Lv, *Anal. Methods* 4 (2012) 3261.
- [206] F. Caputo, M. De Nicola, A. Sienkiewicz, A. Giovanetti, I. Bejarano, S. Licocchia, E. Traversa, L. Ghibelli, *Nanoscale* 7 (2015) 15643.
- [207] S. Singh, T. Dosani, A.S. Karakoti, A. Kumar, S. Seal, W.T. Self, *Biomaterials* 32 (2011) 6745.
- [208] A. Asati, S. Santra, C. Kaittanis, S. Nath, J.M. Perez, *Angew. Chem. Int. Ed.* 48 (2009) 2308.
- [209] M. Ornataska, E. Sharpe, D. Andreescu, S. Andreescu, *Anal. Chem.* 83 (2011) 4273.
- [210] A. Hayat, J. Cunningham, G. Bulbul, S. Andreescu, *Anal. Chim. Acta* 885 (2015) 140.
- [211] B. Liu, Z. Huang, J. Liu, *Nanoscale* 8 (2016) 13562.
- [212] X. Li, M. Wilmanns, J. Thornton, M. Kohn, *Sci. Signal.* 6 (2013) 10.
- [213] F. Sacco, L. Peretto, L. Castagnoli, G. Cesareni, *FEBS Lett.* 586 (2012) 2732.
- [214] D.M. Maxwell, K.M. Brecht, I. Koplovitz, R.E. Sweeney, *Arch. Toxicol.* 80 (2006) 756.
- [215] M. Eddleston, N.A. Buckley, P. Eyer, A.H. Dawson, *Lancet* 371 (2008) 597.
- [216] M.H. Kuchma, C.B. Komanski, J. Colon, A. Teblum, A.E. Masunov, B. Alvarado, S. Babu, S. Seal, J. Summy, C.H. Baker, *Nanomed-Nanotechnol* 6 (2010) 738.
- [217] A.A. Vernekar, T. Das, G. Mughesh, *Angew. Chem. Int. Ed.* 55 (2016) 1412.
- [218] M.J. Manto, P. Xie, C. Wang, *ACS Catal.* 7 (2017) 1931.
- [219] B. Fatima, M. Najam-ul-Haq, F. Jabeen, S. Majeed, M.N. Ashiq, S.G. Musharraf, M.A. Shad, G. Xu, *Analyst* 138 (2013) 5059.
- [220] A.A. Vernekar, T. Das, G. Mughesh, *Angew. Chem. Int. Ed.* 55 (2016) 1412.
- [221] X. Liu, K. Zhou, L. Wang, B. Wang, Y. Li, *J. Am. Chem. Soc.* 131 (2009) 3140.
- [222] B. Liu, J. Liu, *Nano Res.* 10 (2017) 1125.